

# Recent Advances in Biomedical Applications

Guest Editors: Alberto Borboni, Tadeusz Mikołajczyk, and Vera Murgul



# Recent Advances in Biomedical Applications

Applied Bionics and Biomechanics

---

## **Recent Advances in Biomedical Applications**

Guest Editors: Alberto Borboni, Tadeusz Mikołajczyk,  
and Vera Murgul



Copyright © 2016 Hindawi Publishing Corporation. All rights reserved.

This is a special issue published in "Applied Bionics and Biomechanics." All articles are open access articles distributed under the Creative Commons Attribution License, which permits unrestricted use, distribution, and reproduction in any medium, provided the original work is properly cited.

## **Editor-in-Chief**

Rene V. Mayorga, University of Regina, Canada

## **Editorial Board**

Saverio Affatato, Italy	Luis Gracia, Spain	Carlo Menon, Canada
Seungik Baek, USA	Eugenio Guglielmelli, Italy	Jose Merodio, Spain
Sabine F. Bensamoun, France	Elena Gutierrez-Farewik, Sweden	Joseph Mizrahi, Israel
Ulrike Böer, Germany	Kozaburo Hayashi, Japan	Juan C. Moreno, Spain
Andrea Cereatti, Italy	Hiroaki Hobara, Japan	Estefanía Peña, Spain
Laurence Cheze, France	Serkan Inceoglu, USA	Bernardo Requena, Spain
Christian Cipriani, Italy	Hoon Eui Jeong, Republic of Korea	Hossein Rouhani, Canada
Jose L. Contreras-Vidal, USA	Zhongmin Jin, China	Simo Saarakkala, Finland
Marco Controzzi, Italy	Kiros Karamanidis, Germany	Jean Slawinski, France
Ugo Della Croce, Italy	Justin Keogh, Australia	Hanno Steinke, Germany
Agnès Drochon, France	Jan Harm Koolstra, Netherlands	Fong-Chin Su, Taiwan
Alicia El Haj, UK	Thibault Lemaire, France	Wei Tan, USA
Fabio Esposito, Italy	Le Ping Li, Canada	Amir A. Zadpoor, Netherlands
Toshio Fukuda, Japan	Francisco Lopez-Valdes, Spain	Stefano Zaffagnini, Italy
Mark D. Geil, USA	Andrea Marinozzi, Italy	Li-Qun Zhang, USA
Ángel Gil-Agudo, Spain	Craig P. McGowan, USA	Yanzhong Zhang, China
Philippe Gorce, France	Kenneth Meijer, Netherlands	Nigel Zheng, USA

# Contents

## **Recent Advances in Biomedical Applications**

Alberto Borboni, Tadeusz Mikołajczyk, and Vera Murgul  
Volume 2016, Article ID 6808695, 1 page

## **Parallel Robot for Lower Limb Rehabilitation Exercises**

Alireza Rastegarpanah, Mozafar Saadat, and Alberto Borboni  
Volume 2016, Article ID 8584735, 10 pages

## **Lower Limb Rehabilitation Using Patient Data**

Alireza Rastegarpanah and Mozafar Saadat  
Volume 2016, Article ID 2653915, 10 pages

## **A Critical Analysis of a Hand Orthosis Reverse Engineering and 3D Printing Process**

Gabriele Baronio, Sami Harran, and Alberto Signoroni  
Volume 2016, Article ID 8347478, 7 pages

## **Design Concepts of Polycarbonate-Based Intervertebral Lumbar Cages: Finite Element Analysis and Compression Testing**

J. Obedt Figueroa-Cavazos, Eduardo Flores-Villalba, José A. Diaz-Elizondo, Oscar Martínez-Romero, Ciro A. Rodríguez, and Héctor R. Siller  
Volume 2016, Article ID 7149182, 9 pages

## **A New Orthodontic Appliance with a Mini Screw for Upper Molar Distalization**

Nurhat Ozkalayci and Mehmet Yetmez  
Volume 2016, Article ID 5728382, 4 pages

## **Functional Design in Rehabilitation: Modular Mechanisms for Ankle Complex**

Francesco Aggogeri, Nicola Pellegrini, and Riccardo Adamini  
Volume 2016, Article ID 9707801, 8 pages

## **Relationship between Lower Limb Angular Kinematic Variables and the Effectiveness of Sprinting during the Acceleration Phase**

Artur Struzik, Grzegorz Konieczny, Mateusz Stawarz, Kamila Grzesik, Sławomir Winiarski, and Andrzej Rokita  
Volume 2016, Article ID 7480709, 9 pages

## **Microstructure and Mechanical Properties of Microwave Sintered ZrO<sub>2</sub> Bioceramics with TiO<sub>2</sub> Addition**

Hsien-Nan Kuo, Jyh-Horng Chou, and Tung-Kuan Liu  
Volume 2016, Article ID 2458685, 7 pages

## **Singular Value Decomposition Based Features for Automatic Tumor Detection in Wireless Capsule Endoscopy Images**

Vahid Faghili Dinevari, Ghader Karimian Khosroshahi, and Mina Zolfy Lighvan  
Volume 2016, Article ID 3678913, 8 pages

## *Editorial*

# **Recent Advances in Biomedical Applications**

**Alberto Borboni,<sup>1</sup> Tadeusz Mikołajczyk,<sup>2</sup> and Vera Murgul<sup>3</sup>**

<sup>1</sup>*Mechanical and Industrial Engineering Department, Università degli Studi di Brescia, Brescia, Italy*

<sup>2</sup>*Production Engineering Department, UTP University of Science and Technology, Bydgoszcz, Poland*

<sup>3</sup>*St. Petersburg State Polytechnical University, Saint Petersburg, Russia*

Correspondence should be addressed to Alberto Borboni; [alberto.borboni@unibs.it](mailto:alberto.borboni@unibs.it)

Received 31 August 2016; Accepted 31 August 2016

Copyright © 2016 Alberto Borboni et al. This is an open access article distributed under the Creative Commons Attribution License, which permits unrestricted use, distribution, and reproduction in any medium, provided the original work is properly cited.

As widely experimented in research and in real world application, the biomedical field is experimenting different innovations, which are associated with the contamination with the knowledge of other research branches, such as material science, engineering, biological systems, and informatics. Different technical journals proposed special issues in recent years on applications of special technologies for biomedical applications and the number of these special issues increased especially in the last ten years. For this reason, we proposed a special issue, more generally on biomedical applications, with the purpose of seeing how the land lies in these territories of the research. The result of this activity is not surely sufficient to trace the state of the art of biomedical applications but can probably help to identify some field of activity.

Different works are devoted to the analysis (A. Struzik et al.) and to the recovery of functional activities associated with the limbs. In fact, different subjects can be injured by one or more pathologies and they can lose some of their abilities. To recover these abilities, researchers proposed new orthoses for both the lower limbs (A. Rastegarpanah et al. and F. Aggogeri et al.) and the upper limbs (G. Baronio et al.).

Some functional parts of the human body can lose their functionalities in an irreversible way, so they must be substituted to reduce pain, to recover functionalities, and to prevent worsening of patient's conditions. The work of J. O. Figueroa-Cavazos et al. is addressed to this direction.

The accurate evaluation of the pathologies needs new instrumentation and new methodologies, as suggested by V. F. Dinevari et al., or innovative processing technologies, such as 3D printing (J. O. Figueroa-Cavazos et al. and G. Baronio et al.).

A particular branch of research is devoted to orthodontic applications of manufacturing technologies (N. Ozkalayci and M. Yetmez) and material science (H.-N. Kuo et al.).

We hope that this special issue can contribute to the discussion of the scientific community to focus on some routes of the research and to enhance some gaps that can be filled in future works.

Alberto Borboni  
Tadeusz Mikołajczyk  
Vera Murgul

## Research Article

# Parallel Robot for Lower Limb Rehabilitation Exercises

Alireza Rastegarpanah,<sup>1</sup> Mozafar Saadat,<sup>1</sup> and Alberto Borboni<sup>2</sup>

<sup>1</sup>Department of Mechanical Engineering, School of Engineering, University of Birmingham, Birmingham, UK

<sup>2</sup>School of Mechanical Engineering, Università Degli Studi di Brescia, Brescia, Italy

Correspondence should be addressed to Alireza Rastegarpanah; [a.r.adrex@yahoo.com](mailto:a.r.adrex@yahoo.com)

Received 22 February 2016; Revised 29 July 2016; Accepted 16 August 2016

Academic Editor: Antonio Riveiro

Copyright © 2016 Alireza Rastegarpanah et al. This is an open access article distributed under the Creative Commons Attribution License, which permits unrestricted use, distribution, and reproduction in any medium, provided the original work is properly cited.

The aim of this study is to investigate the capability of a 6-DoF parallel robot to perform various rehabilitation exercises. The foot trajectories of twenty healthy participants have been measured by a Vicon system during the performing of four different exercises. Based on the kinematics and dynamics of a parallel robot, a MATLAB program was developed in order to calculate the length of the actuators, the actuators' forces, workspace, and singularity locus of the robot during the performing of the exercises. The calculated length of the actuators and the actuators' forces were used by motion analysis in SolidWorks in order to simulate different foot trajectories by the CAD model of the robot. A physical parallel robot prototype was built in order to simulate and execute the foot trajectories of the participants. Kinect camera was used to track the motion of the leg's model placed on the robot. The results demonstrate the robot's capability to perform a full range of various rehabilitation exercises.

## 1. Introduction

Stroke is a leading cause of death [1] and it is also a leading cause of chronic disability with 100,000 patients having their first stroke annually in the UK. Although the rate of mortality due to stroke has been falling, the prevalence of stroke is expected to increase in the future due to the aging population [2]. The improvement of motor recovery and motor plasticity of a patient along specific patterns is the aim of rehabilitation exercises [3–6]. The use of robotic technology in rehabilitation can accelerate the treatment and recovery of the disabled and it actuates the rehabilitation clinics to change their path from labour-intensive operations to technology-assisted operations [7]. Emerging robotic technology in a traditional rehabilitation therapy session would provide high quality treatment at a lower cost and effort. The level of motor recovery of patients can be quantified by defining different rehabilitation exercises for the robot [8].

Different lower limb rehabilitation-assisting robots have been developed to revive the functional mobility of damaged limbs, ranging from complex computerized stations to simple structures. These systems have been categorized in five different groups: (i) treadmill gait trainers, (ii) footplate-based gait trainers, (iii) overground gait trainers, (iv)

stationary gait trainers, and (v) ankle rehabilitation systems. In some studies resistive force has been provided during exercise and haptic simulation has been interacted with VR simulation [9, 10]. Using a 6-DoF parallel robot is an applicable method for lower limb rehabilitation due to its simple configuration and high flexibility in performing a different range of motions [10]. Rutgers is one of the pioneering ankle rehabilitation devices and its developments have been cited in eight different studies [11–17]. In another study, a high performance 2-DoF overactuated parallel mechanism has been designed and built for ankle rehabilitation based on custom designed backdrivable actuators and an impedance control system [18–20]. In another study, the prototype of a 3-RSS/S parallel mechanism has been produced for ankle rehabilitation application [20, 21], but no clinical trials have been found for this system.

To develop the robotic devices, first the motor learning and motor adaption of healthy people should be investigated; and then the neurologically injured patients can be rehabilitated with respect to the obtained results [22, 23]. Therapeutic exercises can vary from range of motion, active assistive isotonic, isometric, isokinetic, and manual exercises [24–26]. The path planning of a hybrid parallel robot for ankle rehabilitation was investigated based on inverse kinematics

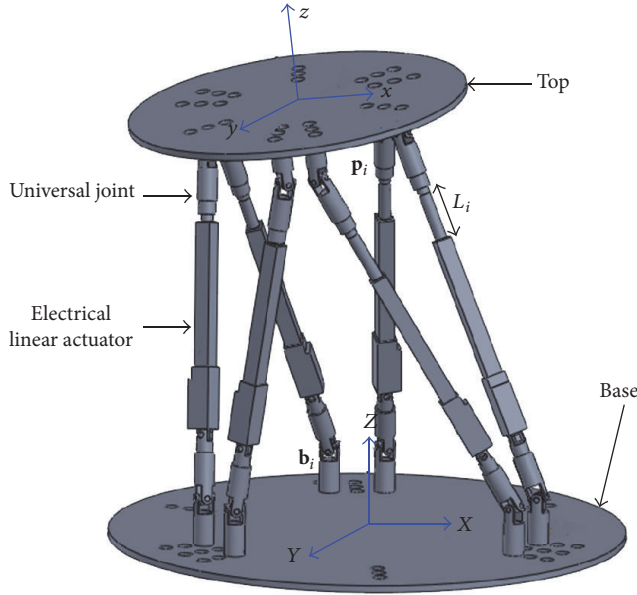


FIGURE 1: The CAD model of the robot designed in SolidWorks.

during normal walking and stepping [27–29]. The 6-DoF parallel robot is stiffer than a tripod as it employs extra three actuators [30]; hence it requires actuators with lower load capacity.

There have been multiple clinically evaluated systems using Kinect, but the majority are being used for upper limb rehabilitation, as seen in [31–33]. Kinect would only be a viable alternative to current red, green, blue, depth (RGB-D) cameras if it provided accuracy that was comparable. In [34] they investigated the accuracy of Kinect by comparing it to a Vicon camera, which is a very precise, but expensive and bulky, marker-based motion capture system. In [34] Kinect is distanced between 1.0 m and 3.0 m from the targets and the RMS errors between the Kinect and Vicon system are all below 10 mm. In [35] it is reported that although Kinect had varied success depending on the activity being done, there was still a good overall relationship between the results of the Kinect and the Vicon system for most movements. In [36] the Kinect is once again compared to the Vicon system, but this time it is tracking elderly persons' foot movements; it is reported that it provides acceptable accuracy in measuring variation in stride velocity [37].

In this paper the healthy participants' data has been used to evaluate the capability of a 6-DoF parallel robot during four various rehabilitation exercises. The performance of the robot

based on real patient data during normal walking will be investigated in a separate research study. The aim of this study is to investigate and evaluate different characteristics of the parallel robot during the performance of different exercises for the rehabilitation of a lower limb. The CAD model and a physical prototype of a 6-DoF robot have been designed and built to simulate the predefined foot trajectories of healthy subjects. All of the required force will be supplied by the actuators during the performing of the exercises. A Kinect camera was used as a depth motion sensor to detect the position of the robot's end effector during its movements.

## 2. Methodology

In this section, first the kinematics and dynamics of a parallel robot have been investigated and then the CAD model of the robot has been designed and simulated in SolidWorks software. The foot trajectories of 20 healthy participants have been analysed and recorded in the gait lab, where they have been used by the proposed parallel robot to follow these trajectories.

**2.1. Kinematic Analysis.** In order to calculate the length of actuators with respect to the reference foot trajectories, the inverse kinematic of 6-DoF parallel robot has been investigated [38]. Focusing the attention on a single leg, it is composed of two links connected to each other by a cylindrical joint and connected to the top and to the base by two respective universal joints. The potential centres of instantaneous rotations (CIR) allowed by the cylindrical joint are on the axis of the joint, while the potential CIR allowed by the top universal joint are in the centre of the joint. The combination of these CIR subspaces is coincident with the axis of the cylindrical joint because it intersects the centre of the universal joint. The same kinematical behaviour can be obtained with a prismatic joint (that substitutes the cylindrical joint) and a spherical joint (that substitutes the top universal joint). Thus we can observe that the proposed UCU parallel robot is kinematically equivalent to a Stewart platform.

In order to find the initial position of the joints connected to the moving platform (top) and fixed platform (base), the 3D CAD model of the robot was designed in SolidWorks (Figure 1). The coordinate system of  $O = (X, Y, Z)$  and  $o = (x, y, z)$  was placed on the centre of top and base, respectively. Equation (1) shows the homogeneous transformation matrix used in [38] and it represents the transformation of the top connecting point to the corresponding base points with respect to the standard Euler angles. The moving frame has been rotated about the fixed  $Z$ -,  $y$ -, and  $z$ -axes, respectively.

$$T_{\text{BASE}}^{\text{TOP}} = \begin{bmatrix} \cos \beta \cos \gamma + \sin \alpha \sin \beta \sin \gamma & -\cos \beta \sin \gamma + \sin \alpha \sin \beta \cos \gamma & \cos \alpha \sin \beta & Px \\ \cos \alpha \sin \gamma & \cos \alpha \cos \gamma & -\sin \alpha & PY \\ \sin \beta \cos \gamma + \sin \alpha \cos \beta \sin \gamma & \sin \beta \sin \gamma + \sin \alpha \cos \beta \cos \gamma & \cos \alpha \cos \beta & PZ \\ 0 & 0 & 0 & 1 \end{bmatrix}, \quad (1)$$

where  $t = [Px, Py, Pz]^T$  and  $\mathfrak{R} = (\alpha, \beta, \gamma)$  represent the translation and rotation of top with respect to the base, respectively.  $\alpha$  and  $\beta$  represent the approach vector of the moving platform and  $\gamma$  is the roll angle about it [38]. The positions of the top joints have been calculated by the following equation:

$$\begin{aligned} & [X_{Ti}, Y_{Ti}, Z_{Ti}, 1]^T \\ &= T_{\text{BASE}}^{\text{TOP}} (px, py, pz, \alpha, \beta, \gamma) [x_{Ti}, y_{Ti}, z_{Ti}, 1]^T \quad (2) \\ & \quad i \in \{1, \dots, 6\}, \end{aligned}$$

where  $\mathbf{P}_i = [X_{Ti}, Y_{Ti}, Z_{Ti}]$  represents the position of the top joints with respect to the base,  $\mathbf{p}_i = [x_{Ti}, y_{Ti}, z_{Ti}]$  represents the position of the top joints with respect to the end effector's coordinate reference, and  $i$  represents the number of actuators. The lengths of the actuators are therefore calculated using the following equations:

$$\mathbf{s}_i = (X_{Ti} - X_{bi}) + (Y_{Ti} - Y_{bi}) + (Z_{Ti} - Z_{bi}) \quad (3a) \quad i \in \{1, \dots, 6\},$$

$$L_i = \|\mathbf{s}_i\| \quad i \in \{1, \dots, 6\}, \quad (3b)$$

where  $(X_{bi}, Y_{bi}, Z_{bi})$  shows the position of the  $i$ th connection point on the base.

The actuator force during different motions have been calculated based on inverse dynamic and Newton-Euler formulation presented at [39]. The unit vector along the actuator was calculated by the following equation:

$$\mathbf{s}_i = \frac{\mathbf{s}_i}{L_i} \quad i \in \{1, \dots, 6\}. \quad (4)$$

The profile of force applied by the foot during different exercises was measured by the force plate in the gait lab and was used as the external force in calculating the actuator force. By calculating the magnitude of actuator forces ( $\mathbf{F} = [F_1 \ F_2 \ F_3 \ F_4 \ F_5 \ F_6]^T$ ), the resultant force ( $\mathbf{R}$ ) and momentum ( $\mathbf{M}$ ) for the system have been calculated by the following equations, respectively [39, 40]:

$$\mathbf{R} = \sum_{i=1}^6 \mathbf{s}_i F_i, \quad (5)$$

$$\mathbf{M} = \sum_{i=1}^6 (\mathbf{b}_i \times \mathbf{s}_i) F_i, \quad (6)$$

where  $\mathbf{b}_i$  is the  $i$ th connection point at the base. The output force has been related to the input forces by (7) [40]:

$$[\mathbf{R} \ \mathbf{M}]^T = \mathbf{H} \mathbf{F}, \quad (7)$$

$\mathbf{H}$

$$= \begin{bmatrix} \mathbf{s}_1 & \mathbf{s}_2 & \mathbf{s}_3 & \mathbf{s}_4 & \mathbf{s}_5 & \mathbf{s}_6 \\ \mathbf{b}_1 \times \mathbf{s}_1 & \mathbf{b}_2 \times \mathbf{s}_2 & \mathbf{b}_3 \times \mathbf{s}_3 & \mathbf{b}_4 \times \mathbf{s}_4 & \mathbf{b}_5 \times \mathbf{s}_5 & \mathbf{b}_6 \times \mathbf{s}_6 \end{bmatrix}, \quad (8)$$

where  $\mathbf{H}$  is a  $6 \times 6$  transformation matrix which describes the relation between the input forces and output forces. When  $\mathbf{H}$  is singular, the extra load will be created on the platform which cannot be supported by the actuator forces. The singularities were identified while the value of determination of the matrix  $\mathbf{H}$  was zero [40]. The static singularity will appear when

$$\det [\mathbf{H}(\mathbf{X}p)] = 0. \quad (9)$$

Equation (9) shows the singularity manifold for the 6-DoF Stewart platform which consists of continuous hypersurfaces which separate the task space into two or more disjointed segments [40]. The length of actuators, actuator forces, and workspace of the robot were calculated by a developed MATLAB program based on kinematics and dynamics of the robot.

**2.2. Robot Analysis.** The prototype of the 6-DoF UCU parallel robot was designed and built in the Robotic Laboratory of University of Birmingham. Six servo actuators with a stroke size of 150 mm were used and the actuators were connected to the top and base by 12 universal joints. A SSC-32 microcontroller was used to control the position of the moving platform.

A Graphical User Interface (GUI) was designed and created in MATLAB to control the movements of the hexapod. The GUI included a data base library with four different exercises. The control system of the robot was designed in such a way to follow the trajectory of a foot during different exercises. Before the robot performed the exercise, its workspace, the required force for each actuator, the length of the actuators, the path motion, and singularly points were calculated and the results were displayed on the monitor.

Due to the stroke limitation of the prototype's actuators, the measured foot trajectories in the gait laboratory were scaled down to three times of the recorded trajectory by the Vicon system, except for in the ankle exercise where the foot trajectory was not scaled down. Then, the scaled-down trajectory was simulated in SolidWorks. The CAD model was linked to MATLAB and by moving the CAD model the physical prototype executed the same motion.

**2.3. Gait Analysis.** Twenty healthy people participated in this study: ten males with average age of  $35.23 \pm 3.02$  years, height of  $175.2 \pm 4.34$  cm, and weight of  $82.764 \pm 4.89$  kg and ten females with an average age of  $33.75 \pm 2.34$  years, height of  $168.23 \pm 3.43$  cm, and weight of  $59.453 \pm 5.563$  kg. The participants have been selected based on the following criteria: (1) able-bodied with no disabilities like drop foot, stroke; (2) weight less than 100 kg; (3) ability to perform functional movements like stair climbing and normal walking. The protocol was approved by the West Midlands Rehabilitation Centre (WMRC), Birmingham, UK. The experiment was advertised at the University of Birmingham and prior to the experimentation the ethical approval was granted to the WMRC and all participants completed a data collection consent form and a health declaration form.

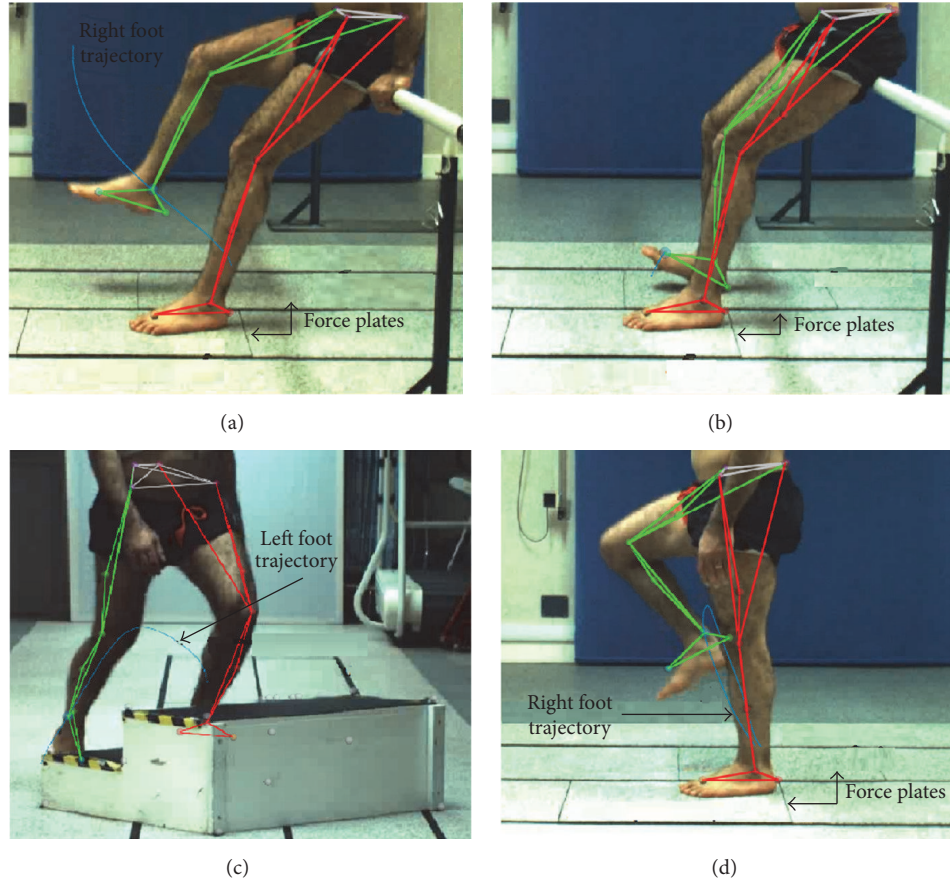


FIGURE 2: Four rehabilitation exercises performed by healthy subjects in the gait laboratory and the foot trajectories were simulated using the Vicon system: (a) hip flexion/extension; (b) ankle dorsiflexion/plantar flexion; (c) stair climbing; (d) marching.

As it is shown in Figure 2, based on consulting with physiotherapists at the WMRC, four different exercises were designed to be performed by the participants in barefoot mode.

The four exercises were (1) hip flexion/extension, (2) ankle dorsiflexion/plantarflexion, (3) stair climbing, and (4) marching. For each exercise, each participant had six good trials with their right leg and six good trials with their left leg. Before starting each exercise, each participant had a warm up trial. The gait laboratory was equipped with 12 Vicon cameras (six MX 3+ and six MX T40), two force plates (one Kistler FP1 with a frequency of 1000 Hz and one Ampti optima with a frequency of 1000 Hz), two digital cameras (sagittal plane and coronal plane), reflective markers, and Vicon Nexus software 1.8.5 and Vicon Polygon 3.5.1 software. After anthropometric measurements, 16 reflective markers were placed on anatomical landmarks with the assistance of therapists at the WMRC.

In the first exercise shown in Figure 2(a), participants were asked to sit on a bar, and while they grasped the support bar, both their feet were placed on the force plates. Then, the participants were asked to perform hip flexion/extension with one leg while the other leg remained on the force plate. In the second exercise, shown in Figure 2(b), participants were

asked to use the support bar to perform ankle dorsiflexion exercise, while both their feet were placed on the force plates and both their hands were free. For the third exercise, a two-step platform was placed in the middle of the gait laboratory's walkway. Stair climbing was started with the participant's right foot used for the first six trials and their left foot was used to start the next trials. The height of each step was 209 mm and the reflective markers were placed on the edges of the step platform to define the location of the stairs. This exercise was created by three submovements; the starting foot moves from the floor to the first step; then the other leg starts its movement from the floor to the second step and finally the starting leg moves from the first step to the second step. In this study only the first movement of the foot segment from the floor to the first step will be investigated.

For instance, the left leg was the starting leg in Figure 2(c). In the last exercise shown in Figure 2(d), participants were asked to stand on the force plate with one foot on each of the right and left force plates. Then participants were asked to bend their knees to the point that their femur was parallel to the ground. This exercise was called marching due to its similarity to military marching. In each exercise the maximum applied force by the leg was measured by the force plate and this was used as an external force which was applied

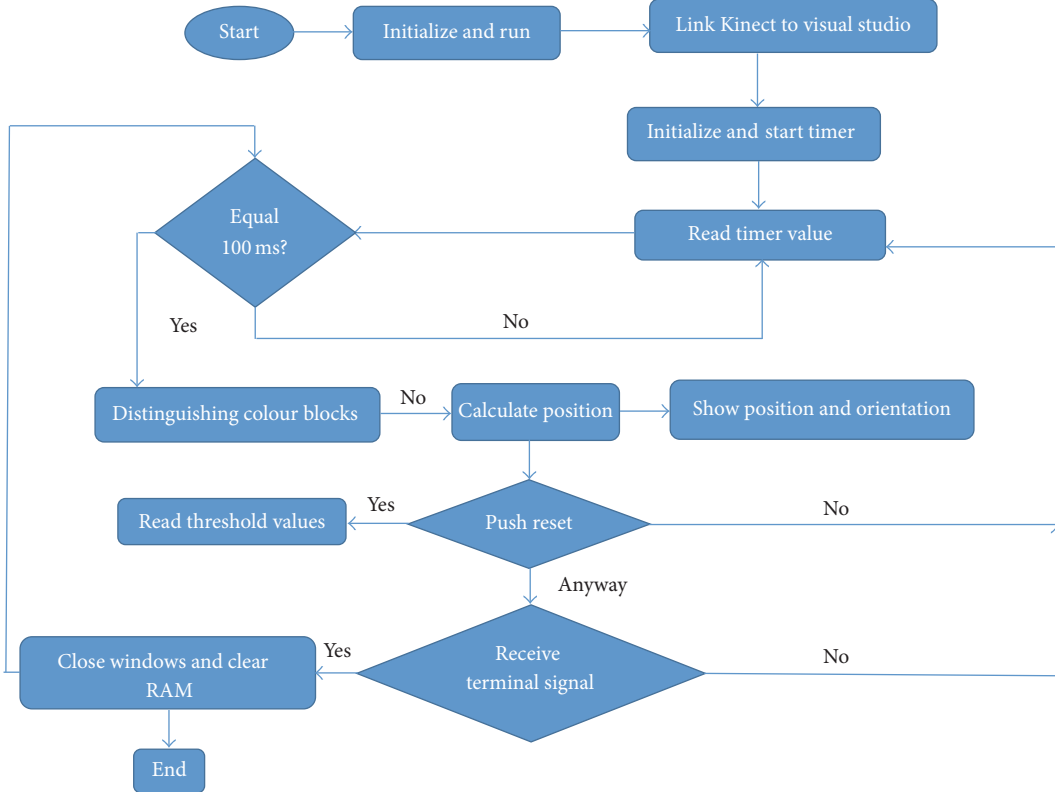


FIGURE 3: Logical flowchart demonstrating colour detection by Kinect camera.

on top of the parallel robot. With respect to the different weights of the participants, the mean value of the maximum forces was calculated for each exercise.

**2.4. Tracking the Foot Trajectory by a Kinect Camera.** To validate the movement of the physical model with the obtained results of the CAD model, a Kinect camera was used as an optical sensor to track and detect the position of the physical hexapod during performance of the exercises. A skeleton model of a lower limb was placed on the moving platform and the movements of the foot were recorded by two Kinect cameras during all exercises. Blue, red, and green paper markers were placed on anatomical landmarks of the foot, similar to the anatomical landmarks which were used in the gait laboratory. It is important to note that the Kinect has serious problems with detecting transparent, reflective, or absorptive objects, as the infrared pattern is not visible or reflected correctly [41]. This is also a reason for using coloured markers on the metal plate, as the reflective surface would cause tracking problems in the depth values. One Kinect camera was placed in the sagittal plane and another one was placed in the lateral plane. In [42] how the depth was calculated by the Kinect was explained.

In order to detect a colour point first the Kinect camera was linked to the visual studio; then the timer read the value, as shown in Figure 3. If that value is equal to 100 ms then the camera distinguishes the colour block and measures the position of the marker. A closed loop was then created in order to detect the position continuously.

In order to calibrate and measure the accuracy of the camera, a ruler with a resolution of 0.1 mm was used. The centre point of a blue marker was placed in different positions along the  $x$ - and  $y$ -axes and the measured values were compared with those measured by the ruler. Ten trials were performed along the  $y$ -axis from 0–300 mm with increments of 30 mm, as shown in Figure 4. A black background was used to reduce the noises created by light. The green, red, and blue markers have been detected by the Kinect camera and they have been marked by yellow circles.

The positions of the markers were measured with respect to the coordinate reference shown in Figure 5. A skeleton model of a leg was connected to a flexible holder from the hip joint and its foot segment was attached on the centre of the moving platform by double-sided sticky tape.

The joints used in the skeleton's knee and ankle model give a wide range of movement for performing different exercises. The position error of the Kinect camera was calculated by comparing its results with those of a Vicon camera. While one camera tracked the movement of the robot in the sagittal plane, the other tracked it in the coronal plane. The data received from the Kinect camera was stored in real time.

### 3. Results and Discussion

**3.1. Workspace of the Robot.** The structural limitations and singularity points of the robot have been considered along the path motion. As it is shown in Figure 6, the workspace

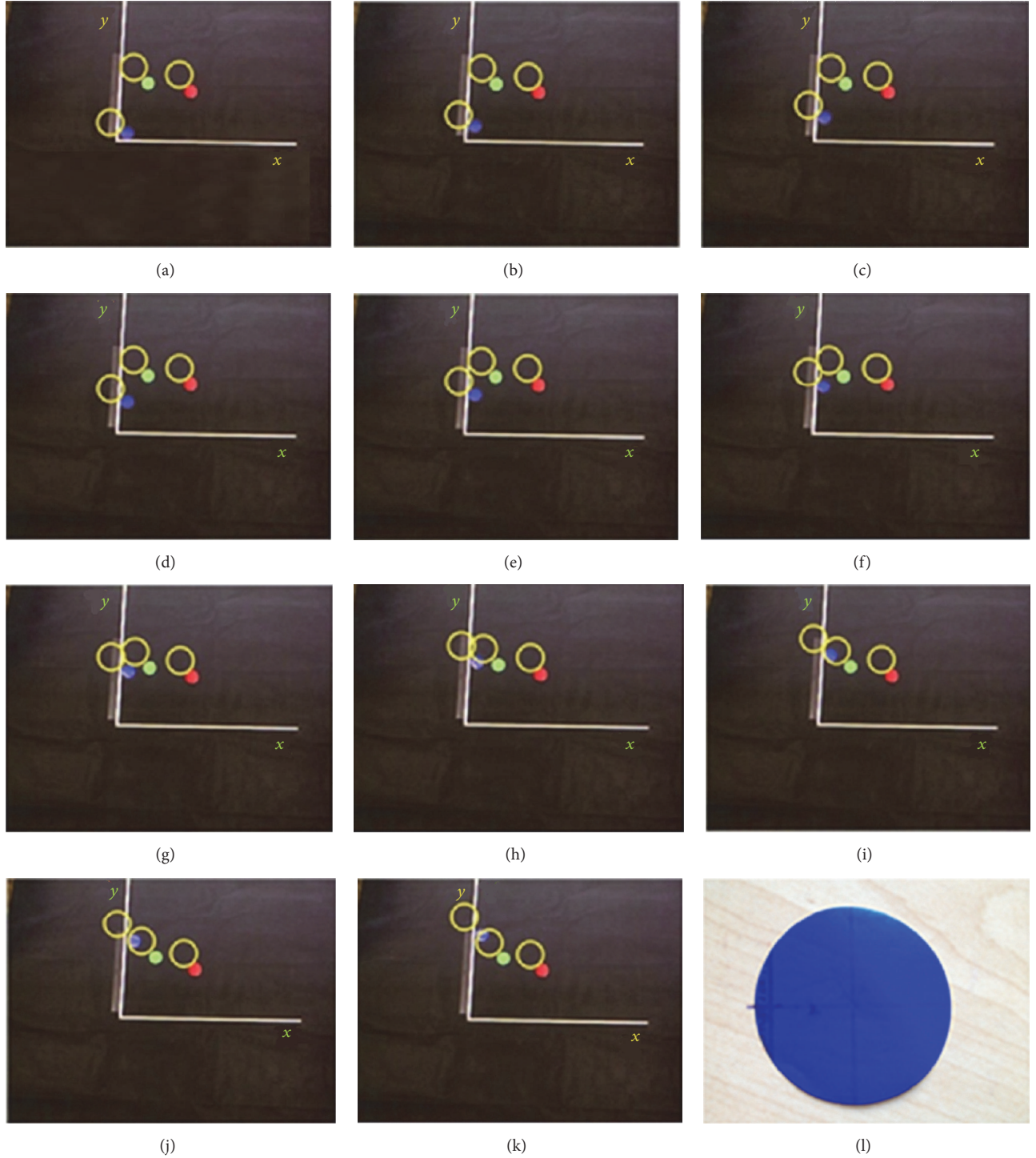


FIGURE 4: Calibration of Kinect camera: (a–k) along  $y$ -axis for every 30 mm from 0 mm–300 mm. (l) Experimental blue marker.

of the robot was simulated in MATLAB software based on the developed numerical method in MATLAB, the structural limitation of the robot, and Cartesian and polar algorithms. The resolution of simulation can be increased by increasing the number of mesh points. The robot was able to move 240 mm along the  $x$ - and  $y$ -axes and 140 mm along the positive  $z$ -axis.

All foot trajectories during different exercises were simulated in MATLAB. The lengths of the actuators were calculated based on (3a). The singularity condition of the robot was checked within the workspace by the developed program in MATLAB. As it is shown in Figure 7, the ranges of motions for different trajectories have been illustrated and it can be found that the end effector moved along the



FIGURE 5: Colour marker detection by Kinect camera using KinectColorBlock software.

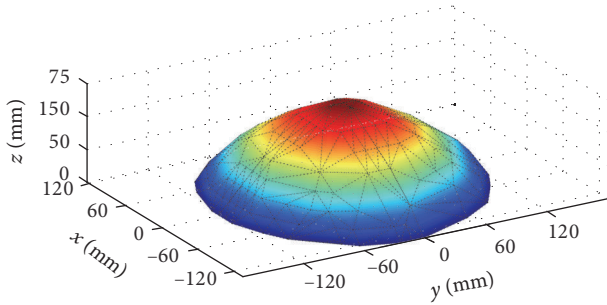


FIGURE 6: Calculated workspace of the robot in MATLAB.

paths inside the workspace. The range of movement for all exercises except the ankle exercise was out of the workspace of the robot, so the trajectory of motion for the marching, hip, and stair climbing exercises has been scaled down three times compared to the recorded trajectory in the gait. In the ankle exercise the moving platform reached the maximum of 6 cm along the  $z$ -axis and then returned to the home position (Figure 7(a)). In the hip exercise the robot simulated the flexion/extension movement for the leg and it reached the maximum of 124 mm along the  $z$ -axis (Figure 7(b)). In the marching exercise the robot reached the maximum of 140 mm along the  $z$ -axis and the variation of movement along the  $x$ -axis was between 0 and 10 mm (Figure 7(c)). In stair climbing, the robot simulated the movement of the foot during one step and it reached the maximum of 110 mm along the  $z$ -axis (Figure 7(d)).

**3.2. Robot Execution and Kinect Detection.** In this section, it will be explained how the exercises were executed by the robot and how the position errors were measured by the Kinect camera. As an example, one of the exercises will be discussed here. As it is shown in Figure 8(b), the trajectory of the foot and the ground reaction force during marching were measured and analysed. The constructed robot followed the scaled-down trajectory of the foot during the marching exercise and it is shown in Figure 8(a).

Working with a Kinect camera in a laboratory environment was much easier, faster, and cheaper than using Vicon

TABLE 1: Position error of Kinect camera during movements of skeleton model of foot by hexapod.

Type of exercise	Maximum position error (mm)			Minimum position error (mm)		
	$x$	$y$	$z$	$x$	$y$	$z$
Marching	34.15	32.78	34.05	11.75	10.81	12.04
Ankle exercise	32.02	33.06	33.25	10.75	10.95	11.80
Knee exercise	33.54	31.65	31.84	11.02	10.75	10.84
Stair climbing	33.24	35.02	33.54	11.46	12.34	11.99

cameras in a clinical environment. Based on the calibration test mentioned in Section 2.4, the mean value of the position error was 2.6 mm for Kinect camera. In this experiment the movements of the skeleton model of the foot and moving platform were measured by the Kinect camera. The position error between the results obtained by the Kinect camera and Vicon camera has been reported in Table 1.

As it is shown by Table 1, the maximum and minimum position errors were 34.15 mm in the  $x$ -axis in marching and 10.75 mm in the  $x$ -axis in the ankle exercise, respectively. Since two cameras were used to track the movements of the robot, one of them tracked the movements in the  $x$ - and  $z$ -axes and the other one was used to track the movements in the  $y$ - and  $z$ -axes. The position error can be decreased by better synchronization between the two cameras. Also these two cameras were placed 1 m away from the robot in order to capture the whole of the movements of the robot without relocating the position of the cameras; this might be another reason for the position error. In this study, a black background was used in order to reduce the light reflection and detect the markers with better resolution; some preliminary tests proved this issue. The robot repeated execution of each exercise 12 times and the mean position error along different axes was presented in Table 1. Considering the Kinect camera as a partly accurate and cheap replacement for a Vicon camera was another achievement of this paper and the error of using a Kinect camera during rehabilitation experiments was addressed fairly. The most important factors in reducing these

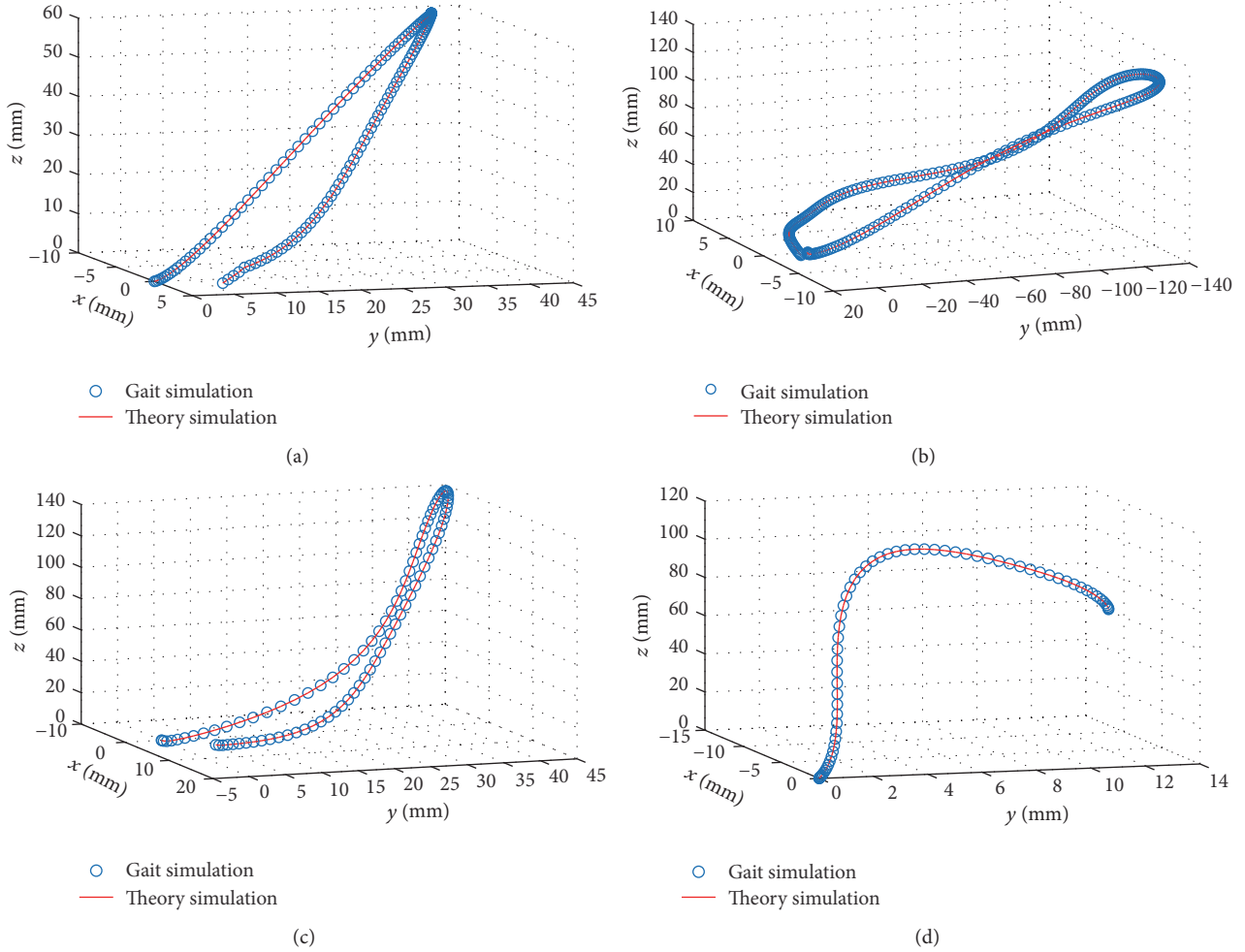


FIGURE 7: Foot trajectory (blue circles) versus robot's trajectory (red line) during 4 different exercises: (a) ankle exercise, (b) hip exercise, (c) marching, and (d) stair climbing.

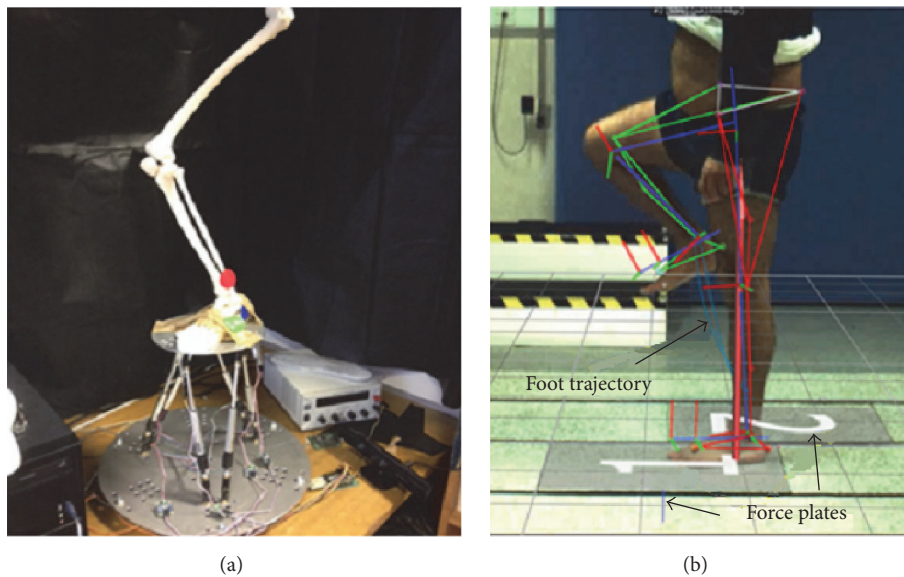


FIGURE 8: Performing marching exercise (a) by the robot and (b) by healthy subject.

errors are increasing the number of cameras and preparing a proper location based on light reflections.

## 4. Conclusion

In this paper different rehabilitation exercises have been simulated by a 6-DoF parallel robot prototype. The ability of the robot during the performance of these exercises has been investigated; however, the trajectories of the foot, for the marching, stair climbing, and hip exercises were scaled down due to the stroke limitation of the actuators used. The maximum and minimum position errors of the trajectories of the physical robot for the same exercises obtained by the Kinect camera were measured to be 34.15 mm and 10.75 mm, respectively. In all cases the robot followed all the trajectories without encountering any singular points. The outcome of this research demonstrates a real capability exhibited by the robot as a robust device for performing various lower limb rehabilitation exercises for patients with lower limb disability.

## Competing Interests

The authors declare that they have no competing interests.

## Acknowledgments

The authors would like to thank the West Midlands Rehabilitation Centre (WMRC), part of Birmingham Community Healthcare NHS Foundation Trust for providing gait measurement laboratory support, and Applied Computing and Engineering Ltd (AC&E) for their sponsorship of this project.

## References

- [1] V. L. Feigin, M. H. Forouzanfar, R. Krishnamurthi et al., "Global and regional burden of stroke during 1990–2010: findings from the Global Burden of Disease Study 2010," *The Lancet*, vol. 383, no. 9913, pp. 245–255, 2014.
- [2] J. M. Veerbeek, E. van Wegen, R. van Peppen et al., "What is the evidence for physical therapy poststroke? A systematic review and meta-analysis," *PLoS ONE*, vol. 9, no. 2, Article ID e87987, 2014.
- [3] N. Tejima, "Rehabilitation robotics: a review," *Advanced Robotics*, vol. 14, no. 7, pp. 551–564, 2000.
- [4] M. Zhang, T. C. Davies, and S. Xie, "Effectiveness of robot-assisted therapy on ankle rehabilitation—a systematic review," *Journal of NeuroEngineering and Rehabilitation*, vol. 10, no. 1, article 30, 2013.
- [5] H. Schmidt, C. Werner, R. Bernhardt, S. Hesse, and J. Krüger, "Gait rehabilitation machines based on programmable footplates," *Journal of NeuroEngineering and Rehabilitation*, vol. 4, no. 1, article 2, 2007.
- [6] J. H. S. Carr and R. B. Shephard, *A Motor Relearning Programme for Stroke*, W. Heinemann Medical Books, London, UK, 1982.
- [7] D. Y. L. Chan, C. C. H. Chan, and D. K. S. Au, "Motor relearning programme for stroke patients: a randomized controlled trial," *Clinical Rehabilitation*, vol. 20, no. 3, pp. 191–200, 2006.
- [8] N. C. Bejarano, S. Maggioni, L. De Rijcke, C. A. Cifuentes, and D. J. Reinkensmeyer, "Robot-assisted rehabilitation therapy: recovery mechanisms and their implications for machine design," in *Emerging Therapies in Neurorehabilitation II*, pp. 197–223, Springer, 2016.
- [9] I. Díaz, J. J. Gil, and E. Sánchez, "Lower-limb robotic rehabilitation: literature review and challenges," *Journal of Robotics*, vol. 2011, Article ID 759764, 11 pages, 2011.
- [10] J. E. Deutsch, C. Paserchia, C. Vecchione et al., "Improved gait and elevation speed of individuals post-stroke after lower extremity training in virtual environments," *Journal of Neurologic Physical Therapy*, vol. 28, no. 4, pp. 185–186, 2004.
- [11] Z. Zhou, W. Meng, Q. Ai, Q. Liu, and X. Wu, "Practical velocity tracking control of a parallel robot based on fuzzy adaptive algorithm," *Advances in Mechanical Engineering*, vol. 2013, Article ID 574896, 5 pages, 2013.
- [12] J. A. Blaya and H. Herr, "Adaptive control of a variable-impedance ankle-foot orthosis to assist drop-foot gait," *IEEE Transactions on Neural Systems and Rehabilitation Engineering*, vol. 12, no. 1, pp. 24–31, 2004.
- [13] R. F. Boian, J. E. Deutsch, C. S. Lee, G. C. Burdea, and J. Lewis, "Haptic effects for virtual reality-based post-stroke rehabilitation," in *Proceedings of the 11th Symposium on Haptic Interfaces for Virtual Environment and Teleoperator Systems (HAPTICS '03)*, pp. 247–253, IEEE, Los Angeles, Calif, USA, March 2003.
- [14] M. Girone, G. Burdea, M. Bouzit, V. Popescu, and J. E. Deutsch, "Orthopedic rehabilitation using the 'Rutgers ankle' interface," *Studies in Health Technology and Informatics*, vol. 70, pp. 89–95, 2000.
- [15] J. E. Deutsch, J. Latonio, G. C. Burdea, and R. Boian, "Post-stroke rehabilitation with the rutgers ankle system: a case study," *Presence*, vol. 10, no. 4, pp. 416–430, 2001.
- [16] J. E. Deutsch, J. Latonio, G. Burdea, and R. Boian, "Rehabilitation of musculoskeletal injuries using the Rutgers ankle haptic interface: three case reports," in *Proceedings of the Eurohaptics Conference*, pp. 11–16, Birmingham, UK, July 2001.
- [17] J. E. Deutsch, J. A. Lewis, and G. Burdea, "Technical and patient performance using a virtual reality-integrated telerehabilitation system: preliminary finding," *IEEE Transactions on Neural Systems and Rehabilitation Engineering*, vol. 15, no. 1, pp. 30–35, 2007.
- [18] J. A. Saglia, N. G. Tsagarakis, J. S. Dai, and D. G. Caldwell, "A high performance 2-dof over-actuated parallel mechanism for ankle rehabilitation," in *Proceedings of the IEEE International Conference on Robotics and Automation (ICRA '09)*, pp. 2180–2186, May 2009.
- [19] J. A. Saglia, N. G. Tsagarakis, J. S. Dai, and D. G. Caldwell, "Control strategies for ankle rehabilitation using a high performance ankle exerciser," in *Proceedings of the IEEE International Conference on Robotics and Automation (ICRA '10)*, pp. 2221–2227, IEEE, 2010.
- [20] J. A. Saglia, N. G. Tsagarakis, J. S. Dai, and D. G. Caldwell, "Inverse-kinematics-based control of a redundantly actuated platform for rehabilitation," *Proceedings of the Institution of Mechanical Engineers, Part I: Journal of Systems and Control Engineering*, vol. 223, no. 1, pp. 53–70, 2009.
- [21] G. Liu, J. Gao, H. Yue, X. Zhang, and G. Lu, "Design and kinematics simulation of parallel robots for ankle rehabilitation," in *Proceedings of the IEEE International Conference on Mechatronics and Automation (ICMA '06)*, pp. 1109–1113, IEEE, Luoyang, China, June 2006.
- [22] G. Liu, J. Gao, H. Yue, X. Zhang, and G. Lu, "Design and kinematics analysis of parallel robots for ankle rehabilitation,"

- in *Proceedings of the IEEE/RSJ International Conference on Intelligent Robots and Systems (IROS '06)*, pp. 253–258, Beijing, China, October 2006.
- [23] R. S. Calabro, A. Cacciola, F. Bertè et al., “Robotic gait rehabilitation and substitution devices in neurological disorders: where are we now?” *Neurological Sciences*, vol. 37, article 503, 2016.
- [24] D. J. Reinkensmeyer, J. L. Emken, and S. C. Cramer, “Robotics, motor learning, and neurologic recovery,” *Annual Review of Biomedical Engineering*, vol. 6, pp. 497–525, 2004.
- [25] E. Akdogan and M. A. Adli, “The design and control of a therapeutic exercise robot for lower limb rehabilitation: physiotherabot,” *Mechatronics*, vol. 21, no. 3, pp. 509–522, 2011.
- [26] H. M. Clarkson, *Musculoskeletal Assessment: Joint Range of Motion and Manual Muscle Strength*, Lippincott Williams & Wilkins, Philadelphia, Pa, USA, 2000.
- [27] J. L. Emken, J. H. Wynne, S. J. Harkema, and D. J. Reinkensmeyer, “A robotic device for manipulating human stepping,” *IEEE Transactions on Robotics*, vol. 22, no. 1, pp. 185–189, 2006.
- [28] H. Rakhodaei, M. Saadat, and A. Rastegarpanah, “Motion simulation of a hybrid parallel robot for ankle rehabilitation,” in *Proceedings of the ASME 12th Biennial Conference on Engineering Systems Design and Analysis*, pp. V003T17A008, American Society of Mechanical Engineers, Copenhagen, Denmark, July 2014.
- [29] H. Rakhodaei, M. Saadat, A. Rastegarpanah, and C. Z. Abdullah, “Path planning of the hybrid parallel robot for ankle rehabilitation,” *Robotica*, vol. 34, no. 1, pp. 173–184, 2016.
- [30] M. Girone, G. Burdea, and M. Bouzit, “The Rutgers Ankle orthopedic rehabilitation interface,” in *Proceedings of the ASME Dynamic Systems and Control Division*, vol. 67, pp. 305–312, 1999.
- [31] I. Pastor, H. A. Hayes, and S. J. Bamberg, “A feasibility study of an upper limb rehabilitation system using kinect and computer games,” in *Proceedings of the IEEE Annual International Conference of the Engineering in Medicine and Biology Society (EMBC '12)*, pp. 1286–1289, September 2012.
- [32] H. Jost, “Kinect-based approach to upper limb rehabilitation,” in *Modern Stroke Rehabilitation through e-Health-Based Entertainment*, E. Vogiatzaki and A. Krukowski, Eds., pp. 169–193, Springer, Berlin, Germany, 2016.
- [33] D. Kairy, M. Veras, P. Archambault et al., “Maximizing post-stroke upper limb rehabilitation using a novel telerehabilitation interactive virtual reality system in the patient's home: study protocol of a randomized clinical trial,” *Contemporary Clinical Trials*, vol. 47, pp. 49–53, 2016.
- [34] T. Dutta, “Evaluation of the Kinect™ sensor for 3-D kinematic measurement in the workplace,” *Applied Ergonomics*, vol. 43, no. 4, pp. 645–649, 2012.
- [35] B. Galna, G. Barry, D. Jackson, D. Mhiripiri, P. Olivier, and L. Rochester, “Accuracy of the Microsoft Kinect sensor for measuring movement in people with Parkinson's disease,” *Gait & Posture*, vol. 39, no. 4, pp. 1062–1068, 2014.
- [36] E. E. Stone and M. Skubic, “Passive in-home measurement of stride-to-stride gait variability comparing vision and Kinect sensing,” in *Proceedings of the Annual International Conference of the IEEE Engineering in Medicine and Biology Society (EMBC '11)*, pp. 6491–6494, September 2011.
- [37] J. Foxcroft, *Tracking a Parallel Robot Using Coloured Markers, Microsoft Kinect and the Kinect Colour Block Application, Internal Communication*, School of Mechanical Engineering, University of Birmingham, 2013.
- [38] K. Liu, J. M. Fitzgerald, and F. L. Lewis, “Kinematics analysis of a Stewart platform manipulator,” *IEEE Transactions on Industrial Electronics*, vol. 40, no. 2, pp. 282–293, 1993.
- [39] B. Dasgupta and T. S. Mruthyunjaya, “A Newton-Euler formulation for the inverse dynamics of the Stewart platform manipulator,” *Mechanism and Machine Theory*, vol. 33, no. 8, pp. 1135–1152, 1998.
- [40] B. Dasgupta and T. S. Mruthyunjaya, “Singularity-free path planning for the Stewart platform manipulator,” *Mechanism and Machine Theory*, vol. 33, no. 6, pp. 711–725, 1998.
- [41] F. Alhwarin, A. Ferrein, and I. Scholl, “IR stereo kinect: improving depth images by combining structured light with IR stereo,” in *PRICAI 2014: Trends in Artificial Intelligence*, D.-N. Pham and S.-B. Park, Eds., vol. 8862 of *Lecture Notes in Computer Science*, pp. 409–421, Springer, Berlin, Germany, 2014.
- [42] J. Hernández-López, A. Quintanilla-Olvera, J. López-Ramírez, F. Rangel-Butanda, M. Ibarra-Manzano, and D. Almanza-Ojeda, “Detecting objects using color and depth segmentation with Kinect sensor,” *Procedia Technology*, vol. 3, pp. 196–204, 2012.

## Research Article

# Lower Limb Rehabilitation Using Patient Data

**Alireza Rastegarpanah and Mozafar Saadat**

*Department of Mechanical Engineering, School of Engineering, University of Birmingham, Birmingham, UK*

Correspondence should be addressed to Alireza Rastegarpanah; [a\\_r\\_adrex@yahoo.com](mailto:a_r_adrex@yahoo.com)

Received 9 March 2016; Accepted 26 July 2016

Academic Editor: Tadeusz Mikołajczyk

Copyright © 2016 A. Rastegarpanah and M. Saadat. This is an open access article distributed under the Creative Commons Attribution License, which permits unrestricted use, distribution, and reproduction in any medium, provided the original work is properly cited.

The aim of this study is to investigate the performance of a 6-DoF parallel robot in tracking the movement of the foot trajectory of a paretic leg during a single stride. The foot trajectories of nine patients with a paretic leg including both males and females have been measured and analysed by a Vicon system in a gait laboratory. Based on kinematic and dynamic analysis of a 6-DoF UPS parallel robot, an algorithm was developed in MATLAB to calculate the length of the actuators and their required forces during all trajectories. The workspace and singularity points of the robot were then investigated in nine different cases. A 6-DoF UPS parallel robot prototype with high repeatability was designed and built in order to simulate a single stride. Results showed that the robot was capable of tracking all of the trajectories with the maximum position error of 1.2 mm.

## 1. Introduction

Neurologic injuries like stroke, traumatic brain, and spinal cord injuries can cause lower limb disabilities [1]. A stroke is the second most common cause of death and the leading cause of disability in Europe [2]. Intensive efforts of therapists and patients are required during traditional rehabilitation sessions; furthermore, 44% of patients who are rehabilitated by physiotherapy will have future problems [3, 4]. By using robotic technology, all labour-intensive operations will be performed by robot-assisted rehabilitation devices and based on the obtained data diagnosis, customization of therapy will be facilitated [5].

There are two main types of robot-assisted lower limb rehabilitation devices available including wearable devices and platform-based devices [6–8]. Functional recovery of the gait can be an indicator of lower limb functional recovery, specifically for the ankle joint [1]. Several different robots have been developed for lower limb rehabilitation such as Rutgers, IT-HPARR, AKROD, GIST, and NUVABAT [9]. Parallel robots can be used for lower limb rehabilitation, motion therapy, and muscle strength training. Motion therapy can be carried out in five different modes including passive, active, active-resistive, active-assistive, and bilateral exercises; and each one of these modes needs a different level of participation from patients. In strength training,

actuators apply resistive force to improve the muscle strength of the user. Based on evidence, therapists suggest that active-assistive exercises provide functional benefits for the patients to do the exercises with the minimum level of manual assistance [1]. However, selecting the proper control strategy and rehabilitation system for a specific lower limb disability is still under research and it should be investigated further [10].

Researchers at Rutgers have focused on the development and effect of a robot-based rehabilitation system in different studies [11–17]. It was found that combination of Rutgers system with a Virtual Reality (VR) system leads to a better outcome on the gait of poststroke patients rather than using the robot alone [12, 14]. In [10, 18], the Rutgers system has been used for cerebral palsy patients and it has been found that the patients' quality of life was improved by increasing their ankle strength and motor control. In another study, a six-degree-of-freedom parallel robot, named R-2000, was used to simulate a gait cycle and ground reaction forces in vitro, based on data obtained from an in vivo gait [19].

There are different optimization techniques for trajectory selection of the manipulator such as minimum seeking algorithms, genetic algorithms, multiple objective optimizations, minimum time trajectory, minimum energy trajectory, and collision free trajectory. All of these techniques are based on kinematics and dynamics' constraints of the manipulator during the path motion. The dynamics' results are much more



FIGURE 1: (a–i) Gait analysis of nine poststroke patients with a paretic leg in the gait laboratory.

realistic in comparison with the kinematics' results in terms of fitting in torque constraints and limitation of the joints [20]. In another study, the path planning for a hybrid parallel robot with 9 DoF has been successfully investigated while the robot was tracking the foot trajectory of healthy subjects [21, 22].

In another study, a parallel robot was designed and built for ankle rehabilitation which was capable of performing only two rotations, since the first two movements are the dominant actions in ankle rehabilitation [23]. To determine the appropriate trajectory for the movement of the robot, there are different methods such as modelling the trajectory based on normative movements [24–26]; a prerecorded trajectory obtained by gait analysis [27, 28]; and a prerecorded trajectory during therapist assistance [29, 30].

In this paper, the performance of a 6-DoF parallel robot in following real patient data based on the robot's kinematic and dynamic analysis has been investigated. The capability of the robot in tracking full range of exercises using healthy participants will be considered in a separate research study. The aim of this study is to test the functionality of a 6-DoF UPS parallel robot in tracking the foot trajectory of paretic patients with respect to the robot's constraints. A 6-DoF

UPS parallel robot was designed and built in order to track the foot trajectory of the paretic leg of nine paretic patients during a single stride. It was assumed that the patients would use the robot in a sitting position and all of the required power for performing the exercise will be supplied by the actuators. The system was developed with and for the use of stroke survivors, particularly for those in the early stage of recovery. Personalising the movements of the robot based on prerecorded foot trajectories of patients is one of the fundamental and necessary issues during the procedure of rehabilitation which will be addressed in this study.

## 2. Gait Analysis

**2.1. Participants.** A total of nine patients including four females and five males attended the West Midlands Rehabilitation Centre for the first session of physical rehabilitation after a stroke. The average age of the group was 49.3 years ranging from 21 to 68 years. Participants completed informed consent form to take part in this study which had acquired the relevant ethical approval. Three females, shown in Figures 1(a), 1(g), and 1(h), and three males, shown in Figures 1(d), 1(f), and 1(i), were paralysed on the right side of their body

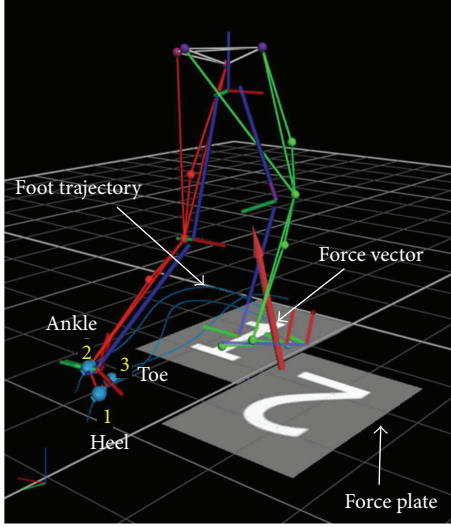


FIGURE 2: 3D simulation of lower limb trajectory of the affected leg with respect to the attached markers.

and the rest, shown in Figures 1(b), 1(c), and 1(e), were paralysed on the left side. One of the male participants shown in Figure 1(c) and one of the female participants shown in Figure 1(a) used a walker during gait analysis. Except for one of the males shown in Figure 1(e), all other participants wore shoes during the test.

**2.2. Measurements.** The gait laboratory was equipped with 12 Vicon cameras (with frequency of 100 Hz) including six MX3+ and six MX T40 cameras. Two digital 50 Hz cameras were used in the sagittal and lateral planes. The Vicon cameras were synchronised with two force plates (Kistler and Ampti Optima) which were used in the laboratory to collect data with a sampling frequency of 2000 Hz. Before data collection, the cameras were calibrated within a  $2.8 \text{ m}^2$  calibration volume. Sixteen reflective markers were placed on the participant's right and left leg to record the gait parameters. The position of the markers was measured by the Vicon system and temporal spatial parameters, linear velocity, and acceleration of the markers were calculated. Based on the Cardan angle system, the joint movements were calculated. The resultant force of the joints was calculated by applying inverse dynamic. The data for each leg was averaged over the successful trials.

A set of three markers were attached to the thigh, shank, and foot segments. Before starting the experiment, the height, mass, and all anthropometric dimensions of the participants were measured including pelvis depth, knee width, hip breadth, and sphygmon height.

Each participant was asked to walk on a 10 m walkway with self-selected speed. Six successful trials were collected for each leg with a total 12 trials for each participant. The trajectory of the foot segment was calculated with respect to the measured trajectory of attached markers 1, 2, and 3, which were placed on the heel, ankle joint, and toe, respectively, as shown in Figure 2. The normal vector of the plane created



FIGURE 3: 6-DoF UPS parallel robot prototype built at the University of Birmingham.

by these three markers was calculated by the following equation:

$$\vec{n} = \mathbf{P}_1\mathbf{P}_2 \times \mathbf{P}_1\mathbf{P}_3, \quad (1)$$

where  $\mathbf{P}_1$ ,  $\mathbf{P}_2$ , and  $\mathbf{P}_3$  represent the position of heel, ankle, and toe markers, respectively.

### 3. Analysis of Parallel Robot

**3.1. Development of Physical Model.** The kinematics of the parallel robot has been investigated based on orientation ranges and linear translation of the foot segment. The length of the actuators of the parallel robot and the actuators forces were calculated; then the singularity regions of the robot were investigated based on Newton-Euler formulation addressed in [31–33].

To follow the trajectory of a foot during a gait cycle, an algorithm was developed in MATLAB to calculate the length of the actuators and the required force for each actuator based on kinematics, dynamics, singularity, and workspace of the designed robot. The desired trajectory was measured in the gait laboratory and was imported to the control system of the robot. A CAD model of the robot was linked to MATLAB to follow the same trajectory. In case the robot faces any kind of constraint, singularity points, or workspace limitation, it searches for the next reachable point along the trajectory.

Based on kinematics and dynamics analysis, a six-DoF hexapod was built at the University of Birmingham [34], as shown in Figure 3, using six linear servo actuators with a stroke of 30 cm, operating speed (12 V) of 55.88 mm per second, dynamic trust (12 V) of 11.33 Kg, and static trust (12 V) of 226.79 Kg connected to the top and base by six rolling spherical joints (SRJ016C) and six universal joints. Ultralight G6 polycarbonate foot wear with adjustable straps was placed on the top platform. A micro control SSC-32 was used to control the movements of the UPS robot.

A graphical user interface (GUI) has been designed in MATLAB in order to control the movements of the robot

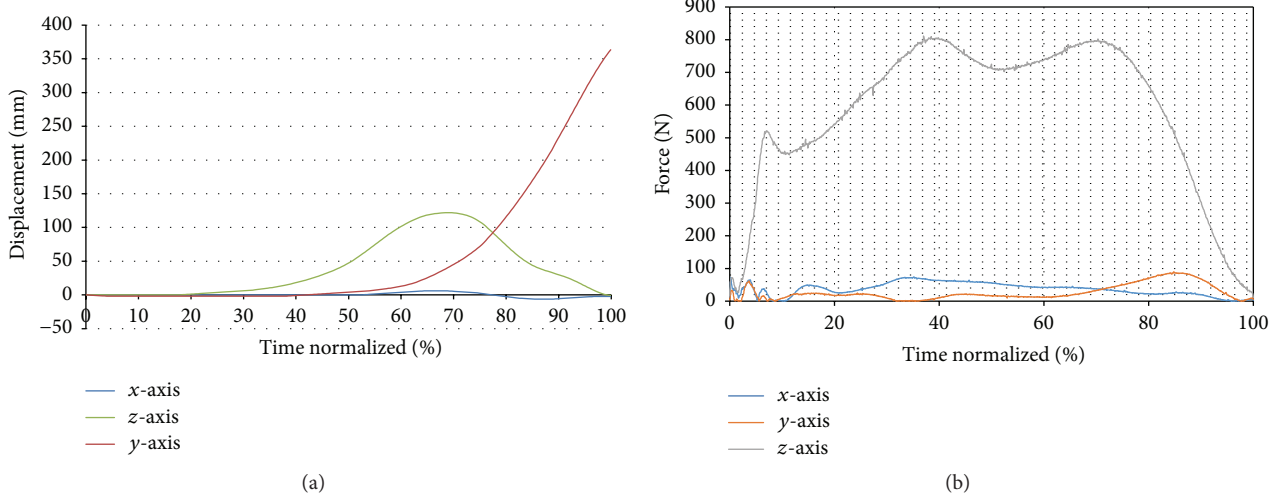


FIGURE 4: Gait results for paralysed participant (a). (a) Foot trajectory in  $x$ -,  $y$ -, and  $z$ -axes and (b) ground reaction force in  $x$ -,  $y$ - and  $z$ -axes. Kistler force plate (right leg).

based on a designed control system. The obtained trajectories from the gait laboratory were used as reference trajectories and the error value was continuously calculated as the difference between the actual foot trajectory and robot's end-effector trajectory. A database, as a library of various rehabilitation exercises, has been embedded in the GUI which enables the operator to select the most appropriate exercise for the rehabilitation of the lower limb. Three different speed modes have been designed for the robot, including slow, medium, and fast, which will be used in different stages of rehabilitation.

**3.2. Repeatability of Parallel Hexapod Robot Movement.** An experiment was conducted to evaluate the repeatability and reliability of the robot's positioning in the static mode as follows. The robot was first positioned to (0, 0, 120) mm in the  $z$ -axis to allow it to translate freely across the  $x$ - and  $y$ -axes. Then, the robot was moved to -100 mm on the  $x$ -axis. Once it has stopped moving, the robot was moved to +100 mm on the  $x$ -axis and then moved back to -100 mm again. The stroke length of the shortest actuator was measured with a set of Vernier callipers. Then, the motion was repeated and the stroke was measured another three times to produce four sets of data for the desired position. This procedure was repeated for several other stroke lengths within the workspace area of the robot. Finally, the robot was moved back to the translation coordinate (0, 0, 120) mm. The above procedure was repeated for all axes of translation. The  $z$ -axis translations' range was marginally smaller than that of the other two axes.

## 4. Results and Discussion

In this study, the average range of motion of the participants' ankle joints during a gait cycle in plantarflexion/dorsiflexion was ( $8^\circ$ ,  $7.74^\circ$ ), in adduction/abduction was ( $10.08^\circ$ ,  $3.35^\circ$ ), and in inversion/eversion was ( $16.07^\circ$ ,  $3.65^\circ$ ), respectively.

**4.1. Gait Results.** In Section 2, we explained how the trajectory of the foot was calculated based on the coordinates of the attached markers. Foot trajectories of all participants have been measured through the Vicon system and the data were analysed by Vicon Nexus software. The obtained trajectory of the leg was normalized for each participant during a single stride. The mean averaged trajectories over six trials were calculated for individual patients in order to be used by the control system of the robot. For instance, the foot trajectory of participant (a) has been normalized in time and shown in Figure 4(a). The foot trajectory reached a maximum of 120 mm along the  $z$ -axis when the foot reached 68% of its trajectory. The ground reaction forces and movement of the paralysed leg were measured by the force plate. As shown in Figure 4(b), the range of variation of force in the  $x$ - and  $y$ -axes changed from 0 to 98 N, while this value changed from 0 to 810 N in the  $z$ -axis. The peak force in the  $z$ -axis occurred when both the heel and the toe were in contact with the force plate. At 40% of the trajectory, both the heel and the toe touched the force plate, and at 52% of the trajectory the heel lost its contact with the force plate. The maximum ground reaction force in different axes was used as an external force in order to calculate the actuator forces during the foot trajectory.

**4.2. Reliability Analysis.** The charts in Figure 5 for the translations in the  $X$  and  $Y$  coordinates show an apparent similarity between them, with both deviations showing a peak at around 225 mm displacement (Figures 5(a) and 5(b)) and coming to a plateau beyond the peak point (0.55 and 0.43 mm for  $X$  and  $Y$ , resp.). The stroke lengths at 225 mm displacement for all six actuators were 202.9, 212.0, 80.7, 91.6, 159.2, and 139.5 mm. For comparison, at a displacement of 150 mm in the  $x$ -axis, the stroke lengths are 166.1, 89.7, 172.4, 135.7, 82.5, and 122.2 mm. The average stroke lengths are marginally longer at 225 mm, with a couple of strokes reaching over 200 mm in length. This

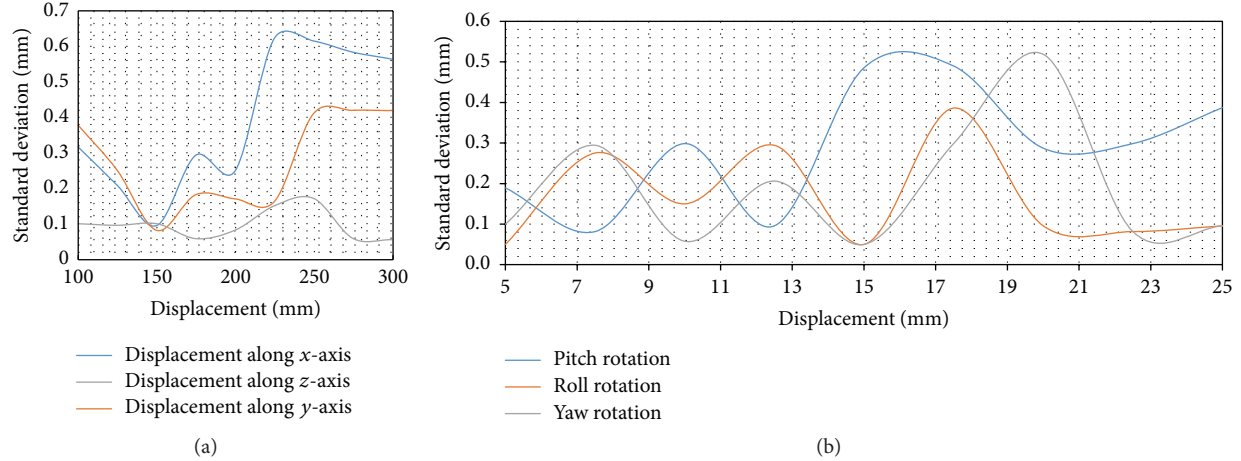


FIGURE 5: Robot repeatability test; (a) reliability of actuators for displacement along  $x$ -,  $y$ - and  $z$ -axes and (b) reliability of actuators for roll, pitch, and yaw rotations.

is closer to approaching the maximum stroke of the actuator of 250 mm compared to the stroke lengths at 150 mm. It was observed that the unreliability increases with the stroke of the actuators. In theory, if all of the actuators are of equal performance, there should be no variation between the data generated from the translations between the  $x$ - and  $y$ -axis translations. However, small errors in the measurement procedure such as inconsistent lengths along the clevis of the actuators will lead to differences between the axes.

As expected, the  $z$ -axis translations showed a distinct trend compared to that of the  $x$ - $y$ , as the vertical displacement occurs on a different plane. Comparing the absolute values of standard deviation on the  $z$ -axis with that of the other translations, it shows that the actuators can be up to 3.65 times more reliable in purely vertical translations compared to lateral movements. The standard deviations only peak at 0.171 mm (Figure 5(a)) as opposed to 0.420 and 0.624 mm for the other two axes of translation.

Translations purely in the  $z$ -axis have a different characteristic in that all of the actuator lengths are theoretically equal at all positions. Due to this characteristic, all of the actuators are only required to move together at the same speed compared to other translations, which require some actuators to move in a sequence. This leads to a more reliable  $z$ -axis movement. The controller used in the platform (Lynxmotion SSC-32) is programmable to synchronise movement across all actuators; however, due to the fixed duty cycle on the actuator hardware, it is not possible to achieve this synchronisation.

In contrast to the reliability of the actuators under translation, rotational movements showed fluctuating reliability. However, the trend is not random as all three axes of rotation show peaks of unreliability between 15 and 20 degrees of rotation and a similar plateau beyond that range. The three rotations are visually similar in “phase” and characteristics.

**4.3. Robot Analysis.** The workspace of the robot was simulated in MATLAB with respect to the maximum length of the actuators and joint constraints in order to find the

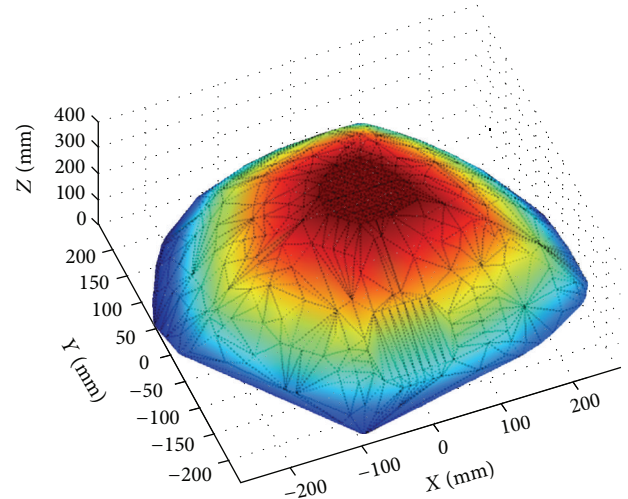


FIGURE 6: The simulated workspace of the robot in MATLAB.

reachable boundary of the moving platform, as shown in Figure 6. The maximum translations of the end effector in the  $x$ -,  $y$ -, and  $z$ -axes were 556 mm, 556 mm, and 280 mm, respectively.

The trajectory of the foot of participant (a) was used by the developed program in MATLAB in order to find the length of the actuators for that particular motion. The calculated lengths are transferred to the interface program (VBA) in order to modify the motors that are developed in the assembled CAD model in SolidWorks. An algorithm was developed in MATLAB to calculate the force of the actuators during the movements of the robot based on measured data in the gait laboratory and kinematic analysis. The actuators' forces were calculated for individual cases and the average value for all participants' trajectories were calculated in 5.5 s, as shown in Figure 7. The required forces for actuators 1 and 4 started between 293 N and 243 N, respectively, and reached their maximum values of 450 N and 370 N, respectively, during the swing phase of the gait cycle. The trend of the

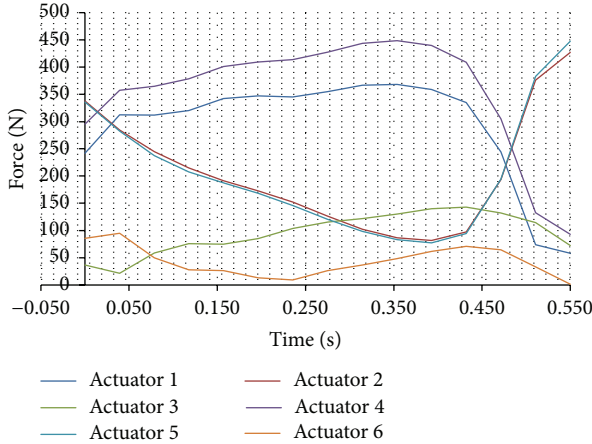


FIGURE 7: Average required force of six actuators during a single stride.

force for actuators 2 and 5 started between 348 N and 346 N and was decreased gradually; however, after 4 s they increased to their maximum values of 435 N and 449 N, respectively. The trend of the forces for actuators 3 and 6 fluctuated in the stance phase of the gait, in a time range of 0 s–0.9 s and then both of them reached their maximum values of 100 N and 50 N at 4.4 s, respectively.

The trajectory of the foot during a gait cycle has been followed by the end effector for all nine participants, as given in Figure 8. The trajectory of the foot measured in the gait laboratory was compared with a simulated trajectory of the robot in MATLAB. The illustrated foot trajectory for each participant is the average of six successful trials. The measured paralysed foot trajectories of the patients during a single stride have been scaled down in the  $y$ -axis two times from the original foot trajectory in order to be within the workspace of the robot. The robot was able to move 278 mm in the positive  $y$ -axis while the maximum scaled down trajectory is 263 mm in the  $y$ -axis (Figure 8(e)). The robot was able to track the foot trajectory of all nine patients during a single stride, although their foot trajectories were different from one another. The robot started its movement from the home position, while all actuators' stroke sizes were zero. Initially, the robot calculated the length of the actuators with respect to the predefined trajectories, and then it calculated the required force of the actuators with respect to the applied GRF. The singularities of the robot during its movement have been investigated with respect to the joint constraint and workspace of the robot. If there was not any singularity point during the trajectory of the robot, then it started its movement. The speed of the actuators during its movement was 2.71 cm/s, which was constant along the entire trajectory. In Figure 8(a), the robot reached 66 mm in the  $z$ -axis; this was the time that the foot reached its maximum position during a single stride. The patients were asked to walk as much as possible in a straight line; as a result, the variation of data in  $X$  was between -10 mm and +10 mm for all cases. The trend of the foot trajectory was very similar between all

cases, so the robot moved along similar trajectories. However, it is very important to personalise the trajectory of motion for individual patients since small movements out of the range of motion of the joint can cause serious injury to the patient.

The mean position error of the robot has been calculated while the robot tracked the foot trajectory. The position of the end effector has been calculated based on the servo feedback of the actuators. The results were then compared with the gait results. The mean values of the position error over the nine participants were 0.7 mm, 1.2 mm, and 0.95 mm in the  $x$ -,  $y$ -, and  $z$ -axes, as shown in Figure 9. The results reveal that the 6-DoF UPS parallel robot has sufficient accuracy for ankle rehabilitation.

As shown in Figure 9(a), the position error in the  $x$ -axis was zero when the robot was passing 50% of the trajectory. The position error in the  $y$ -axis fluctuated and reached its maximum of 1.2 mm after passing 95% of the trajectory. The maximum position error was caused by the joint constraint of the robot. The position error in the  $z$ -axis started from zero and after 0.26 s it reached zero. This means that the position error in the  $z$ -axis was zero when the foot trajectory reached its maximum position. Then, this error was increased radically up to 0.95 mm before decreasing to zero at the end of the trajectory. Since the stroke size was increasing along two axes, the position error was expected to increase too. The system would be able to track the trajectory profile during different rehabilitation exercises with respect to the maximum position error of 1.2 mm. However, the error band can be reduced by improving the architecture of designed algorithm, where the system's accuracy can be further improved.

The long stroke size of the system enables the operator to perform various exercises which require a larger workspace. The current rehabilitation device is potentially inexpensive and easy to use in local clinics and hospitals without special training. The system would allow high quality treatment of people with severe impairments at any time after stroke. Furthermore, therapy and performance would be more consistent, predictable, and measurable. Personalising the foot trajectories by averaging the motions over a number of trials is one of the critical issues which should be considered during the rehabilitation process. The averaged foot trajectory of patient's healthy leg can be used as a reference trajectory for rehabilitation of the affected leg by the robot. Although Rutgers robot [13–15], ARBOT, and other developed parallel ankle robots [35, 36] consider lower limb rehabilitation using a parallel robot, defining the protocols of suitable exercises that can be performed by the robot has not yet been addressed properly. However, in this study, an attempt has been made to introduce a number of fundamental protocols for defining suitable exercises that can be used by the robot.

## 5. Conclusion

In this study, the capability of a 6-DoF parallel robot for lower limb rehabilitation using foot trajectories of a number of patients with paretic legs has been analysed. A physical

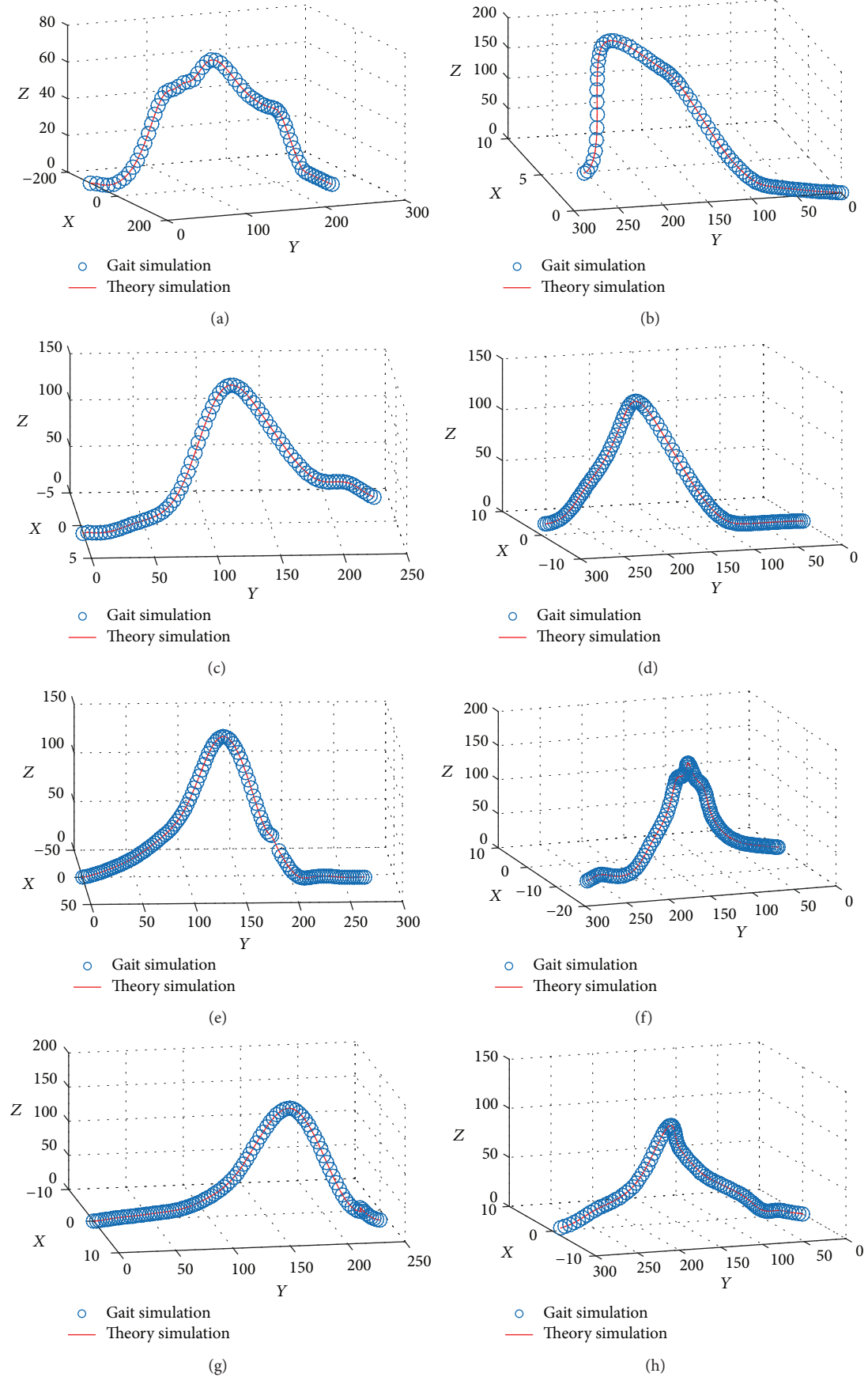


FIGURE 8: Continued.

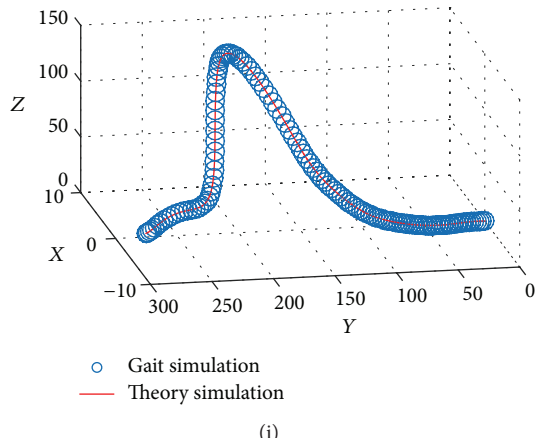


FIGURE 8: (a–i) represent the trajectory of the foot trajectory based on gait results with respect to the trajectory of the robot during performance of the exercise. The outer circles show the trajectory of the foot measured in the gait lab and the inner line represents the trajectory of the robot during performance of the exercise.

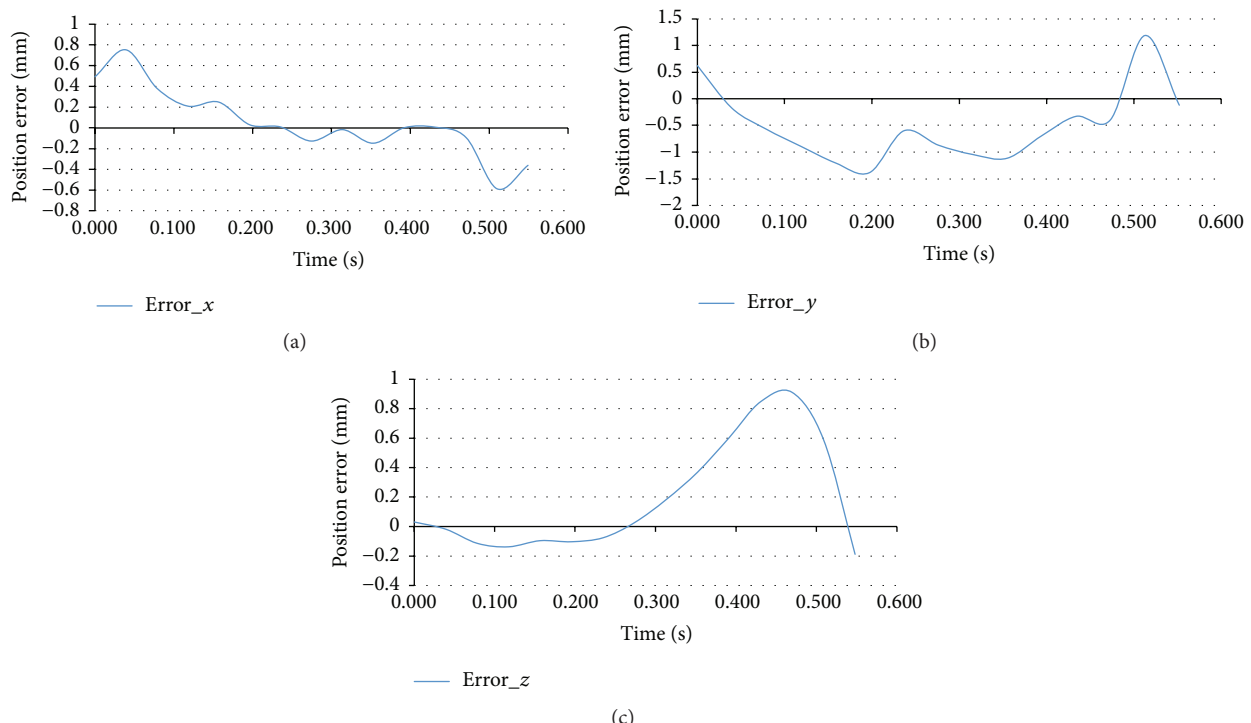


FIGURE 9: (a) Position error of end effector in  $x$ -axis, (b) position error of end effector in  $y$ -axis, and (c) position error of end effector in  $z$ -axis.

robot prototype was developed to track the obtained foot trajectories. The results exhibited a maximum positional error of 1.2 mm in the  $y$ -axis. The robot exhibited good repeatability for the translation in the  $x$ - and  $y$ -axes of the moving platform. Based on kinematic and dynamic analysis, the trajectory of the robot during tracking of the foot trajectories of all patients was simulated in MATLAB, where the results demonstrated that the robot was able to track all of the trajectories within its workspace.

## **Competing Interests**

The authors declare that they have no competing interests.

### Acknowledgments

The authors would like to thank the West Midlands Rehabilitation Centre (WMRC), part of Birmingham Community Healthcare NHS Foundation Trust, for providing gait

measurement laboratory support and Applied Computing and Engineering Ltd. (AC&E) for their sponsorship of this project.

## References

- [1] M. Zhang, T. C. Davies, and S. Xie, "Effectiveness of robot-assisted therapy on ankle rehabilitation—a systematic review," *Journal of NeuroEngineering and Rehabilitation*, vol. 10, no. 1, article 30, 2013.
- [2] C. J. L. Murray and A. D. Lopez, "Global mortality, disability, and the contribution of risk factors: Global Burden of Disease study," *Lancet*, vol. 349, no. 9063, pp. 1436–1442, 1997.
- [3] J. R. Dettori and C. J. Basmania, "Early ankle mobilization—part II: a one-year follow-up of acute, lateral ankle sprains (a randomized clinical trial)," *Military Medicine*, vol. 159, no. 1, pp. 20–24, 1994.
- [4] S. G. Trevino, P. Davis, and P. J. Hecht, "Management of acute and chronic lateral ligament injuries of the ankle," *The Orthopedic Clinics of North America*, vol. 25, no. 1, pp. 1–16, 1994.
- [5] H. I. Krebs, J. J. Palazzolo, L. Dipietro et al., "Rehabilitation robotics: performance-based progressive robot-assisted therapy," *Autonomous Robots*, vol. 15, no. 1, pp. 7–20, 2003.
- [6] S. Mohammed, Y. Amirat, and H. Rifai, "Lower-limb movement assistance through wearable robots: state of the art and challenges," *Advanced Robotics*, vol. 26, no. 1-2, pp. 1–22, 2012.
- [7] N. C. Bejarano, S. Maggioni, L. De Rijcke, C. A. Cifuentes, and D. J. Reinkensmeyer, "Robot-assisted rehabilitation therapy: recovery mechanisms and their implications for machine design," in *Emerging Therapies in Neurorehabilitation II*, pp. 197–223, Springer, 2016.
- [8] O. Stoller, E. D. de Bruin, M. Schindelholz, C. Schuster-Amft, R. A. de Bie, and K. J. Hunt, "Efficacy of feedback-controlled robotics-assisted treadmill exercise to improve cardiovascular fitness early after stroke: a randomized controlled pilot trial," *Journal of Neurologic Physical Therapy*, vol. 39, no. 3, pp. 156–165, 2015.
- [9] I. Díaz, J. J. Gil, and E. Sánchez, "Lower-limb robotic rehabilitation: literature review and challenges," *Journal of Robotics*, vol. 2011, Article ID 759764, 11 pages, 2011.
- [10] W. Meng, Q. Liu, Z. Zhou, Q. Ai, B. Sheng, and S. S. Xie, "Recent development of mechanisms and control strategies for robot-assisted lower limb rehabilitation," *Mechatronics*, vol. 31, pp. 132–145, 2015.
- [11] R. F. Boian, J. E. Deutsch, C. S. Lee, G. C. Burdea, and J. Lewis, "Haptic effects for virtual reality-based post-stroke rehabilitation," in *Proceedings of the 11th Symposium on Haptic Interfaces for Virtual Environment and Teleoperator Systems (HAPTICS '03)*, pp. 247–253, March 2003.
- [12] J. E. Deutsch, C. Paserchia, C. Vecchione et al., "Improved gait and elevation speed of individuals post-stroke after lower extremity training in virtual environments," *Journal of Neurologic Physical Therapy*, vol. 28, no. 4, pp. 185–186, 2004.
- [13] M. Girone, G. Burdea, M. Bouzit, V. Popescu, and J. E. Deutsch, "Orthopedic rehabilitation using the 'Rutgers ankle' interface," in *Studies in Health Technology and Informatics*, vol. 70, pp. 89–95, 2000.
- [14] J. E. Deutsch, J. Latonio, G. C. Burdea, and R. Boian, "Post-stroke rehabilitation with the Rutgers Ankle system: A Case Study," *Presence: Teleoperators and Virtual Environments*, vol. 10, no. 4, pp. 416–430, 2001.
- [15] J. E. Deutsch, J. Latonio, G. Burdea, and R. Boian, "Rehabilitation of musculoskeletal injuries using the Rutgers ankle haptic interface: three case reports," in *Proceedings of the EuroHaptics Conference*, pp. 11–16, Birmingham, UK, July 2001.
- [16] J. E. Deutsch, J. A. Lewis, and G. Burdea, "Technical and patient performance using a virtual reality-integrated telerehabilitation system: preliminary finding," *IEEE Transactions on Neural Systems and Rehabilitation Engineering*, vol. 15, no. 1, pp. 30–35, 2007.
- [17] R. F. Boian, C. S. Lee, J. E. Deutsch, G. Burdea, and J. A. Lewis, "Virtual reality-based system for ankle rehabilitation post stroke," in *Proceedings of the 1st International Workshop Virtual Reality Rehabilitation*, pp. 77–86, 2002.
- [18] G. C. Burdea, D. Cioi, A. Kale, W. E. Janes, S. A. Ross, and J. R. Engsberg, "Robotics and gaming to improve ankle strength, motor control, and function in children with cerebral palsy—a case study series," *IEEE Transactions on Neural Systems and Rehabilitation Engineering*, vol. 21, no. 2, pp. 165–173, 2013.
- [19] P. M. Aubin, M. S. Cowley, and W. R. Ledoux, "Gait simulation via a 6-DOF parallel robot with iterative learning control," *IEEE Transactions on Biomedical Engineering*, vol. 55, no. 3, pp. 1237–1240, 2008.
- [20] J. Jeevamalar and S. Ramabalan, "Optimal trajectory planning for autonomous robots—a review," in *Proceedings of the 1st International Conference on Advances in Engineering, Science and Management (ICAESM-'12)*, pp. 269–275, March 2012.
- [21] H. Rakhodaei, M. Saadat, A. Rastegarpanah, and C. Z. Abdallah, "Path planning of the hybrid parallel robot for ankle rehabilitation," *Robotica*, vol. 34, no. 1, pp. 173–184, 2016.
- [22] H. Rakhodaei, M. Saadat, and A. Rastegarpanah, "Motion simulation of a hybrid parallel robot for ankle rehabilitation," in *Proceedings of the ASME 2014 12th Biennial Conference on Engineering Systems Design and Analysis*, p. V003T17A008, American Society of Mechanical Engineers, Copenhagen, Denmark, July 2014.
- [23] J. A. Saglia, N. G. Tsagarakis, J. S. Dai, and D. G. Caldwell, "A high-performance redundantly actuated parallel mechanism for ankle rehabilitation," *The International Journal of Robotics Research*, vol. 28, no. 9, pp. 1216–1227, 2009.
- [24] L. Marchal-Crespo and D. J. Reinkensmeyer, "Review of control strategies for robotic movement training after neurologic injury," *Journal of NeuroEngineering and Rehabilitation*, vol. 6, no. 1, article 20, 2009.
- [25] J. Hong, C. Chun, and S.-J. Kim, "Gaussian process gait trajectory learning and generation of collision-free motion for assist-as-needed rehabilitation," in *Proceedings of the IEEE-RAS 15th International Conference on Humanoid Robots (Humanoids '15)*, pp. 181–186, Seoul, Republic of Korea, November 2015.
- [26] K. J. Wisneski and M. J. Johnson, "Quantifying kinematics of purposeful movements to real, imagined, or absent functional objects: implications for modelling trajectories for robot-assisted ADL tasks," *Journal of NeuroEngineering and Rehabilitation*, vol. 4, article 7, 2007.
- [27] D. Aoyagi, W. E. Ichinose, S. J. Harkema, D. J. Reinkensmeyer, and J. E. Bobrow, "A robot and control algorithm that can synchronously assist in naturalistic motion during body-weight-supported gait training following neurologic injury," *IEEE Transactions on Neural Systems and Rehabilitation Engineering*, vol. 15, no. 3, pp. 387–400, 2007.
- [28] S. K. Banala, S. K. Agrawal, and J. P. Scholz, "Active Leg Exoskeleton (ALEX) for gait rehabilitation of motor-impaired

- patients," in *Proceedings of the IEEE 10th International Conference on Rehabilitation Robotics (ICORR '07)*, pp. 401–407, Noordwijk, The Netherlands, June 2007.
- [29] T. Nef, M. Mihelj, and R. Riener, "ARMin: a robot for patient-cooperative arm therapy," *Medical & Biological Engineering & Computing*, vol. 45, no. 9, pp. 887–900, 2007.
  - [30] S. Kousidou, N. G. Tsagarakis, C. Smith, and D. G. Caldwell, "Task-oriented biofeedback system for the rehabilitation of the upper limb," in *Proceedings of the IEEE 10th International Conference on Rehabilitation Robotics (ICORR '07)*, pp. 376–384, Noordwijk, The Netherlands, June 2007.
  - [31] C. E. Syrseloudis and I. Z. Emiris, "A parallel robot for ankle rehabilitation-evaluation and its design specifications," in *Proceedings of the 8th IEEE International Conference on BioInformatics and BioEngineering (BIBE '08)*, pp. 1–6, IEEE, Athens, Greece, October 2008.
  - [32] K. Liu, J. M. Fitzgerald, and F. L. Lewis, "Kinematic analysis of a Stewart platform manipulator," *IEEE Transactions on Industrial Electronics*, vol. 40, no. 2, pp. 282–293, 1993.
  - [33] B. Dasgupta and T. S. Mruthyunjaya, "A Newton-Euler formulation for the inverse dynamics of the Stewart platform manipulator," *Mechanism and Machine Theory*, vol. 33, no. 8, pp. 1135–1152, 1998.
  - [34] A. Rastegarpanah, *A methodology for the lower limb robotic rehabilitation system [Ph.D. thesis]*, University of Birmingham, 2016.
  - [35] S. Q. Xie and P. K. Jamwal, "An iterative fuzzy controller for pneumatic muscle driven rehabilitation robot," *Expert Systems with Applications*, vol. 38, no. 7, pp. 8128–8137, 2011.
  - [36] Y. H. Tsoi, S. Q. Xie, and G. D. Mallinson, "Joint force control of parallel robot for ankle rehabilitation," in *Proceedings of the IEEE International Conference on Control and Automation (ICCA '09)*, pp. 1856–1861, Christchurch, New Zealand, December 2009.

## Research Article

# A Critical Analysis of a Hand Orthosis Reverse Engineering and 3D Printing Process

**Gabriele Baronio,<sup>1</sup> Sami Harran,<sup>1</sup> and Alberto Signoroni<sup>2</sup>**

<sup>1</sup>*Dipartimento di Ingegneria Meccanica e Industriale, Università degli Studi di Brescia, Via Branze 38, 25123 Brescia, Italy*

<sup>2</sup>*Dipartimento di Ingegneria dell'Informazione, Università degli Studi di Brescia, Via Branze 38, 25123 Brescia, Italy*

Correspondence should be addressed to Gabriele Baronio; gabriele.baronio@unibs.it

Received 29 April 2016; Revised 5 July 2016; Accepted 13 July 2016

Academic Editor: Tadeusz Mikołajczyk

Copyright © 2016 Gabriele Baronio et al. This is an open access article distributed under the Creative Commons Attribution License, which permits unrestricted use, distribution, and reproduction in any medium, provided the original work is properly cited.

The possibility to realize highly customized orthoses is receiving boost thanks to the widespread diffusion of low-cost 3D printing technologies. However, rapid prototyping (RP) with 3D printers is only the final stage of patient personalized orthotics processes. A reverse engineering (RE) process is in fact essential before RP, to digitize the 3D anatomy of interest and to process the obtained surface with suitable modeling software, in order to produce the virtual solid model of the orthosis to be printed. In this paper, we focus on the specific and demanding case of the customized production of hand orthosis. We design and test the essential steps of the entire production process with particular emphasis on the accurate acquisition of the forearm geometry and on the subsequent production of a printable model of the orthosis. The choice of the various hardware and software tools (3D scanner, modeling software, and FDM printer) is aimed at the mitigation of the design and production costs while guaranteeing suitable levels of data accuracy, process efficiency, and design versatility. Eventually, the proposed method is critically analyzed so that the residual issues and critical aspects are highlighted in order to discuss possible alternative approaches and to derive insightful observations that could guide future research activities.

## 1. Introduction

In the orthopedics and rehabilitation fields the personalization of the patient care is increasingly influenced by the development of new additive manufacturing (AM) technologies and, in particular, by the diffusion of 3D printers. As evidenced in Negi et al. [1] and in Hieu et al. [2], various rapid prototyping (RP) techniques are workable in the medical field. In particular, the use of 3D printers is spreading in the orthotics field and their diffusion is expected to rapidly increase in the near future, given the continuous evolution of available materials and the lowering of the device and production costs of the various AM technologies.

If it is true that the use of AM processes allows attaining high level of customization, this requires that a geometric model of the orthosis to be realized (3D printed) has to be generated first. It is therefore necessary that a reverse engineering (RE) process precedes the implementation phase. The

three main phases of an RE/RP of an orthosis by 3D printing technologies can be outlined as follows:

- (1) Acquisition of the 3D geometry of the interested anatomy using an optical 3D scanner.
- (2) Processing of the acquired data through dedicated software (including CAD 3D modelers).
- (3) Realization of the orthosis using a 3D printer.

While for the third phase suitable (possibly low-cost) hardware can be chosen according to specific needs and among the available and well identifiable AM technologies, the first two phases are instead far from being self-evident. In fact, for the first phase there are a variety of possible acquisition technologies (i.e., structure form motion and dense stereo imaging, time-of-flight range imaging, laser scanners, and structured-light scanners) and modalities (e.g., static multiview or real-time incremental acquisitions) that can correspond to very

different feature combinations in terms of metric accuracy, hardware and software costs, and ease of use.

Likewise, the choice of the most suitable 3D processing and modeling tools strictly depends on a rich set of parameters including the acquisition equipment and the produced data features and the clinical or design requirements and constraints. By the analysis of the literature there are basically two alternative approaches that one can follow:

- (1) As discussed by Paolusek et al. [3], a traditional industrial RE methodology can be followed: this involves the modeling of the details of the orthosis using a generalist 3D CAD modeling software (that can be relatively complex to use and/or expensive to acquire).
- (2) As discussed by Paterson et al. [4] one can instead develop dedicated CAD software for specific orthotic applications (this can be of more immediate use but is extremely targeted and therefore of limited usage, other than likely being more expensive).

Focusing on the orthoses of the upper limbs (forearm, wrist, or hand), we acknowledge the existence of comparative studies regarding the suitability of various 3D printing technologies for the RP of customized orthoses (as described by Paterson et al. [5] and Negi et al. [1]). Less attention, however, is devoted to the development of new acquisition methods of the morphology of the forearm and to the definition of new subsequent data processing and 3D modeling solutions. In fact, a biased interest toward the evolution of 3D printing techniques in the biomedical field is probably justified from its closeness to the final product (e.g., orthoses), while the importance of the development of appropriate technologies for the acquisition and processing of 3D data can be more difficult to perceive, with a natural inclination to simply borrow the knowledge from the RE processes typical of the manufacturing industry.

Forearm, wrist, and hand orthoses are corrective and therapeutic devices that find indications of use for several pathologies and temporal or permanent disability conditions (as described by Jacobs and Austin [6]). With respect to a well assessed variety of prefabricated orthoses, which can be selected simply with respect to their available sizes, a high level of design and manufacturing personalization can be seen as supporting the solution of the problematic aspects related to the level of compliance and tolerability of long-term use of these devices. In fact, a major requirement is the comfort (as described by Andringa et al. [7]), and the high level of orthosis customization, made possible by an accurate anatomical acquisition, is aimed precisely at an optimized adaptation to the anatomy and can be directed to the avoidance of pressure points and other pain and discomfort factors. Moreover, the possibility to include a highly personalized and possibly independent management of the fingers increases the patient care possibilities, for example, in the handling of paraplegic/hemiplegic subjects (antispasticity corrections, poststroke rehabilitation), and can enable solutions not yet considered or experimented, at least on a large scale.

In this work, we implement and critically review the production phases of a hand orthosis (including fingers) within a RE/RP process of industrial type. We use the new optical 3D scanner *Scan-in-a-Box*, some recently developed rigid and deformable scan alignment solutions, the *Rhinoceros* CAD software and a *Stratasys Dimension BST 1200es* 3D printer. These elements were chosen because they can be all considered and located in a low-cost range with respect to the spectrum of available technologies while, taken both singularly and together, they ensure a high level of accuracy and good versatility of the target RE/RP processes. Building on this framework, a further objective of this paper is to highlight the critical issues of traditional RE processes (meant and developed for industrial uses) once applied to the targeted medical application. The recommendations coming from this work are intended to promote and guide further research and experimentations efforts. Particular attention will be given to the 3D data processing phases.

## 2. Materials and Methods

In this section we go through the production process of a personalized hand orthoses starting from the reverse engineering of the patient anatomy and according to the three steps listed above.

**2.1. 3D Anatomy Acquisition.** The purpose of this phase is to produce a faithful anatomical digitization of the hand/wrist complex using an optical scanner that offers an interesting cost-accuracy combination. The scanning takes place with respect to a free standing or partially sustained arm (we neither block the arm nor the hand). Therefore, it is necessary that the acquisition would not be invalidated by the presence of slight involuntary movements, with respect to a reference position, that unavoidably occur during the scanning session.

We operated with the new low-cost structured-light optical 3D scanner *Scan-in-a-Box* (by OpenTechnologies srl, Italy (<http://www.scaninabox.com/>)) to acquire the range images that contribute to the creation of the triangular mesh of the lower part of the limb. This lightweight reconfigurable scanner performs high-resolution structured-light scans in about 4 seconds, guaranteeing a metric accuracy till 0.1% with respect to the object size (in our case this means about 0.2 mm). The scanner comes with interactive software that handles the measuring process and processes the acquired data, including range image cleaning, alignment, mesh generation, basic mesh repair tools, and various data exporting formats.

The 3D mesh (usually in STL format) is required by the subsequent design and printing stages of the orthosis. Before that, a cumulative point cloud is created by the alignment of the different range scans acquired from various viewpoints to guarantee the complete coverage of the anatomic region of interest. In more detail, we report an example where the following steps have been realized:

- (i) Whole anatomy coverage is obtained with 8 acquisitions of the forearm positioned on a chair armrest from 4 vantage points. The scanner is repositioned

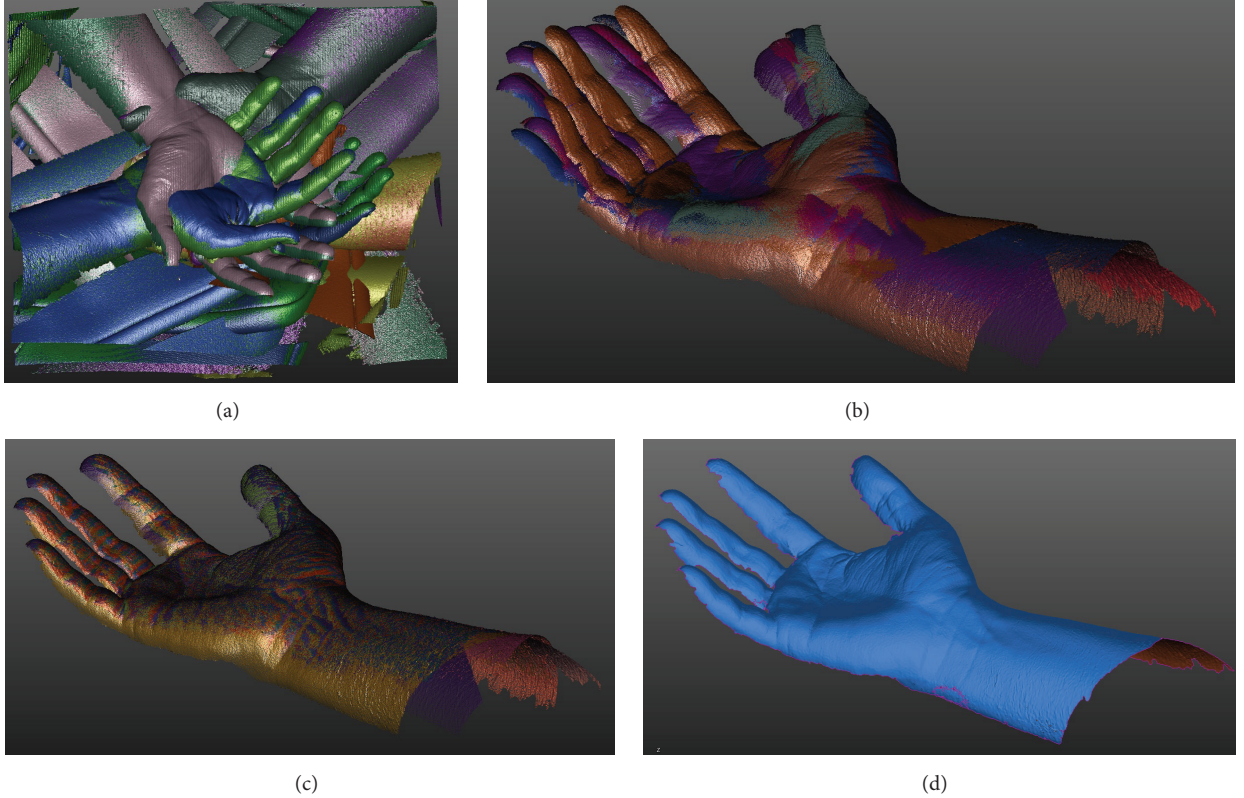


FIGURE 1: The 3D acquisition phase.

around the limb, according to the next needed vantage point, for a total scanning time of approximately 2 minutes. This is compatible with many clinical situations. However, since each single range image is referenced with its own coordinate system, the various scans need to be aligned (Figure 1(a)).

- (ii) After cleaning each scan from the unwanted background (using the scanner software), a completely automated coarse alignment of the range images was obtained by the technique described in Bonarrigo et al. [8] which guarantees reliable and robust alignments, based on the automatic detection of correspondences between local geometric features, which are robust to viewpoint changes and partial deformations. Given the low number of needed scans this step can be possibly substituted by facilitated manual alignment provided by the scanner software at an additional time cost of about 10 min.

The resulting aligned image set is shown in Figure 1(b).

- (iii) The impossibility to maintain a perfectly fixed position during the scanning time determines a difference between the positions of the fingers of different range images. This is clearly visible in Figure 1(b). We solved this problem by applying the patch-wise as-rigid-as-possible deformable alignment technique described in Bonarrigo et al. [9] that allows the

deformable alignment of various scans with respect to a reference one. This method is able to compensate for various kinds of motion and deformation that the acquired data can exhibit, which is achieved by a nonlinear, physics-inspired deformation regularization. The surface is discretized into a hierarchy of partially overlapping patches, for each of which a distinct rigid transformation is found by minimizing a global objective function that takes into account both the need for accurate alignment and for the regularity of the deformation field. The resulting rigid transformations are then extended to all sample points in a rigid manner using dual quaternion interpolation. As a result of this as-rigid-as-possible deformation this dynamic registration avoids unnecessary distortion and faithfully preserves geometric features. As it can be seen in Figure 1(c), this allows proper motion-compensated alignment without any detrimental effect on the geometric accuracy.

- (iv) The scanner software allows the direct conversion of the aligned scans (i.e., the cumulative point cloud) in a 3D triangular mesh (Figure 1(d)). Such a mesh is required for the subsequent modeling of the customized hand orthosis by a 3D CAD software.
- (v) The final mesh has been optimized (border regularization) and repaired from its defects by the automatic fixing tool RameshCleaner (as described by Centin and Signoroni [10]). This is a structured set of effective

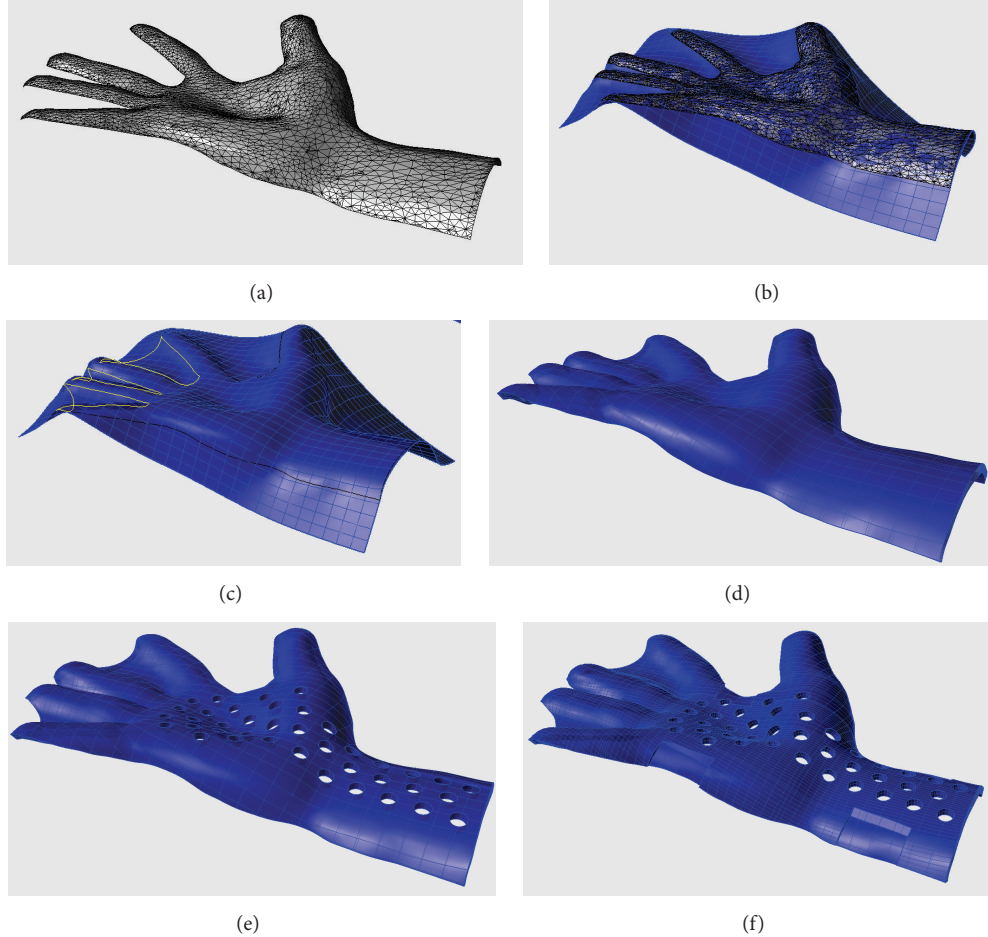


FIGURE 2: The 3D modeling phase.

fixing strategies that maximally preserve the original data while effectively solving several important and typical mesh weakness (possible holes, degenerate triangles, foldovers, or spikes).

Other optimization operations were not necessary. The total time to accomplish all the above operations is about 1 h 30 min, subdivided as follows: 15 min for multipose hand acquisition with data cleaning and rigid alignment, 15 min for fine deformable alignment, and about 1 h for mesh creation, regularization, and repair.

**2.2. 3D CAD Modeling of the Hand Orthosis.** The *Rhinoceros* CAD software was used to import the triangular mesh (STL) previously obtained and, using its dedicated tools, to derive the NURBS representation of the surface. Then, by modeling the reconstructed surface, the solid geometry of the orthosis to be printed was obtained. In particular, the operations that have been carried out are as follows:

- (i) An offset of 2-3 mm is applied to the imported mesh. This is necessary to create an adaptation space between the hand and the inner surface of the orthosis, in order to avoid discomfort and to prevent/tolerate the physiological swelling (Figure 2(a)).

- (ii) The so processed triangular mesh is automatically converted in a mathematical NURBS surface by the dedicated tool (*RhinoResurf*) integrated in the CAD software (Figure 2(b)).

For the NURBS conversion of the previously optimized mesh we used the following parameters of the *RhinoResurf* plug-in: max tolerance 0.5 mm, smooth “medium.” With these coefficients the average (max) mesh to surface point deviation is 0.076 mm (0.497 mm).

The parameters of the NURBS surface obtained by the reconstruction are

“U”: degree = 3 num. CV = 31 ( $0 \leq U \leq 203.085$ ),

“V”: degree = 3 num. CV = 31 ( $0 \leq V \leq 296.855$ ).

- (iii) Extraction of the projection curve of the mesh border on the CAD surface (shape of the hand) and design of closing curves projected on the CAD surface over the finger area (Figure 2(c)). These curves are needed to create a connecting surface between the various fingers in order to stiffen the orthosis.

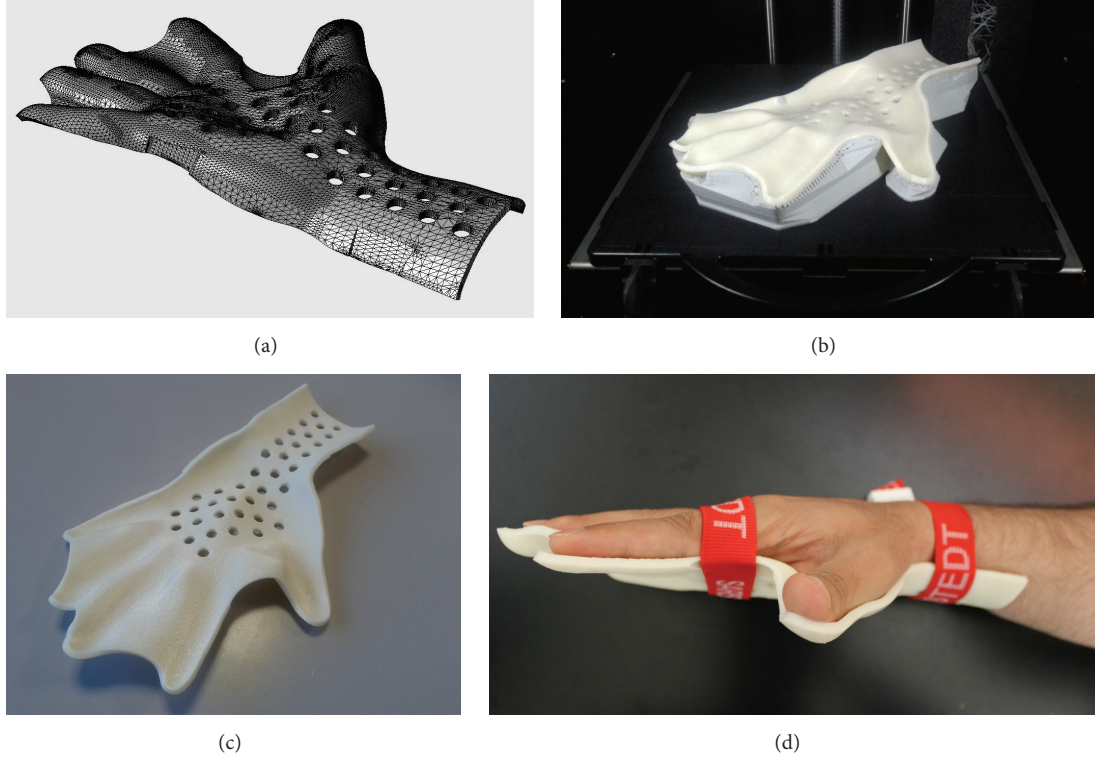


FIGURE 3: The 3D printing phase.

- (iv) Shaped cut of the CAD surface and its thickening of 4 mm (solid offset operation) to obtain the solid volume of the orthosis (Figure 2(d)).
- (v) In order to realize lightening and skin breathing holes on the orthosis, in the forearm and palm areas, a repeated volume subtraction operation (e.g., cylinder intersections) has been performed (Figure 2(e)).
- (vi) In order to realize the housing grooves for the fastening bands, another volume subtraction operation was performed on the orthosis where CAD model, at this point, is completed (Figure 2(f)).

The total time to accomplish all the above operations is about 2 hours (this can vary depending on the skillfulness of the operator).

**2.3. Back-Conversion of the CAD Orthosis Model in a Triangular Mesh for 3D Printing.** In the last phase of the orthosis realization process, we must convert back and export the optimized 3D CAD model in a triangular mesh (Figure 3(a)) format (STL) which is required for 3D printing, as depicted in Figures 3(b), 3(c), and 3(d). In our case, a FDM printer (Stratasys “Dimension BST 1200es”) employing ABS material (ABSplus, tensile strength: 37 MPa) was used with a layer thickness of 0.254 mm and build size 254 × 254 × 305 mm.

The forearm accommodation of the printed prototype does not have an optimal length (Figure 3(d)); this was only due to the limited available printing area of the used printer (Figure 3(b)).

The total printing time was about 11 hours. Summing up all the acquisition, modeling, and printing phases, we obtained lead times of about 1 working day (dominated by the printing time). This can be considered tolerable and compatible with the clinical and patient needs. Possible finishing phases are not considered here, but the reader can refer to Palousek et al. [3].

### 3. Discussion

On one hand, we can look at the methodology described above as geometrically satisfactory and as an inspiring way for the production of hand orthoses that must lead to a favorable trade-off between high-accuracy (in the reproduction of the patient anatomy) and low-cost (of both hardware and software tools throughout the production chain) requirements.

An acquisition of the hand and fingers anatomy with submillimeter accuracy, as the one allowed by the selected acquisition and processing pipeline, is undeniably a good starting point for the design and production of orthoses with a high degree of comfort and tolerability and to give the opportunity for clinicians to indicate pressure zones and to create orthoses fully responsive to the therapeutic needs, other than enabling the faithful translation of therapeutic indications also for the fingers.

However, our work is significant also because it allows highlighting some critical aspects of the process that we want to examine in the following discussion. We believe that the production of highly personalized orthoses is still very

challenging and presents open issues that can be addressed and solved only through a serious and deeply interdisciplinary work between different expertise in the fields of orthopedics and rehabilitation, mechanical RE and material science, computer vision, and geometry processing.

**3.1. Scanning of the Forearm and Scan Alignment.** The morphological complexity of the hand requires the acquisition of more range images from different vantage points. It is therefore necessary that the subjects keep the limb and the hand steady for a certain amount of time (one to two minutes). If the hand is not firmly constrained, involuntary movements generate scan misalignments especially in the finger area. The use of an innovative deformable alignment technique (as described by Bonarrigo et al. [9]) allowed us to overcome what is usually considered a major problem in the use of static optical scanners for body scans (as described by Paterson et al. [11], Bibb et al. [12], and Tzou et al. [13]). The scanner used in this work has also the additional feature of being lightweight and therefore easily repositionable around the limb.

Possible alternative scanning techniques are those operating by stereophotogrammetric principles. They usually are specific devices able to shoot, in a split-second (so that motion problems are inherently solved), simultaneous multiview images which estimate and generate a 3D surface (as described by Paterson et al. [11] and Tzou et al. [13]). However, these dedicated systems can be very expensive and may even suffer from some versatility and surface coverage issues, especially for the reconstruction of complex geometries, as in the case of the hand fingers and even limiting to single-side acquisitions.

Another more recent alternative consists in the so-called real-time scanning technologies (examples of devices on the market are: *Health Care Partner 3D* from Creaform (<http://www.creaform3d.com/>), *Artec Eva* from Artec3D (<https://www.artec3d.com/>), and *Insight3* from OpenTechnologies (<http://www.scanner3d.it/>)) which are usually portable and handy optical scanner devices operating with fixed light patterns, where the acquired views are continuously accumulated (similarly to what described in Izadi et al. [14]) while the scanner is smoothly moved around the object of interest. Although the accumulation process does not allow too rapid movements, the scanning can be faster compared to what is obtained using static devices, but not such as to avoid body motion issues. In this case, the nominal scanner accuracy can be compromised because, depending on the entity of the motion, the compensation mechanisms within the view accumulation process can introduce nonnegligible deviations from the true geometry. This can generate an orthosis that causes discomfort or even unwanted compressions on some body parts. In addition, these systems can still be widely more expensive with respect the one selected in this work.

**3.2. 3D CAD Modeling of the Orthosis.** The use of a 3D CAD modeling software is typical in a RE environment. However, its use requires specific skills that are not that diffuse among clinicians and orthopedic/orthotics technicians. Thus, the

rehabilitation facility (either a clinical structure or an external service), even if it is equipped with appropriate hardware (3D scanner and 3D printer), could not be self-sufficient (unless investing in skilled CAD technicians) in reaching a cost-efficient production of customized orthosis using AM processes.

Conversely, the potential of traditional CAD systems is only marginally exploited in the considered processes: the modeling procedures only needed basic commands (offset, Figure 2(a), thickening, Figure 2(d), cut, Figure 2(e), etc.) or the execution of very specific tasks (reinforcement of the finger area, Figure 2(c)). Interestingly, the most complex phase remains the conversion of the triangular mesh into a mathematical surface representation (Figure 2(b)). This operation is usually left to a specific plug-in, whose quality is a main guiding factor for the choice of the CAD system.

It is evident that there is a 3D domain transition (STL-CAD-STL) which is not strictly required from the 3D printing point of view, but that is necessary for the type of software (3D CAD) used to process the data within the typical RE approach. However, this can be seen as an extra burden, both procedural and economical, for the orthoses design and production chain. The ability to perform basic modeling operations directly on the 3D mesh seems then to emerge as a particularly interesting and desirable opportunity.

The possibility to directly operate on the mesh produced by the scanner through an appropriate and handy interface would also make these editing tools usable even by nontechnical CAD staff. As a matter of fact, systems that directly work on meshes already exist but either they are general purpose creative mesh sculpting tools (e.g., Autodesk Meshmixer, <http://www.meshmixer.com/>), not specifically conceived for the clinical use, or they are clinically oriented tools, but in this case they are usually very specific and verticalized on single applications. This is why there is still room for the development of mesh editing systems that might be easily exploited, through appropriate interfaces, by practitioners and technicians in the clinical field for the design and production of printable STL models of orthoses.

**3.3. 3D Printing.** The use of a low-cost 3D printer (FDM technology) can lead to restrictions in the geometric definition of some details. For example, the size of the lightening and aeration holes on the orthosis could be optimized (smaller or different textures) according to the quality, resolution and materials of the selected printer (see Paterson et al. [4]). Alternative but currently more expensive 3D printing technologies can yield orthosis with higher resolutions and made of materials with better performance than ABS.

**3.4. Further Considerations.** In rehabilitation, when, for example, spasticity symptoms (either caused by cerebral palsy or stroke outcomes) must be treated, it is not always possible to acquire the scan of a freestanding hand in the desired working position of the orthosis. In these cases, the clinicians make use of tapes and provisional supporting systems to acquire the forearm and the hand anatomy in the desired position.

This, however, may not always be done in a simple and accurate way, so that the availability of suitable mesh deformation tools (similar to those already seen or specifically informed by an articulated deformation model) could become a great opportunity for the practitioners. For example, this would enable the possibility to implement angular adjustment of the position of the fingers according to, possibly progressive, corrective criteria. Such adjustments could also be directed to the reduction of comfort issues affecting the patient compliance (as described by Andringa et al. [7]).

## 4. Conclusions

The analysis and the experimental considerations we made about the proposed hand orthosis RE/RP process lead us to the following main conclusions and insights:

- (i) For the digitization of the forearm anatomy we have identified low-cost optical 3D scanning solution able to guarantee a high degree of accuracy of the single scans.
- (ii) A feature based multiview automatic coarse registration approach followed by a deformation alignment software can be both used to recover a faithful and accurate alignment of the scans, including the complex finger area, in a resilient way with respect to unavoidable slight movements of the limb and fingers. It is therefore not strictly necessary (unless specifically required by the clinician for correction purposes) to fix the limb and fingers with tape or special retainer systems during the acquisition.
- (iii) The use of a 3D CAD modeler to import and process the triangular mesh obtained as a product of the anatomy digitization would not be necessary if there was a software able to perform the needed modeling operations directly on the triangular mesh (STL).
- (iv) This software might also include the possibility to correct, working on the acquired anatomy, the angular position of the fingers according to the rehabilitative needs identified by the clinicians. Most of the works in the literature consider processes oriented to the production of customized wrist immobilization splints, where the fingers are deliberately left free to move. However, due to the population aging, it is becoming increasingly important to also treat people with stroke outcomes. For these subjects the orthotic rehabilitation is directed to the treatment of the spasticity of the entire wrist-hand complex and thus also of the fingers.

These considerations reveal several open issues and suggest the need to continue with research studies directed to develop new data processing software and cost-efficient RE/RP methodologies to give better answers to the specific clinical requirements and to the usability needs coming from the orthotics technicians.

## Competing Interests

The authors declare that they have no competing interests.

## References

- [1] S. Negi, S. Dhiman, and R. K. Sharma, "Basics and applications of rapid prototyping medical models," *Rapid Prototyping Journal*, vol. 20, no. 3, pp. 256–267, 2014.
- [2] L. C. Hieu, J. V. Sloten, L.T. Hung et al., "Medical reverse engineering applications and methods," in *Proceedings of the 2nd International Conference on Innovations, Recent Trends and Challenges in Mechatronics, Mechanical Engineering and New High-Tech Products Development (MECAHITECH '10)*, pp. 232–246, Bucharest, Romania, September 2010.
- [3] D. Palousek, J. Rosicky, D. Koutny, P. Stoklasek, and T. Navrat, "Pilot study of the wrist orthosis design process," *Rapid Prototyping Journal*, vol. 20, no. 1, pp. 27–32, 2014.
- [4] A. M. Paterson, R. J. Bibb, and R. I. Campbell, "Evaluation of a digitised splinting approach with multi-material functionality using additive manufacturing technologies," in *Proceedings of the 23rd Annual International Solid Freeform Fabrication Symposium*, pp. 656–672, August 2012.
- [5] A. M. Paterson, R. Bibb, R. I. Campbell, and G. Bingham, "Comparing additive manufacturing technologies for customised wrist splints," *Rapid Prototyping Journal*, vol. 21, no. 3, pp. 230–243, 2015.
- [6] M. A. Jacobs and N. M. Austin, *Orthotic Intervention for the Hand and Upper Extremity: Splinting Principles and Process*, Lippincott Williams & Wilkins, Philadelphia, Pa, USA, 2nd edition, 2014.
- [7] A. Andringa, I. van de Port, and J.-W. Meijer, "Long-term use of a static hand-wrist orthosis in chronic stroke patients: a pilot study," *Stroke Research and Treatment*, vol. 2013, Article ID 546093, 5 pages, 2013.
- [8] F. Bonarrigo, A. Signoroni, and R. Leonardi, "Multi-view alignment with database of features for an improved usage of high-end 3D scanners," *EURASIP Journal on Advances in Signal Processing*, vol. 2012, no. 1, article 148, 2012.
- [9] F. Bonarrigo, A. Signoroni, and M. Botsch, "Deformable registration using patch-wise shape matching," *Graphical Models*, vol. 76, no. 5, pp. 554–565, 2014.
- [10] M. Centin and A. Signoroni, "RameshCleaner: conservative fixing of triangular meshes," in *Proceedings of the STAG: Smart Tools & Apps for Graphics*, 2015.
- [11] A. M. J. Paterson, R. J. Bibb, and R. I. Campbell, "A review of existing anatomical data capture methods to support the mass customisation of wrist splints," *Virtual and Physical Prototyping*, vol. 5, no. 4, pp. 201–207, 2010.
- [12] R. Bibb, P. Freeman, R. Brown, A. Sugar, P. Evans, and A. Bocca, "An investigation of three-dimensional scanning of human body surfaces and its use in the design and manufacture of prostheses," *Proceedings of the Institution of Mechanical Engineers, Part H: Journal of Engineering in Medicine*, vol. 214, no. 6, pp. 589–594, 2000.
- [13] C.-H. J. Tzou, N. M. Arnter, I. Pona et al., "Comparison of three-dimensional surface-imaging systems," *Journal of Plastic, Reconstructive and Aesthetic Surgery*, vol. 67, no. 4, pp. 489–497, 2014.
- [14] S. Izadi, D. Kim, O. Hilliges et al., "KinectFusion: real-time 3D reconstruction and interaction using a moving depth camera," in *Proceedings of the 24th Annual ACM Symposium on User Interface Software and Technology (UIST '11)*, pp. 559–568, 2011.

## Research Article

# Design Concepts of Polycarbonate-Based Intervertebral Lumbar Cages: Finite Element Analysis and Compression Testing

J. Obedt Figueroa-Cavazos,<sup>1</sup> Eduardo Flores-Villalba,<sup>1</sup> José A. Diaz-Elizondo,<sup>2</sup> Oscar Martínez-Romero,<sup>1</sup> Ciro A. Rodríguez,<sup>1</sup> and Héctor R. Siller<sup>1</sup>

<sup>1</sup>Tecnológico de Monterrey, Escuela de Ingeniería y Ciencias, 64849 Monterrey, NL, Mexico

<sup>2</sup>Tecnológico de Monterrey, Escuela de Medicina, 64710 Monterrey, NL, Mexico

Correspondence should be addressed to Héctor R. Siller; [hector.siller@itesm.mx](mailto:hector.siller@itesm.mx)

Received 16 November 2015; Revised 29 March 2016; Accepted 18 April 2016

Academic Editor: Tadeusz Mikołajczyk

Copyright © 2016 J. Obedt Figueroa-Cavazos et al. This is an open access article distributed under the Creative Commons Attribution License, which permits unrestricted use, distribution, and reproduction in any medium, provided the original work is properly cited.

This work explores the viability of 3D printed intervertebral lumbar cages based on biocompatible polycarbonate (PC-ISO® material). Several design concepts are proposed for the generation of patient-specific intervertebral lumbar cages. The 3D printed material achieved compressive yield strength of 55 MPa under a specific combination of manufacturing parameters. The literature recommends a reference load of 4,000 N for design of intervertebral lumbar cages. Under compression testing conditions, the proposed design concepts withstand between 7,500 and 10,000 N of load before showing yielding. Although some stress concentration regions were found during analysis, the overall viability of the proposed design concepts was validated.

## 1. Introduction

The combination of biotechnology and 3D printing has led to the rise of 3D bioprinting, which is a processing technique that promises to solve critical issues while finding printable biomaterials, increasing the capacity of precise positioning and including cell sources, in order to be successfully applied in diagnosis, personalized medicine, and regenerative medicine [1]. Literature that demonstrates the disruptiveness of this group of applications is spread out in several fields. Radenkovic et al. suggested the idea of manufacturing personalized human hollow organs with lower architectural complexity using detailed patient information, acquired by medical imaging, appropriate cell type, and 3D printing technology [2]. Other works showed the potential of medical and industrial applications of several classes of 3D printing techniques that may be useful for attending the future demand for organ transplants. For example, Yoo made a comparison among different 3D bioprinting technologies in order to evaluate their impact on human health and medical devices industry [3]. Visser et al. stated that the potential application of 3D bioprinting in medicine will evolve into tissue printing in the near future [4].

3D printing of implants, prosthesis, and other medical devices can be considered an important stage of the full development of 3D bioprinting applications. Particularly, design of prosthesis and implants is nowadays embracing the use of 3D printing technologies as FDM (Fused Deposition Modeling), in order to solve the need for customization and the need for providing a fast response in surgical interventions [5]. Some previous works show that it is possible to satisfy the main features required in customized medical devices such as strength, sterility, dimensional stability, and safety. For example, Rankin et al. used a FDM machine for surgical retractors prototyping. This prototype was sterilized and tolerated the tangential force needed to fulfill the requirements before failure, both before and after exposure to sterilization [6].

A specific case of the need of customized implants is column surgery. This is performed in order to ease pathologies associated with back pain that are sometimes caused by deterioration of surrounding fibrous ring of intervertebral discs, resulting in spinal disc herniation. The column surgery that deals with this illness is usually known as spinal fusion surgery, where the vertebrae gradually fuse into a single body with the introduction of an intervertebral cage implant. Spinal fusion is done most commonly in the lumbar region

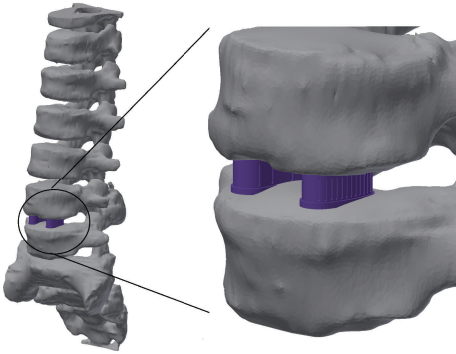


FIGURE 1: Representation of the lumbar cage implants (vertebrae images courtesy of Centro de Tecnologia da Informação Renato Archer).

of the spine, but it is also used to treat cervical and thoracic regions. The main function of an intervertebral cage implant is to fill the intervertebral space in order to facilitate the process of osseointegration and to provide mechanical support through an optimal load distribution and an interbody fusion balance fixation.

Figure 1 shows the conceptual representation of an intervertebral cage implant system. Typically, intervertebral cage implants are manufactured with medical grade titanium alloys (Ti6Al4V), polyether ether ketone (PEEK), and composite materials. But now, with the appearance of 3D printing and Additive Manufacturing Technologies like Fusion Deposition Modeling (FDM), the potential for developing customer oriented and reliable cage implants is higher. The following sections of this work explain the development of a process chain for taking advantage of FDM in column surgery implants customization.

## 2. Related Work

There are a limited number of research studies that explore the design and rapid manufacturing of patient-specific implants for column surgery. de Beer and van der Merwe developed a study of the rapid manufacturing of metallic implants. They used computed tomography (CT), direct laser metal sintering (DMLS), and mechanical testing in order to propose a process chain for customization of intervertebral disc implants [7]. In the same matter, Domanski et al. used three Additive Manufacturing Technologies: Fused Deposition Modeling, Powder Based 3D Printing (3DP), and Selective Laser Melting (SLM). They performed Finite Element Analysis for strength validation and they compared surface roughness of each prototype developed [8]. Espalin et al. suggested the use of FDM for the freeform manufacturing of several types of implants. They concentrated their research approach on cranial reconstruction, but they suggested this technique for the customization of orthopedic spacers [9]. Chougule et al. used noninvasive imaging, reverse engineering, and FDM for the development of specific implants for minimum invasive spine surgeries. They suggested that this process chain could provide valuable medical information and powerful diagnostic tool for surgeons to understand the

complex internal anatomy of the patient [10]. A work that precedes the one presented here explores the use of FDM and common 3D printing machinery, in the development of design concepts of polymeric spinal surgery implants [11]. It was an exploratory study that evaluated the feasibility of implant customization with this kind of techniques and lays the foundations of the present work.

## 3. Objective

There is a clear need to evaluate the viability of the use of 3D printing for the customization of column surgery implants. Thus, the main objective of this research is to validate a series of design concepts of a specific case of column implants (called “intervertebral lumbar cages”) with the aid of FDM, computational simulations, and experimental testing. Furthermore, this work is intended to lay the basis for the implementation of these medical devices in orthopedic surgeries.

## 4. Materials and Methods

This section covers the set-up of a proposed process chain for lumbar cage material selection, design, prototyping through FDM, mechanical testing, and Finite Element Analysis.

**4.1. Materials.** The proposed polymer for this research is PC-ISO (polycarbonate-ISO), an industrial thermoplastic that can be sterilized by several methods like ethylene oxide and gamma radiation, according to the work of Perez et al. In this work sterility testing was performed with successful results for material deposited with FDM process [12]. Cunha et al. evaluated safety and radiation attenuation properties of PC-ISO material and established a method for its clinical use in customized Gynecological Brachytherapy Applicators. The work concluded that PC-ISO is a suitable material for this application in a clinical setting [13].

In the case of the material biocompatibility, there are several studies ordered by the material supplier that confirm that the material is not toxic, does not present allergenic potential, and does not have irritant effects. Among the studies mentioned above there is, for example, the ISO Acute Systemic Injection Test, which was designed for screening PC-ISO extracts for potential toxic effects as a result of a single-dose systemic injection in mice. The study confirmed that the animals did not present signs of toxicity in comparison with the control. Regarding mechanical properties of the chosen material, it has a specified ultimate tensile strength of 57 MPa and a modulus of elasticity of 2 GPa, properties that made this polymer competitive with other engineered materials for implants [11].

**4.2. Prototypes.** The implant design for FDM took into account several design guidelines for the appropriate deposition of the polymeric material, in order to improve its mechanical performance during tensile or compressive testing and for increasing the dimensional and geometrical accuracy. Some of these design guidelines were formulated by Ahn et al., based on the results of extensive experimentation [14]. Derived from that work, the following guidelines are

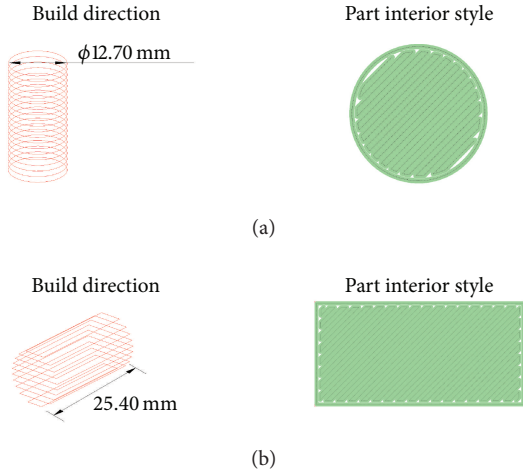


FIGURE 2: Build direction and part interior style of cylindrical test specimens: (a) transverse-vertical and (b) horizontal-axial configurations.

TABLE 1: System specifications of FDM machine.

Configuration	
Build envelope (XYZ)	$406 \times 355 \times 406\text{ mm}$
Material delivery	Two build material canisters 1508 cc Two support material canisters 1508 cc Autochangeover between canisters
Material options	PC-ISO
Layer thickness	0.330 mm 0.254 mm 0.178 mm
Support structure	Breakaway Support System (BASS™)

used in this particular case study:

- (i) A negative air gap, meaning that two FDM layers partially occupy the same space, will increase both strength and stiffness.
- (ii) The build orientation could improve the part accuracy and strength.

Prior to the exploration of patient-specific lumbar cage process chain, cylindrical specimens with two different configurations of build directions were subject to compression strength testing (Figure 2). This procedure was carried out as screening experimentation in order to establish the material mechanical properties for a Finite Element Analysis of the lumbar cage concepts. For the manufacture of the cylindrical specimens and implant design concepts, a FDM machine Stratasys Fortus 400mc was used and two different machine nozzles were configured for the deposition process (Tables 1 and 2). According to the supplier of PC-ISO material, the specific gravity is 1.20, which is equivalent to  $0.0012\text{ g/mm}^3$  in density [15]. Taking as reference this value and the final weights of the cylindrical specimens, the fill percentage obtained with 0.30 mm nozzle is approximately 88% and the

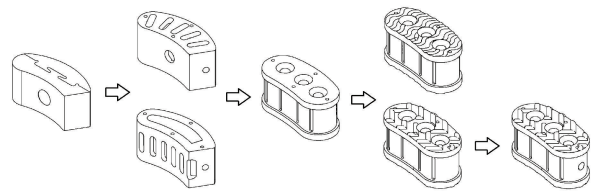


FIGURE 3: Evolution of lumbar cage design concepts.

TABLE 2: Fused Deposition Modeling process specifications.

Nozzle diameter	0.30 mm	0.40 mm
Slice height	0.17 mm	0.25 mm
Contour width	0.35 mm	0.50 mm
Part raster width	0.35 mm	0.50 mm
Visible surface raster	0.30 mm	0.43 mm
Internal raster	0.40 mm	0.61 mm

fill percentage obtained with the 0.40 mm nozzle is approximately 92%, which may influence the strength behavior.

The design criteria for lumbar cage geometries were established by the analysis of patents and commercial products, in which the predominant factor found was the load distribution for providing minimum damage to vertebrae [16–19].

It is important to point out that the mechanical response to fatigue testing must be considered in further research since there is evidence in the literature that repetitive loading can cause vulnerability to column mechanical damage [20], and there is limited fatigue data in the literature for FDM deposited materials [21].

The evolution of all design attempts is shown in Figure 3, in which the geometries presented in previous research are also exhibited [11].

In this work, four different lumbar cage design concepts are proposed, as an optimization alternative in the search for appropriate 3D printed implants. These lumbar cage design concepts were tested in a similar set-up to that used for cylindrical specimens. Solid models of the proposed lumbar cages were drawn using a generic CAD tool. The dimensions ranges of the prototypes were about 13.4 mm in width and 28.7 mm in length, having a height of 13 millimeters. Also, all the designs included geometrical features that facilitate osseointegration. It is important to point out that the design concepts include antiskid systems required for appropriate implant fixation, but these geometrical features could generate stress concentration. Figure 4 presents the proposed lumbar cage design: (a) a flat lumbar cage that does not have an antiskid system; (b) a lumbar cage with an antiskid system with undulating features; (c) a lumbar cage with antiskid system with triangular features; and (d) the same geometry that proposed lumbar cage design (c), but with a handling hole in the side view (the handling hole is used to hold the lumbar cage during implantation).

**4.3. Compression Strength Testing.** Compressive strength tests for each cylindrical specimen and each lumbar cage design concept were conducted using a Shimadzu Universal

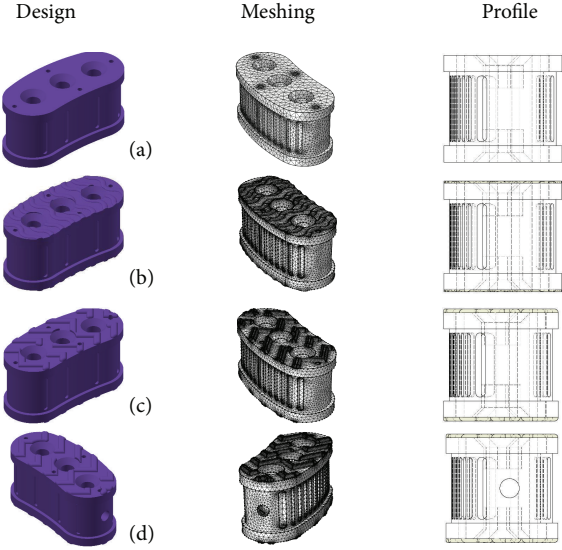


FIGURE 4: Proposed lumbar cage new designs.

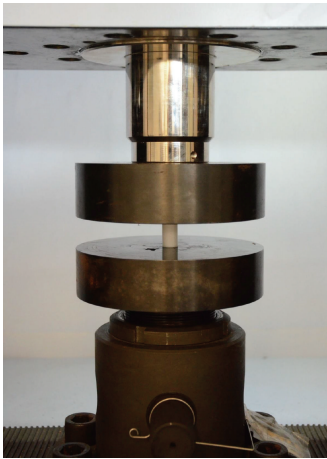


FIGURE 5: Test system equipped with a 25 kN load cell.

Testing Machine equipped with a 25 kN load cell. The tests performed on cylindrical specimens were based on the “ASTM.D695.2010, Standard Test Method for Compressive Properties of Rigid Plastics” [22], using 6 mm/min as crosshead speed (Figure 5).

**4.4. Simulation Settings.** The Finite Element Analysis (FEA) was performed with the aid of COMSOL Multiphysics 4.3 software, to automatically generate tetrahedral elements and for performing the computational simulation. It is a common practice to use automatic tetrahedral mesh generators to discretize complex 3D structural components. This type of mesh generators can handle complex geometries with a minimum of human intervention (as compared to, e.g., the manual generation of a mesh of hexahedral elements). The solver used to perform the 3D calculations was embedded in the software. Mesh size was predefined in a range of 0.286 and 2.290 mm with a maximum element growth rate

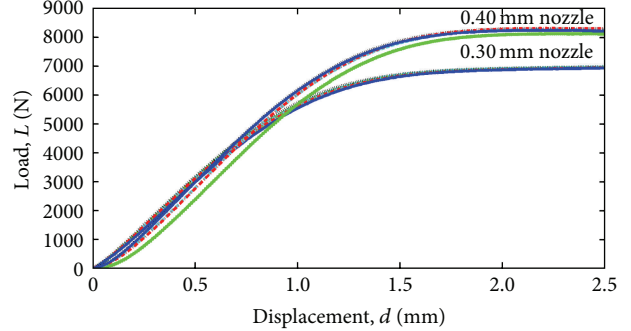


FIGURE 6: Comparison of the compression test of PC-ISO cylindrical test specimens, printed with 0.30 mm and 0.40 nozzle configuration.

TABLE 3: Mechanical properties of PC-ISO cylindrical test specimens.

Mechanical properties	Unit	0.30 mm	0.40 mm
Compressive yield strength	MPa	40	55
Young's modulus	GPa	1.2220	1.2580
Poisson's ratio	1	0.3928	0.4287
Density	Kg/m <sup>3</sup>	1,060	1,110

of 1.45. Mechanical properties of the proposed lumbar cages were assumed to be homogeneous and linear elastic. The mechanical properties of Table 3 were taken as simulation references for each proposed prototype.

**4.5. Reference Column Load.** In order to establish a good approximation of the load that must be used for simulating average column loads, an additional literature review was made. Wilke et al. estimated an interdiscal pressure of 1.8 MPa, equivalent of 3,240 N in a disc area of 1800 mm<sup>2</sup>, in the L4-L5 disc while an average person was holding a 20 kg object 600 mm away from the chest [23]. Schultz et al. estimated that the interdiscal pressure varies depending on the body position and type of activity, taking values from 0.270 MPa (486 N of load over 1800 mm<sup>2</sup>) in a relaxed standing position to 1.62 MPa (2,916 N of load over 1800 mm<sup>2</sup>) in the most strenuous task examined [24]. Therefore, considering the average loads from the literature, a 4,000 N axial force was taken as reference load and the bottom face of the prototype was rigidly fixed for motion constraint.

## 5. Results and Discussion

**5.1. Compression Strength Testing.** The results of this screening experimentation for horizontal-axial build configuration were discarded since they presented lower strength behavior (7,800 N) in comparison to those with transverse-vertical build configuration for similar conditions (8,300 N). Figure 6 shows results of the compressive strength test of PC-ISO specimens manufactured by 0.30 mm nozzle in transverse-vertical build direction and 0.40 mm nozzle in transverse-vertical build direction. In order to evaluate the repeatability of the FDM process, several replications were conducted. The

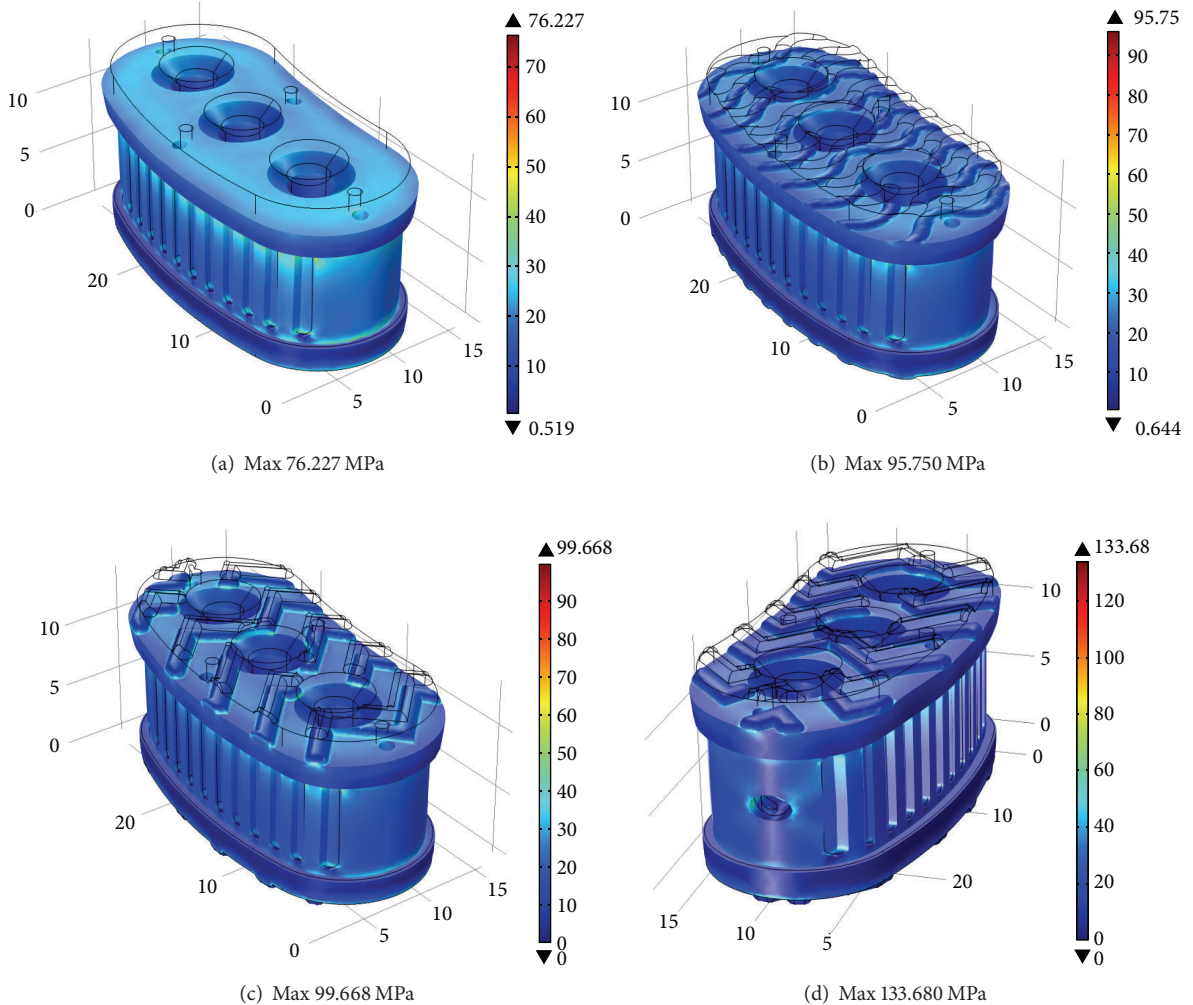


FIGURE 7: Volumetric analysis: von Mises stress distribution with 4,000 N as reference load.

average of these loads was of 7,776 N and the standard deviation was of 102.3 N. Therefore, the process has a deviation error of 1.32% between the five experimental trials, a number that indicates a good repeatability of the process.

Table 3 shows the mechanical properties of PC-ISO cylindrical test specimens obtained from the initial mechanical compressive testing, in order to be used as preliminary data for the Finite Element Analysis. Compressive yield strength was calculated by dividing the load carried by the specimen at the yield point by the original minimum cross-sectional area of the specimen ( $126.7 \text{ mm}^2$ ). Figure 6 shows the comparison of the compression test of PC-ISO cylindrical test specimens of both 0.30 mm and 0.40 mm nozzle configurations.

**5.2. Simulation Results for Lumbar Cage Concepts.** Simulations results are explained in terms of the average von Mises stresses exhibited in different cross sections of the four design concepts. Figure 7 shows the Finite Element Analysis of prototypes manufactured with the 0.40 mm nozzle in a full isometric view, with a top cross-sectional area of  $257 \text{ mm}^2$ . Using the 4,000 N force as reference load, it is shown that the average von Mises stresses are up to 30 MPa for all prototypes.

Complex geometry shows higher maximum von Mises stress. Figure 8 shows the middle cross section with an area of  $268 \text{ mm}^2$  for concepts (a), (b), and (c). Concept (d) has a middle cross section area of  $262 \text{ mm}^2$ . As expected, all design concepts exhibited average von Mises stress of approximately 15 MPa. Stress increases in the outer regions of the cross section due to the complex geometry of the outside surface of the implant. In the case of concept (d), the maximum stress is higher compared to the other concepts due to the stress concentration effect of the handling hole.

Figure 9 shows the cross section of the top plane where the volumetric analysis (from Figure 7) shows the maximum von Mises stress. In this plane, the cross-sectional area is  $247 \text{ mm}^2$  due to the blind holes incorporated in the design concept. Average von Mises stress should be 16.2 MPa. Stress concentration regions produce localized values up to 78.8 MPa.

**5.3. Experimental Results for Lumbar Cage Concepts.** Figure 10 shows a comparison between compressive strength tests of the proposed lumbar cage design (a) manufactured by the 0.30 mm nozzle and 0.40 mm nozzle. It is clearly

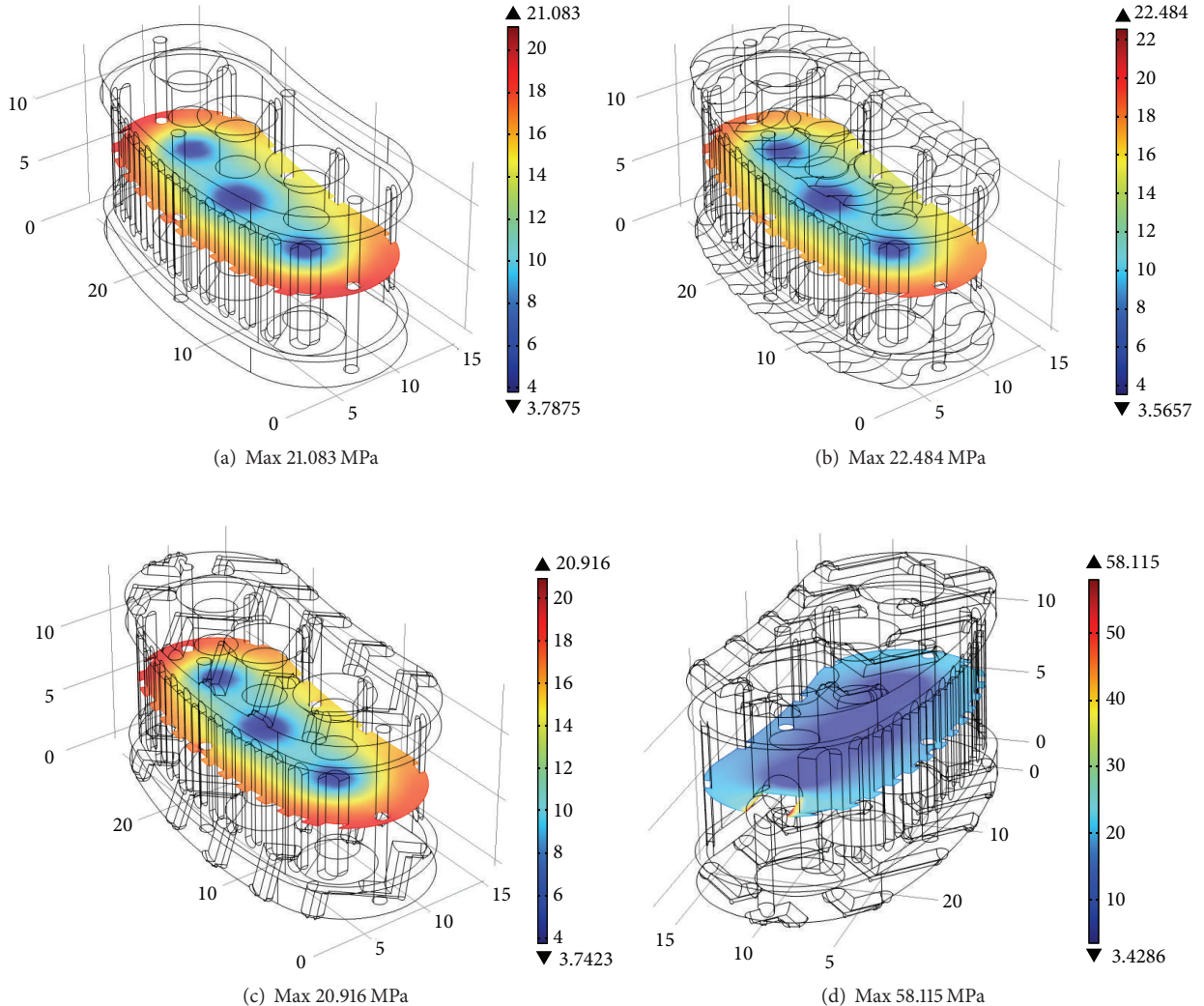


FIGURE 8: Cross section analysis for middle plane: von Mises stress distribution with 4,000 N as reference load.

seen from the same figure that the lumbar cage design manufactured by the 0.40 mm nozzle has better mechanical properties than those manufactured by the 0.30 mm nozzle. Further experimentation was limited to the 0.40 mm nozzle configuration.

Figure 11 shows the measured load ( $L$ ) versus displacement ( $d$ ) behavior of prototypes manufactured with the 0.40 mm nozzle. The best mechanical behavior is found in those design concepts with simpler geometrical elements, such as design (a) with the flat surface and design (b) with undulating features. However, the design concepts with more complex geometry (such as (c) and (d)) facilitate osseointegration and the surgical procedure during implantation.

**5.4. Discussion.** Based on the cylindrical samples, the reference compressive yield strength to consider is 55 MPa. The middle plane simulation analysis shows that, on average, stress level is well below the compressive yield strength of the FDM-printed PC-ISO material. Only in the case of concept (d), the maximum stress level exceeds the limit by small percentage (6%).

From the compression testing experimental results of the cylindrical specimens and the design concepts (Figures 6 and 10), the mechanical behavior exhibited at 1 mm of displacement is similar in terms of engineering stress. Specifically, the cylindrical specimens exhibited an approximate engineering stress of 54 MPa (estimated with a cross section of 126 mm<sup>2</sup> and 6800 N) while the engineering stress at the middle cross section (estimated with 268 mm<sup>2</sup> and 15,000 N) of the design concepts is approximately 55 MPa.

Local maximum stress levels are above the material strength in some regions. For the top plane analysis, all regions with maximum stress are above the material strength (between 14 and 43% higher stress compared to the material strength). The volumetric analysis shows regions that exceed the material strength by a large percentage (up to 143% in the case of design concept (d)).

In contrast to the FEM analysis results, using 4,000 N as the reference load, the actual compression test shows that the various design concepts are robust. For the case of design concepts (a) and (b), the yield behavior starts at approximately

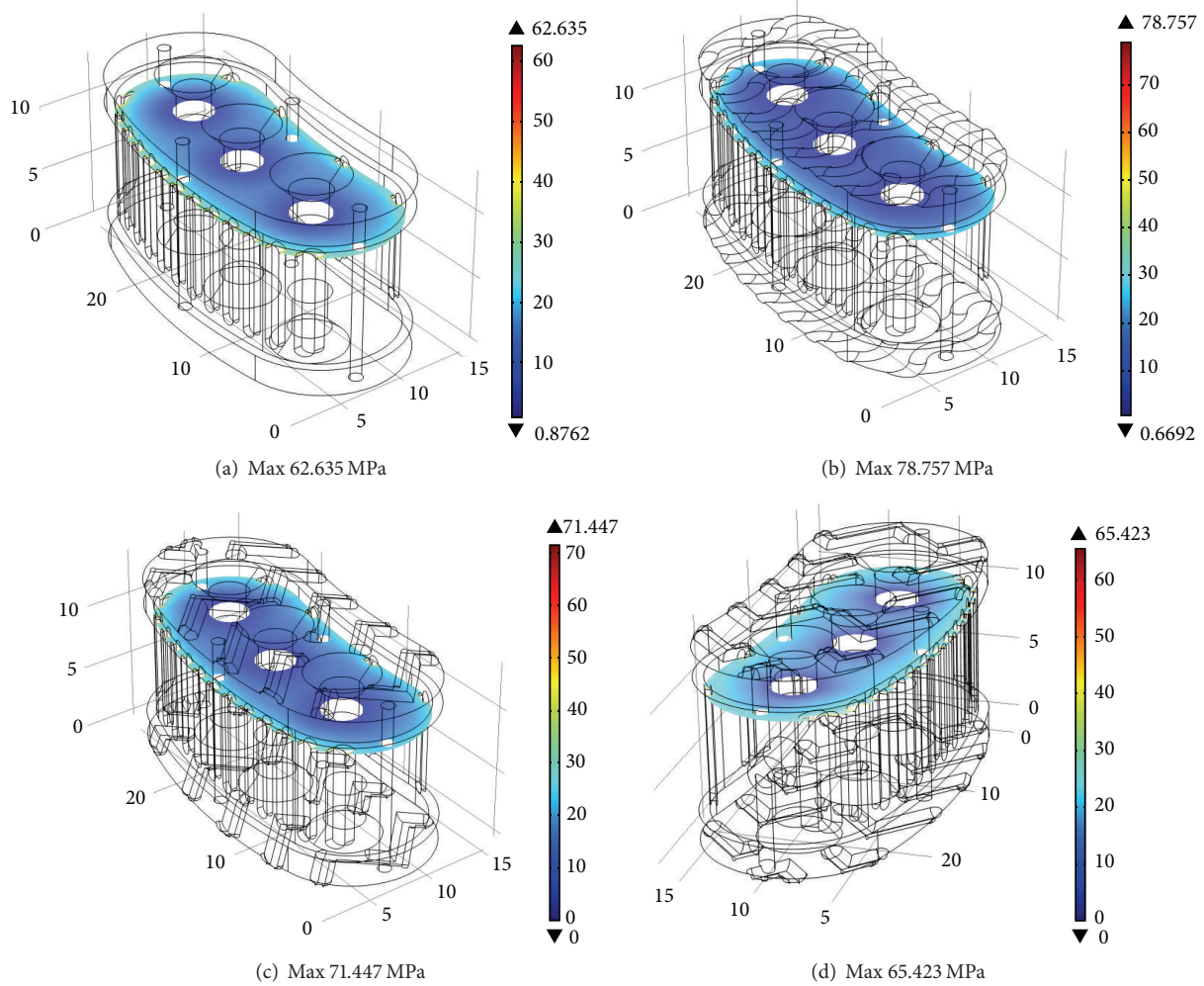


FIGURE 9: Cross section analysis for top plane: von Mises stress distribution with 4,000 N as reference load.

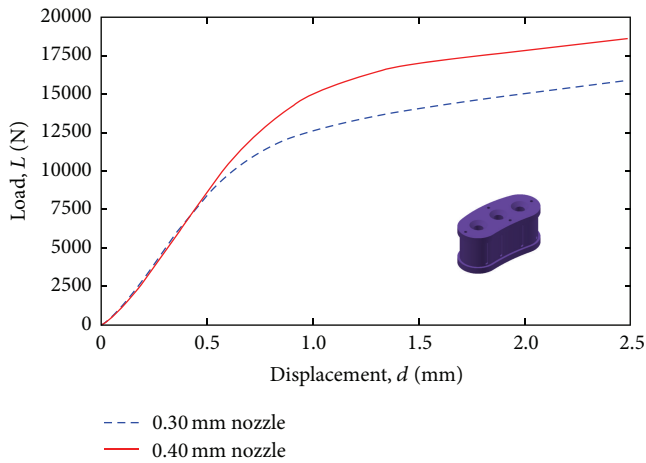


FIGURE 10: Compression testing for design concept (a), with different FDM nozzle configurations (0.30 versus 0.40 mm).

10,000 N. A load of approximately 7,500 N is supported by design concepts (c) and (d) before yielding is observed.

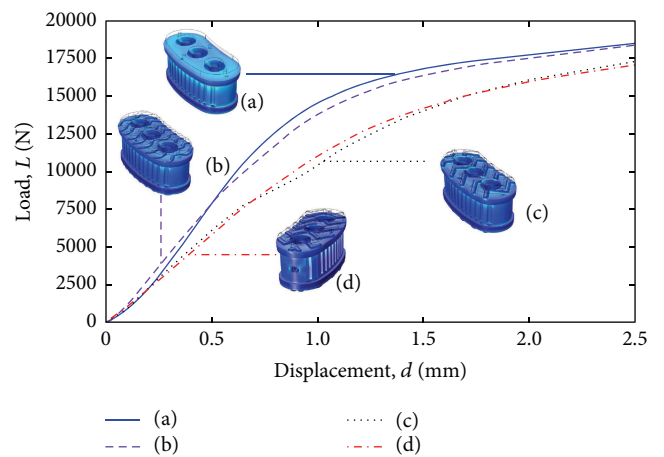


FIGURE 11: Compression testing for all design concepts with 0.40 mm nozzle configuration.

The FDM process cannot produce sharp corners due to geometry of the filament used for generation of each layer.

Therefore, this additive manufacturing process is beneficial to avoid stress concentration regions in the printed intervertebral lumbar cages. In addition, the FEM analysis shows that the stress concentration areas are quite localized. Therefore, it can be concluded that the high loads supported by the different design concepts are due to a combination of (a) localized stress concentration regions, (b) additive manufacturing process that intrinsically reduces stress concentration geometries, and (c) ductile nature of the PC-ISO material.

In order to further validate the proposed design concepts, additional testing under dynamic conditions is needed in order to assess the fatigue response of the material. In terms of the design concepts, additional refinements are required in order to reduce the amount of stress concentration due to sharp changes in geometry.

## 6. Conclusions and Future Work

This work has shown the viability of FDM-printed intervertebral lumbar cages based on biocompatible polycarbonate (PC-ISO material). Several design concepts are proposed for the generation of patient-specific intervertebral lumbar cages. Finite Element Analysis and compression testing show the viability of the proposed design concepts. The part interior style has a more significant influence than the build direction of the material deposition. Furthermore, PC-ISO material showed a high repeatability in the manufacture process for transverse-vertical build direction and solid part interior style parameters, achieving compressive yield strength of 55 MPa. The literature recommends a reference load of 4,000 N for design of intervertebral lumbar cages. Under compression testing conditions, the FDM-printed intervertebral lumbar cages withstand between 7,500 and 10,000 N of load before showing yielding.

Further research must be carried out with in vitro and in vivo testing in order to guarantee the full viability of the intervertebral lumbar cage implants that have been proposed in this work. Specifically, the validation should be carried out through the analysis of biocompatibility and osseointegration with the surrounding tissue, towards the full integration of 3D printed implants in the medical practice. The benefits of using 3D printing for each specific patient should potentially increase the ergonomics, simplify the procedure, and bring overall better personalized results once validated.

## Competing Interests

The authors declare that there are no competing interests regarding the publication of this paper.

## Acknowledgments

The authors would like to acknowledge the support of Tecnológico de Monterrey through its Research Group in Advanced Manufacturing. Support was also provided from the MADI<sup>T</sup> “National Lab of Additive Manufacturing, 3D Digitizing and Computerized Tomography” at Universidad Nacional Autónoma de México and from Centro de Tecnología da Informação Renato Archer. Finally, the authors of this

work would like to express their gratitude to Jan Lammel Lindemann, for his valuable comments.

## References

- [1] G. Gao and X. Cui, “Three-dimensional bioprinting in tissue engineering and regenerative medicine,” *Biotechnology Letters*, vol. 38, no. 2, pp. 203–211, 2016.
- [2] D. Radenkovic, A. Solouk, and A. Seifalian, “Personalized development of human organs using 3D printing technology,” *Medical Hypotheses*, vol. 87, pp. 30–33, 2016.
- [3] S.-S. Yoo, “3D-printed biological organs: medical potential and patenting opportunity,” *Expert Opinion on Therapeutic Patents*, vol. 25, no. 5, pp. 507–511, 2015.
- [4] J. Visser, F. P. Melchels, W. J. Dhert, and J. Malda, “Tissue printing; the potential application of 3D printing in medicine,” *Nederlands Tijdschrift voor Geneeskunde*, vol. 157, no. 52, Article ID A7043, 2013.
- [5] V. Petrovic, J. V. Haro Gonzalez, O. Jordá Ferrando, J. Delgado Gordillo, J. R. Blasco Puchades, and L. Portoles Grinan, “Additive layered manufacturing: sectors of industrial application shown through case studies,” *International Journal of Production Research*, vol. 49, no. 4, pp. 1061–1079, 2011.
- [6] T. M. Rankin, N. A. Giovinco, D. J. Cucher, G. Watts, B. Hurwitz, and D. G. Armstrong, “Three-dimensional printing surgical instruments: are we there yet?” *Journal of Surgical Research*, vol. 189, no. 2, pp. 193–197, 2014.
- [7] N. de Beer and A. van der Merwe, “Patient-specific intervertebral disc implants using rapid manufacturing technology,” *Rapid Prototyping Journal*, vol. 19, no. 2, pp. 126–139, 2013.
- [8] J. Domanski, K. Skalski, R. Grygoruk, and A. Mróz, “Rapid prototyping in the intervertebral implant design process,” *Rapid Prototyping Journal*, vol. 21, no. 6, pp. 735–746, 2015.
- [9] D. Espalin, K. Arcaute, D. Rodriguez, F. Medina, M. Posner, and R. Wicker, “Fused deposition modeling of patient-specific polymethylmethacrylate implants,” *Rapid Prototyping Journal*, vol. 16, no. 3, pp. 164–173, 2010.
- [10] V. N. Chougule, A. V. Mulay, and B. B. Ahuja, “Development of patient specific implants for minimum invasive spine surgeries (MISS) from non-invasive imaging techniques by reverse engineering and additive manufacturing techniques,” *Procedia Engineering*, vol. 97, pp. 212–219, 2014.
- [11] O. Figueroa, C. A. Rodríguez, H. R. Siller et al., “Lumbar cage design concepts based on additive manufacturing,” in *High Value Manufacturing: Advanced Research in Virtual and Rapid Prototyping*, P. H. da Silva Bárto, A. C. S. de Lemos, A. M. H. Pereira et al., Eds., chapter 102, CRC Press, New York, NY, USA, 2013.
- [12] M. Perez, M. Block, D. Espalin et al., “Sterilization of FDM-manufactured parts,” in *Proceedings of the 23rd Annual International Solid Freeform Fabrication Symposium (SFF '12)*, pp. 285–296, Austin, Tex, USA, August 2012.
- [13] J. Cunha, R. Sethi, K. Mellis et al., “WE-F-16A-01: commissioning and clinical use of PC-ISO for customized, 3D printed, gynecological brachytherapy applicators,” *Medical Physics*, vol. 41, no. 6, article 514, 2014.
- [14] S.-H. Ahn, M. Montero, D. Odell, S. Roundy, and P. K. Wright, “Anisotropic material properties of fused deposition modeling ABS,” *Rapid Prototyping Journal*, vol. 8, no. 4, pp. 248–257, 2002.
- [15] Stratasys, *Production-Grade Thermoplastic for Fortus 3D Production Systems*, Stratasys, Eden Prairie, Minn, USA, 2015.

- [16] B. Schafer and H. Halm, "Intervertebral implant," United States of America Patent US 6,143,032, 2000.
- [17] S. A. Webb, A. P. Moreno, M. E. Mitchell, and A. C. Smith, "Spinal implant," United States of America Patent US 7,806,932 B2, 2010.
- [18] P. P. Varga and J. W. Ogilvie, "Intervertebral spacer," United States of America Patent US 6,579,318 B2, 2003.
- [19] F. K. Fuss and R. J. Sabitzer, "Implant for insertion between spinal column vertebrae," United States of America Patent US 6,562,072 B1, 2003.
- [20] M. A. Adams and P. Dolan, "Spine biomechanics," *Journal of Biomechanics*, vol. 38, no. 10, pp. 1972–1983, 2005.
- [21] J. Lee and A. Huang, "Fatigue analysis of FDM materials," *Rapid Prototyping Journal*, vol. 19, no. 4, pp. 291–299, 2013.
- [22] ASTM D695-10, *Standard Test Method for Compressive Properties of Rigid Plastics*, ASTM International, West Conshohocken, Pa, USA, 2010, <https://www.astm.org/>.
- [23] H.-J. Wilke, P. Neef, B. Hinz, H. Seidel, and L. Claes, "Intradiscal pressure together with anthropometric data—a data set for the validation of models," *Clinical Biomechanics*, vol. 16, supplement 1, pp. S111–S126, 2001.
- [24] A. Schultz, G. Andersson, R. Ortengren, K. Haderspeck, and A. Nachemson, "Loads on the lumbar spine. Validation of a biomechanical analysis by measurements of intradiscal pressures and myoelectric signals," *The Journal of Bone & Joint Surgery—American Volume*, vol. 64, no. 5, pp. 713–720, 1982.

## Research Article

# A New Orthodontic Appliance with a Mini Screw for Upper Molar Distalization

Nurhat Ozkalayci<sup>1</sup> and Mehmet Yetmez<sup>2</sup>

<sup>1</sup>Department of Orthodontics, Faculty of Dentistry, Bulet Ecevit University, 67100 Zonguldak, Turkey

<sup>2</sup>Department of Mechanical Engineering, Faculty of Engineering, Bulet Ecevit University, 67100 Zonguldak, Turkey

Correspondence should be addressed to Nurhat Ozkalayci; dt.nurhat@yahoo.com

Received 29 April 2016; Accepted 30 June 2016

Academic Editor: Alberto Borboni

Copyright © 2016 N. Ozkalayci and M. Yetmez. This is an open access article distributed under the Creative Commons Attribution License, which permits unrestricted use, distribution, and reproduction in any medium, provided the original work is properly cited.

The aim of this study is to present a new upper molar distalization appliance called Cise distalizer designed as intraoral device supported with orthodontic mini screw for upper permanent molar distalization. The new appliance consists of eight main components. In order to understand the optimum force level, the appliance under static loading is tested by using strain gage measurement techniques. Results show that one of the open coils produces approximately 300 gr distalization force. Cise distalizer can provide totally 600 gr distalization force. This range of force level is enough for distalization of upper first and second molar teeth.

## 1. Introduction

Orthodontic problems can be classified as skeletal problems and dental problems. Skeletal problems can be originated from skeletal deviations and treated with orthopedic corrections, fixed mechanics, or surgery. Dental problems are classified as dental class I malocclusion, dental class II malocclusion, and dental class III malocclusion. Dental class II malocclusion is generally caused by the early loss of the upper deciduous second molar. After early tooth loss, upper first permanent molars erupt more mesially than their normal locations or drift mesially [1–3]. On one hand, upper first premolars' extraction followed by fixed orthodontic treatment is mostly chosen treatment way of this type of dental malocclusion. On the other hand, upper molar distalization can be used as alternative treatment way [4–6]. This type of molar tooth movement can be achieved by extraoral or intraoral orthodontic appliances [7, 8]. The main disadvantages of extraoral appliances are aesthetic appearance and need of patient cooperation [9, 10]. In order to eliminate such need, intraoral appliances are designed for usage [1–3]. The class II elastics or intermaxillary anchorage is one of the ways that correct the class II dental relationships but the lower incisor protrusion and the bite deepening are the most probably seen

side effects of this elastic usage. Removable appliances can be also used for the upper molar distalization but it is difficult to provide enough anchorage with removable appliances due to their retention limits, whereas the upper incisor protrusion is the possible disadvantage of these mechanics. Another disadvantage of these devices is the fact that their success is directly dependent on the patient's compliance like headgears. Only fixed mechanics with coils do not achieve proper molar distalization. Another common way for upper molar distalization is the extraction of the second molar or distalizing the upper molar before the second molar eruption [11]. However, loss of the upper second molar is a cold idea for patients and clinician in general clinical practice. In addition to that, the anchorage need is one of the main problems for intraoral appliances [12]. Intraoral appliances can be supported by teeth or/and soft tissue [13]. However, side effects like soft tissue irritation and unwanted tooth movement can be seen due to teeth and soft tissue anchorage [14]. Recently, to avoid these side effects, the most popular way of the intraoral anchorage is the use of orthodontic mini screw [15]. New appliances which supported orthodontic mini screw, teeth, or soft tissue are designed and presented on last decade for upper molar distalization [16]. Most of these appliances can be placed on palatal soft tissue and

orthodontic mini screws are placed in palatine bone. These two-side effective appliances can be mainly considered for only first molar distalization [17].

In this study, a new appliance called Cise distalizer supported with only orthodontic mini screw for upper molar distalization is designed, produced, and tested. Cise distalizer is placed into the buccal maxillary area and can be used on one-side or two-side upper first and second molar distalization.

## 2. Materials and Methods

The appliance called Cise distalizer consists of eight main components (see Figure 1), namely, (i) a mini screw (Dentaurum, Germany), (ii) a rectangular bendable L-wire (Dentaurum, Germany), (iii) a crimpable bendable wire (Dentaurum, Germany), (iv) NiTi open coil spring (Modern Orthodontics, India), (v) two screwed stoppers (Dentaurum, Germany), (vi) two T-tubes (Dentaurum, Germany), (vii) a molar tube (Dentaurum, Germany), and (viii) lingual retainer composite with its bonding agent (3M Unitek, USA).

Three design steps of the appliance are as follows:

- The main structure is completed by integrating the screwed stopper to the rectangular long L-wire and the crimpable bendable wire. In this step, crimpable wire is crimped to the small arm of L-wire with crimping hook plier.
- The open coil springs are fixed to one end of each wire. That is, the two stoppers are placed to the L-wire and the crimpable wire, respectively. Similarly, the two open coils are located to the L-wire and the crimpable wire, respectively.
- The structure ends up adding T-tubes and a molar tube to the wires. Briefly, it means that after molar tube is bonded on the upper first molar, two T-tubes are inserted on L-wire. Then, the L-wire is transformed into U-wire. Finally, the appliance is bonded to the head of mini screw. The appliance without activation is given in Figure 2.

Shortly, the appliance has four active and two passive parts. Active parts are two open coils and two screw activated stoppers. Passive parts are two rectangular wire ends, one of which attaches to orthodontic mini screw and the other one is placed into molar tube. Orthodontic mini screw can be inserted either between upper canine and first premolar region (right side) or between upper first premolar and second premolar region (left side). These two different mini screw cases are presented in Figure 3. It is noted that the region can be chosen according to characteristics of patient's dental arches.

For strain gage measurement, two unidirectional GFLA-3-350-50 strain gages (gage factor:  $2.12 \pm 0.01$ ; gage resistance:  $350 \pm 1\Omega$ ) are used with an adhesive, namely, P-2 (TML, Tokyo Sokki Kenkyujo Co., Ltd., Japan). Figure 3 shows location of the mounted strain gages on the critical points of the model. The critical point is the location of distal surface of upper first permanent molar teeth. When the appliance is

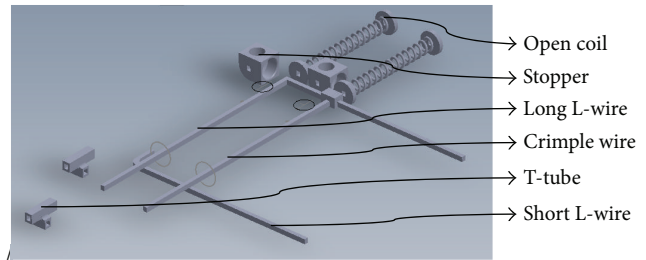


FIGURE 1: Components of Cise distalizer.

activated with the sliding of two stoppers, strain gage measurement is obtained. The two-channel strain measurements are completed using a microprocessor-based data acquisition system, namely, SoMat™ eDAQlite, and SoMat TCE software (HBM, Inc., USA).

## 3. Results and Discussions

Results of the strain measurement are given in Figure 4. The results obviously show that one of the open coils produces approximately 300 gr distalization force. Cise distalizer can provide totally 600 gr distalization force. This range of force level is acceptable for distalization of upper first and second molar teeth to eliminate unwanted tooth movement. In other words, it is possible to provide optimum force level while using Cise distalizer.

One can also say that (1) loading of appliance provides acceptable deflection distal surface of upper first molar and (2) strain field at mini screw with upper first premolar and second premolar region (left side) is higher than that at mini screw with upper canine and first premolar region. In other words, the design at left side reflects more deflection than that of the other side.

Corresponding to the advantages of the Cise distalizer for clinical applications, one may discuss three main points. First, dental malocclusion caused by dental crowding shows different molar relationships. If the mandibular arch crowding is mild and the molar relationship is class II and the sagittal, transversal, and vertical skeletal relationships between the maxillary and mandibular bones are normal, most possible cause of the severe upper arch crowding is the mesial movements of upper molars [18]. According to the acceptable force versus movement control, Cise distalizer can provide molar distalization without poor aesthetics because anchorage control can be completed by orthodontic mini screws which are more esthetic than extraoral appliances and activation of appliance is done by clinician and there is no need for patient's cooperation. Only monthly activation of Cise distalizer is suitable for providing force of optimum molar distalization. Force level of Cise distalizer can be controlled easily with the activation degree of stoppers. This force control is very important for elimination of unwanted tooth movement of high force level. It is possible to provide optimum force level while using Cise distalizer.

Second, most of the distalization appliances are placed on the palatine region with orthodontic mini screws [11, 19–21]. This type of appliances possesses hygiene problem due to



FIGURE 2: Cise distalizer on model without activation.

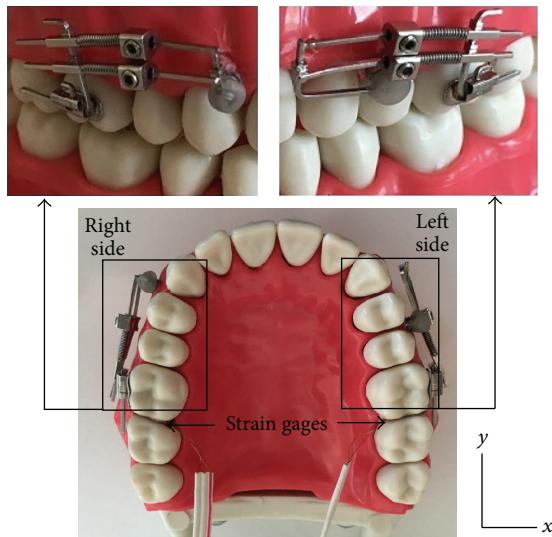


FIGURE 3: Cise distalizer and mounted strain gages on the model.

the fact that it is difficult to provide adequate plaque control under appliances. Also, there are high risks of aspiration, swallowing of piece of the appliance, and damage of the orthodontic mini screw due to trauma. In order to decrease the risk(s), Cise distalizer with its orthodontic mini screw is placed on the buccal region of maxilla [22].

Third, many distalization appliances are designed for two-side molar movement or at least need both right and left first molar attachment with welding molar bands [23, 24]. Cise distalizer can be placed on one side and molar attachment can be made with molar tube and can be produced by clinician at clinic and there is no need for study model, a technician, and a laboratory work. So Cise distalizer is more economic and useful appliance than others. Consequently, Cise distalizer is more hygienic and ergonomic than other appliances and can be easily used on one side. Anchorage of Cise distalizer is provided by an orthodontic mini screw infinite anchorage unit. This type of anchorage eliminates side effects like soft tissue irritation and unwanted tooth movement such as anterior teeth protrusion or mesial movement of premolar [3, 25]. In addition to that, mini screw can be placed in different

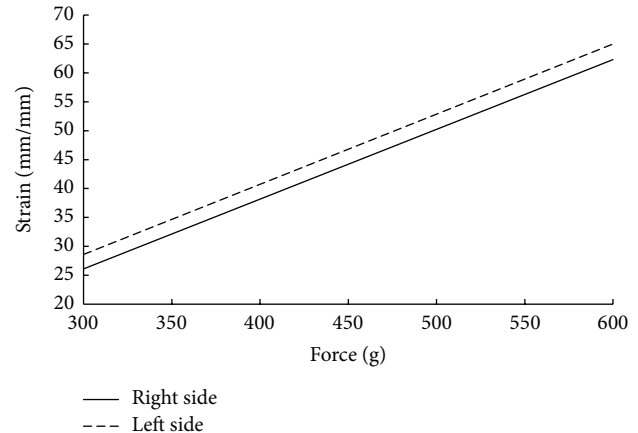


FIGURE 4: Comparison of Cise distalizer at right side and at left side under various loading.

proper area like being placed distal to canine or distal to first premolar.

#### 4. Conclusion

Cise distalizer is an economic and ergonomic distalization appliance. The new appliance introduced here can be used in clinical applications and orthodontic treatments to provide adequate and enough distalization force for upper first and second molar. In the near future, clinical results are to be carefully evaluated to improve the appliance.

#### Competing Interests

The authors declare that they have no competing interests.

#### References

- [1] A. Prakash, R. Patil, O. P. Mehta, G. Singh, and P. K. Jayaprakash, "Post distalization—anchoring molars," *Indian Journal of Dental Sciences*, vol. 5, pp. 120–121, 2013.
- [2] G. Yordanova, "Pendulum appliance—clinics and results," *International Journal of Science and Research*, vol. 3, pp. 1647–1649, 2014.
- [3] C. L. Sandifer, J. D. English, C. D. Colville, R. L. Gallerano, and S. Akyalcin, "Treatment effects of the Carrière distalizer

- using lingual arch and full fixed appliances,” *Journal of the World Federation of Orthodontists*, vol. 3, no. 2, pp. e49–e54, 2014.
- [4] T. T. Üçem, S. Yüksel, C. Okay, and A. Gülsen, “Effects of a three-dimensional bimetric maxillary distalizing arch,” *The European Journal of Orthodontics*, vol. 22, no. 3, pp. 293–298, 2000.
  - [5] D. R. Burkhardt, J. A. McNamara Jr., and T. Baccetti, “Maxillary molar distalization or mandibular enhancement: a cephalometric comparison of comprehensive orthodontic treatment including the pendulum and the Herbst appliances,” *American Journal of Orthodontics and Dentofacial Orthopedics*, vol. 123, no. 2, pp. 108–116, 2003.
  - [6] G. Oberti, C. Villegas, M. Ealo, J. C. Palacio, and T. Baccetti, “Maxillary molar distalization with the dual-force distalizer supported by mini-implants: a clinical study,” *American Journal of Orthodontics and Dentofacial Orthopedics*, vol. 135, no. 3, pp. 282.e1–282.e5, 2009.
  - [7] H. Wang, J. Feng, P. Lu, and G. Shen, “Correction of a skeletal Class II malocclusion with severe crowding by a specially designed rapid maxillary expander,” *American Journal of Orthodontics and Dentofacial Orthopedics*, vol. 147, no. 2, pp. 242–251, 2015.
  - [8] A. D. L. S. D. Lira, A. Izquierdo, S. prado, M. Nojima, and L. Maia, “Anteroposterior dentoalveolar effects with cervical headgear and pendulum appliance: a systematic review,” *Brazilian Journal of Oral Sciences*, vol. 11, no. 4, pp. 433–439, 2012.
  - [9] E. Bolla, F. Muratore, A. Carano, and S. J. Bowman, “Evaluation of maxillary molar distalization with the distal jet: a comparison with other contemporary methods,” *The Angle Orthodontist*, vol. 72, no. 5, pp. 481–494, 2002.
  - [10] G. S. M. Kinzinger and P. R. Diedrich, “Biomechanics of a distal jet appliance: theoretical considerations and in vitro analysis of force systems,” *The Angle Orthodontist*, vol. 78, no. 4, pp. 676–681, 2008.
  - [11] G. S. Antonarakis and S. Kiliaridis, “Maxillary molar distalization with noncompliance intramaxillary appliances in class II malocclusion: a systematic review,” *Angle Orthodontist*, vol. 78, no. 6, pp. 1133–1140, 2008.
  - [12] K.-R. Chung, S.-H. Kim, M. P. Chaffee, and G. Nelson, “Molar distalization with a partially integrated mini-implant to correct unilateral Class II malocclusion,” *American Journal of Orthodontics and Dentofacial Orthopedics*, vol. 138, no. 6, pp. 810–819, 2010.
  - [13] A. Caprioglio, M. Cozzani, and M. Fontana, “Comparative evaluation of molar distalization therapy with erupted second molar: segmented versus Quad Pendulum appliance,” *Progress in Orthodontics*, vol. 15, no. 1, article 49, 2014.
  - [14] A. Sodagar, M. A. Akhoundi, A. Rafighii, and S. Arab, “Fabrication and evaluation of a noncompliant molar distalizing appliance: bonded molar distalizer,” *Journal of Dentistry*, vol. 8, no. 3, pp. 107–116, 2011.
  - [15] J. Hourfar, B. Ludwig, and G. Kanavakis, “An active, skeletally anchored transpalatal appliance for derotation, distalization and vertical control of maxillary first molars,” *Journal of Orthodontics*, vol. 41, supplement 1, pp. S24–S32, 2014.
  - [16] A. S. Burhan, “Combined treatment with headgear and the frog appliance for maxillary molar distalization: a randomized controlled trial,” *Korean Journal of Orthodontics*, vol. 43, no. 2, pp. 101–109, 2013.
  - [17] P. Chandra, S. Agarwal, and D. Singh, “Intra oral molar distalization—a review,” *Journal of Dentofacial Sciences*, vol. 1, no. 1, pp. 15–18, 2012.
  - [18] W. Al-Faleh, “Intraoral maxillary molar distalization: a review,” *Pakistan Oral and Dental Journal*, vol. 29, pp. 301–310, 2009.
  - [19] A. Goyal, H. Jyothikiran, V. Patel, and B. Shivalinga, “Mini-implant supported molar distalization,” *Journal of Dental Implants*, vol. 2, no. 2, pp. 136–140, 2012.
  - [20] A. Caprioglio, M. Fontana, E. Longoni, and M. Cozzani, “Long-term evaluation of the molar movements following Pendulum and fixed appliances,” *The Angle Orthodontist*, vol. 83, no. 3, pp. 447–454, 2013.
  - [21] B. Wilmes, V. Katyal, and D. Drescher, “Mini-implant-borne Pendulum B appliance for maxillary molar distalisation: design and clinical procedure,” *Australian Orthodontic Journal*, vol. 30, no. 2, pp. 230–239, 2014.
  - [22] T. E. Bechtold, J.-W. Kim, T.-H. Choi, Y.-C. Park, and K.-J. Lee, “Distalization pattern of the maxillary arch depending on the number of orthodontic miniscrews,” *The Angle Orthodontist*, vol. 83, no. 2, pp. 266–273, 2013.
  - [23] A. G. Acar, S. Gürsoy, and M. Dinçer, “Molar distalization with a pendulum appliance K-loop combination,” *The European Journal of Orthodontics*, vol. 32, no. 4, pp. 459–465, 2010.
  - [24] A. Mavropoulos, K. Sayinsu, F. Allaf, S. Kiliaridis, M. A. Papadopoulos, and A. O. Keles, “Noncompliance unilateral maxillary molar distalization: a three-dimensional tooth movement analysis,” *The Angle Orthodontist*, vol. 76, no. 3, pp. 382–387, 2006.
  - [25] M. Matei, K. Earar, I. Grigorescu, and I. Zetu, “Simplified systems of distylization—the frog appliance,” *Annals of the University Dunarea de Jos of Galati*, vol. 17, no. 1, pp. 77–80, 2014.

## Research Article

# Functional Design in Rehabilitation: Modular Mechanisms for Ankle Complex

**Francesco Aggogeri, Nicola Pellegrini, and Riccardo Adamini**

*Department of Mechanical and Industrial Engineering, University of Brescia, Via Branze 38, 25123 Brescia, Italy*

Correspondence should be addressed to Francesco Aggogeri; francesco.aggogeri@unibs.it

Received 29 April 2016; Revised 22 June 2016; Accepted 29 June 2016

Academic Editor: Tadeusz Mikołajczyk

Copyright © 2016 Francesco Aggogeri et al. This is an open access article distributed under the Creative Commons Attribution License, which permits unrestricted use, distribution, and reproduction in any medium, provided the original work is properly cited.

This paper is aimed at presenting an innovative ankle rehabilitation device based on a parallel mechanism. A functional analysis and design are described to obtain a device able to guarantee ankle movement while patient's body remains stationary. Human ankle is a challenging context where a series of joints are highly integrated. The proposed rehabilitation device permits a patient with walking defects to improve his or her gait. The research focuses on plantar-flexion-dorsiflexion movement. The robust design starts from an accurate modelling of ankle movements during walking, assessing motion data from healthy individuals and patients. The kinematics analysis and functional evaluations lead the study and development of the articulated system. In particular, results of simulations support the effectiveness of the current design. A 3D prototype is presented highlighting that the ankle motion is successfully demonstrated.

## 1. Introduction

Rehabilitation engineering is aimed at studying and integrating the human joint movements into equipment optimization in developing effective rehabilitation devices. In this way, the study of human movements [1] plays an important role in creating innovative systems able to satisfy patient requirements in physiotherapy programs. There are many challenges and opportunities to integrate applied mechanics concepts into rehabilitation improving physiotherapy effectiveness and reducing healthcare costs. A new prototype for ankle rehabilitation is presented in this study. It has been designed focusing on the integration of human joint movements with machine architecture for rehabilitation machines. Starting from the patients' requirements and an assessment of ankle motion analysis, this paper introduces the mechanism evaluation and the main technical solutions in the device development. Ankle injuries are one of the most common and serious issues in daily activities and sports (15–20% of sport injuries) [2]. Therefore, the creation of an apparatus suitable for the ankle physiotherapy requires an awareness of ankle functionalities, in particular the joint motion ones. In any robotic rehabilitation equipment changes in joint motion are

taken into account considering the structure motion and the desired increased range-of-ankle motion that can be fulfilled through the use of a device based on parallel apparatus design. A parallel mechanism has the advantages of high dynamic performance supporting the ankle motion. This paper investigates the human ankle complexity, movement, and functional needs in rehabilitation. Ankles injuries are analyzed and physiotherapy protocols are examined. The ankle movement is provided as an orientation where a range is given for ankle rehabilitation. This particular range is used for the concept of equipment based on the angle performance [3]. Further kinematics and stiffness analysis are performed on this innovative system. The research uses interdisciplinary approach, combining the clinical requirements with the parallel mechanism configuration and planning rehabilitation motion in a defined workspace for the aim of concurrent design.

In last decades, many systems have been proposed to recover ankle functionalities. These mechanisms focus on human motions without walking. State of the art presents different approaches in attempting this topic; in particular Girone et al. [4] developed a mechanism based on Stewart platform that permits an assisted ankle rehabilitation using

double-acting pneumatic cylinders, linear potentiometers, and force sensors. Yano et al. presented a leg-shaped robot of two 2-DOF manipulators equipped with footpads that guarantee movement of feet [5, 6]. Yoon et al. proposed a reconfigurable ankle rehabilitation robot to cover various rehabilitation exercise modes [7]. In particular, this study shows a device based on a parallel mechanism that generates pitch and roll motions as well as relative rotation between fore and rear platforms. Instead, Dai et al. introduced several parallel mechanisms with a central strut for ankle [8]. In this way, state of the art highlights a broad range of valid solutions; nevertheless there are still many points to be investigated to optimize the trade-off between therapy effectiveness and system automatization.

This paper wants to propose a new device that differs from the other solutions. It is based on a parallel mechanism (1 DOF) able to perform trajectories similar to patient's ankle in nominal environment conditions and permitting to patient's body to remain stationary.

## 2. Ankle Injuries Assessment and Movements

An ankle movement is covered by two separate joints. The first is the articulation among the tibia, the fibula, and the talus, called ankle joint. The second one formed by the talus and the calcaneus is the subtalar articulation [11]. In physiotherapy, the direction, the speed, and the range of joint motion can be altered by injuries to muscles and ligaments and medical treatment relies heavily on an understanding of the normal and abnormal joint functions [12]. The ankle joint is modelled as a simple hinge articulation. During gait cycle, the joint allows inversion and eversion of the foot (passive-resistive function) and it plays an active role in dorsiflexion or plantar-flexion of the foot in nominal environment conditions that represent a significant part of ankle movement. The ankle and subtalar joints have different functionalities and thus their role is critical in developing an excessive ankle ligament stresses.

The ankle joint allows the movements in all 3 body planes (sagittal, frontal, and transverse). The first plane is identified by  $x$ ,  $z$  and rotations around the  $y$ -axis; the transverse plane is given by  $x$ ,  $y$  and rotations in the  $z$ -axis; finally the frontal plane is limited by  $y$  and  $z$ . Nowadays, therapies and rehabilitation methods aiming to progress mobility have to work into specific tasks, customized and time optimized. Well-defined injuries have been tested in groups of patients. Improvements are noted in individuals who received a physiotherapy effort within 3 months in comparison to a conventional one that normally requires from 6 up to 8 months [13]. These studies confirm the potential of a target leading physical therapy.

## 3. Concurrent Model Driven by Functional Requirements

Ankle is a sensitive structural and complex system. This study proposes a robust technique able to support rehabilitation therapy in every distinct phases: assessment, training, and control. The starting point is to identify the real-time patient's

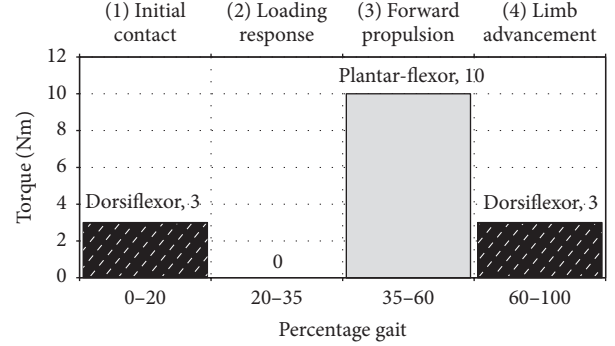


FIGURE 1: Dorsi- and plantar-flexor torque in no-defect walk.

measurements as inputs in generating a specific task. The robot software compares the planned torque or trajectory achieved during rehabilitation. Finally, the robot interface performs the possible correction through the virtual environment. The main assumption is the ability in tracing accurately the joint's center location during the gait cycle.

The developed mechanism provides many types of targeted activities in order to add benefits for autonomous operation, improve safety, manage real-time feedbacks, and reduce the therapist contribution [14]. A preliminary study of gait trajectories using a simple limb model is presented.

The objective of this paper is to develop a rehabilitation device starting from an accurate biomechanical model. Some assumptions of stiffness, stresses, and other limitations are made [15] and included in simulations for the novel iterative roadmap. The framework uses a series of rotations to determine the angle. The XYZ Euler angles convention is adopted and the orientation of the ankle is described by a rotation about  $x$ -,  $y$ -, and  $z$ -axis.

The plantar-flexion/dorsiflexion operation is expressed by  $X$  Euler angle; the inversion/eversion is illustrated by  $Y$  Euler one and the abduction/adduction is explained by  $Z$  Euler one. The controlled axis is  $x$  plantar-flexion/dorsiflexion movement; the other axes are not included. This particular order is chosen considering the clinical applications. Figure 1 indicates the assistive torque at ankle joints by the rehabilitation device in a gait cycle [16]. The needed torque varies from 3 Nm in dorsiflexion operation, while, during impulse phase, the plantar-flexor actuations achieve torques equal to 10 Nm [17].

Nowadays, all commercially rehabilitation robots are composed of joints without any power feedbacks. Passive systems have the benefit to reduce cost guaranteeing the structural simplicity [18, 19]. These devices are not able to offer assistance during third phase, where additional torque is required. In this case, the motion control is generally based on the actuators in an open loop, when the strength and effectiveness are not guaranteed.

Rehabilitation devices are aimed at recovering people with decreased motion control abilities. This biomechanical model needs additional inputs such as human measures and end effector specifications [20]. The developed iterative

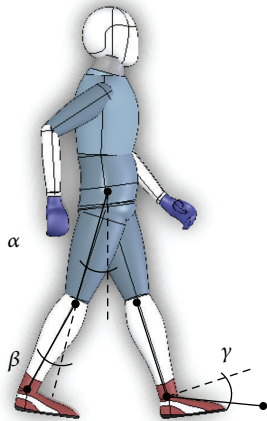


FIGURE 2: Joint angles definition.

approach to define load and trajectory requirements is represented as follows.

- (1) Determine patient's parameters with anthropometric indexes.
- (2) Estimate joint positions, velocities, accelerations, and loads.
- (3) Obtain end effector coordinates from kinematics relationships.
- (4) Joint variables are used in the limb's motion equations to acquire the end effector payloads.

Each limb can be described as a junction of three segments representing the foot (from hallux to ankle joint), leg (from ankle to knee), and thigh (from the knee to the hip). Figure 2 highlights anatomical angles of joints flexion in the sagittal plane:

- (i) hip flexion angle ( $\alpha$ ): the angle between the thigh and the perpendicular line to the ground;
- (ii) lower leg bending angle ( $\beta$ ): angle between the leg and the line through the thigh;
- (iii) foot flexion angle ( $\gamma$ ): angle between the line ankle-hallux and the perpendicular line to leg.

These angles can vary during the gait cycle; in particular they are a function of the gait cycle.

The rehabilitation system workspace needs to be suitable for a wide cluster of people as well as a different range of operation, for instance, walking or stair climbing. Angle and payload limits are used to determine the specified workspace boundary. Table 1 shows the statistical values of these variables [10].

A study on step distance and its relation with morphometric features in adult male is presented. Figure 3 underlines the height for individuals from 1,63 mm to 1,88 mm which corresponds to 1st and 99th percentile of male "20 years and over" age with "all race and ethnicity group" of American adults [10]. Other researches considering more than 200 individuals with no walking defects (group age of 20–30 years)

TABLE 1: Range of human ankle motion [10].

Movement	Max ankle angles		
	Range	Mean	Standard deviation
Dorsiflexion	20.3° to 29.8°	24.6°	3.2°
Plantar-flexion	37.6° to 45.7°	40.9°	4.3°
Inversion	14.5° to 22.0°	16.3°	3.8°
Eversion	10.0° to 17.0°	15.8°	4.4°
Internal rotation	22.0° to 36.0°	29.8°	7.5°
External rotation	15.4° to 25.9°	22.0°	5.9°

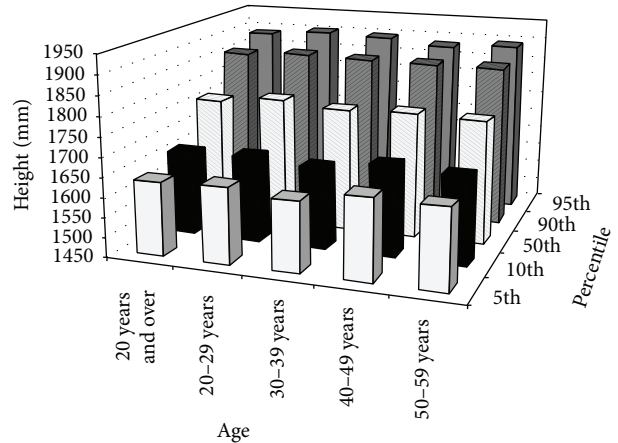


FIGURE 3: Height in millimeters for males by age and selected percentiles.

note the step distance between 600 mm and 700 mm range interval [21].

The main result of this analysis is the correlation between the step distance and the stature, investigated in many studies [22]. A set of methods are usually applied to capture accurate motion data from healthy individuals and patients [23–25]. In particular optical measurement systems, force plates, wearable sensors, accelerometers, and gyroscopes are applied to measure gait parameters, as shown in different researches [26, 27]. In this way, the user's needs are considered in designing and developing the rehabilitation devices [28]. It is possible to recap the ankle model coordinates to the step length (hereafter as  $L_p$ ). In order to study the ankle kinematics it is necessary to compare the  $x$ - and  $y$ -axis to the step length of the patient obtaining, respectively,  $A_i$  and  $B_i$  index:

$$A_i = \frac{X_i \text{ ankle}}{L_p}; \quad (1)$$

$$B_i = \frac{Y_i \text{ ankle}}{L_p}.$$

In the following equation the kinematics of any patient of known stature is determined as follows:

$$X_i \text{ ankle} = A_i \cdot L_p; \quad (2)$$

$$Y_i \text{ ankle} = B_i \cdot L_p.$$

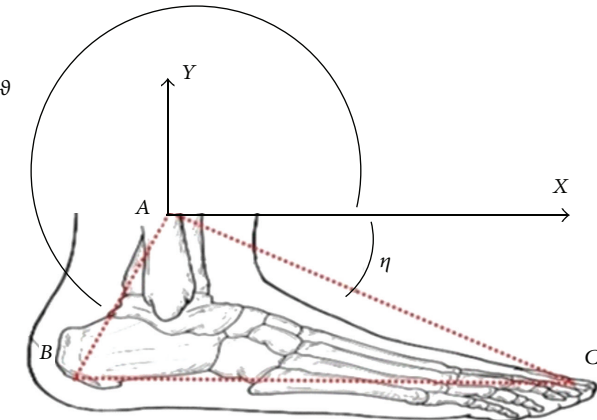


FIGURE 4: Kinematic model angles:  $\eta$  from the ground parallel to hallux and  $\theta$  from ground parallel to heel [9].

In order to define this trajectory it is necessary to assume the foot as a triangle with vertices at the hallux, ankle, and heel (Figure 4). Then it is needed to define the two angles:

- (i)  $\eta$ : the angle from the ground parallel to the ankle and hallux,
- (ii)  $\theta$ : the angle from the ground parallel to the ankle and heel.

It is possible to estimate the angle by considered instance of time, knowing the coordinates of the vertices of the foot by

$$\begin{aligned} \eta &= \arctan \frac{Y_i \text{ hallux} - Y_i \text{ ankle}}{X_i \text{ hallux} - X_i \text{ ankle}}; \\ \theta &= \pi + \arctan \frac{Y_i \text{ heel} - Y_i \text{ ankle}}{X_i \text{ heel} - X_i \text{ ankle}}. \end{aligned} \quad (3)$$

The assumption for walk trajectory planning is based on  $\eta$  and  $\theta$  angles as independent of patients and step distance. In fact, it is sufficient to know the distance of ankle-hallux (CA) and ankle-heel (AB) of a patient in order to determine the standard kinematics of the step:

$$\begin{aligned} \text{Hallux } (X, Y) &= [X_{\text{ankle}} + CA \cdot \cos(\eta); Y_{\text{ankle}} + CA \cdot \sin(\eta)]; \\ \text{Heel } (X, Y) &= [X_{\text{ankle}} + AB \cdot \cos(\eta); Y_{\text{ankle}} + AB \cdot \sin(\eta)]. \end{aligned} \quad (4)$$

The model obtained represents the typical walk of a healthy subject. This is the starting point for a preliminary trajectory definition that will be customized in order to identify ad hoc tasks and training.

In this paper the purpose is to analyze the kinematics of the ankle on the plantar-flexion movement and to increase the degree of patients' mobility. A cyclic trajectory comparing the kinematics of the ankle needs to be defined with a particular articulated mechanism, referring to a person with no walking defects.

The oscillatory phase of the gait cycle is the ankle kinematics, while the support phase is replaced and approximated by a constant motion of the ankle through the initial position

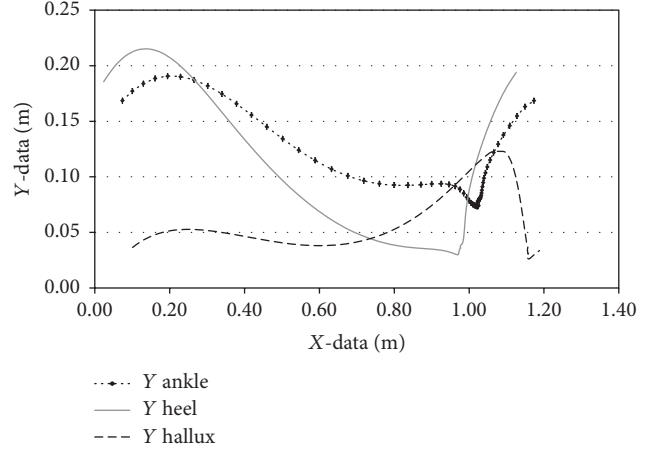


FIGURE 5: Spatial trajectory in transverse plane during gait cycle.

of the cycle. Figures 5 and 6 describe the trajectory and the velocity of the ankle, heel, and hallux model considered during the step cycle in the related Cartesian plan.

#### 4. Modular Mechanism Concept and Simulation

The know-how of the mechanism kinematics and loading performance are necessary inputs to identify the architecture. An iterative process is proposed in order to find the most advantageous mechanism design configuration.

The aim of the paper is to obtain a smart architecture of the mechanism (1 degree of freedom) able to perform trajectories similar to patient's ankle. The software used for the simulation of the planar apparatus is MECAD sw. This configuration allows the usage of one motor performing the movement of the articulated system. The mechanical equipment is constituted by 2 rods and 3 constraints; see Figure 7. Degrees of freedom for planar linkages joined with common joints can be calculated through Gruebler's equation [29]:

$$\text{DOF} = 3 \cdot (n - 1) - 2 \cdot j_p - j_h = 6 - 5 = 1, \quad (5)$$

where  $n$  is the overall sum of links in the mechanism,  $j_p$  is the total number of primary joints, and  $j_h$  is the amount of higher-order joints.

Figure 8 shows an overview of the articulated mechanism where link 5-6 is the crank shaft while link 3-5 is the piston rod. The main system parameters considered in the final simulation are listed in Table 2. A set of assumptions and constraints has been identified in defining the device design and parameters. For example, the rehabilitation walking step cannot exceed 555 mm in order to guarantee patient's safety and therapy effectiveness, as extrapolated from gait analysis.

The use of MECAD permits comparing different configurations with perturbed parameters [30–33]. The simulation output is shown in Figure 9. The proposed physical prototype of a novel modular ankle rehabilitation system is presented in

TABLE 2: Parameters of the articulated system.

Walking step [mm]	Link 5-6 [mm]	Link 3-5 [mm]	Distance 3-7 [mm]	$\lambda$	$\varphi$	$\zeta$	$\varepsilon$
554.80	191.40	390.30	155.90	65.82°	9.86°	96.12°	7.52°

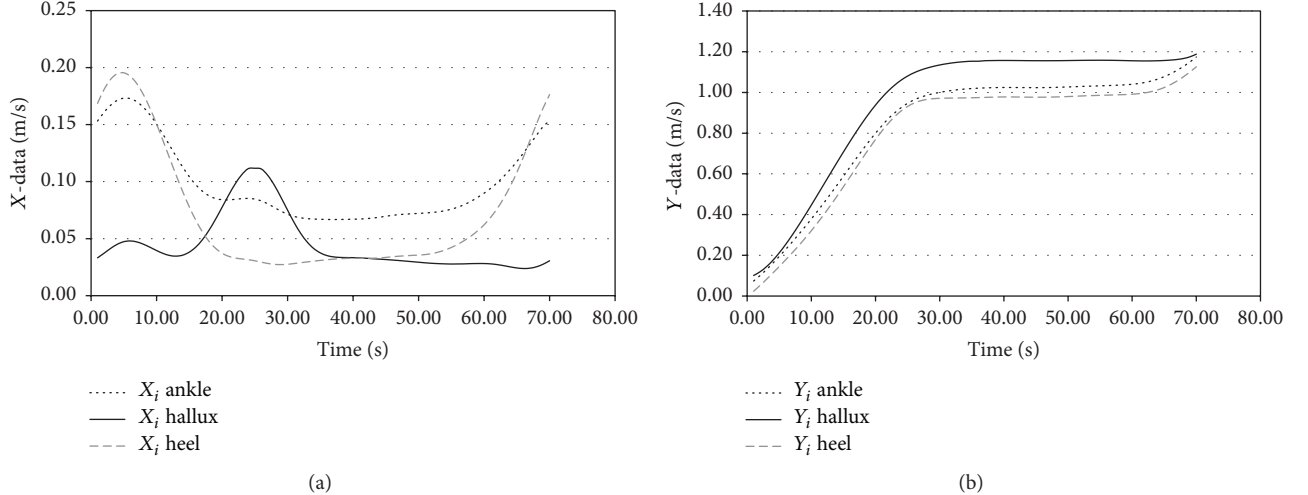


FIGURE 6: Trajectory in X-plane (a) and Y-plane (b) during rehabilitation task.

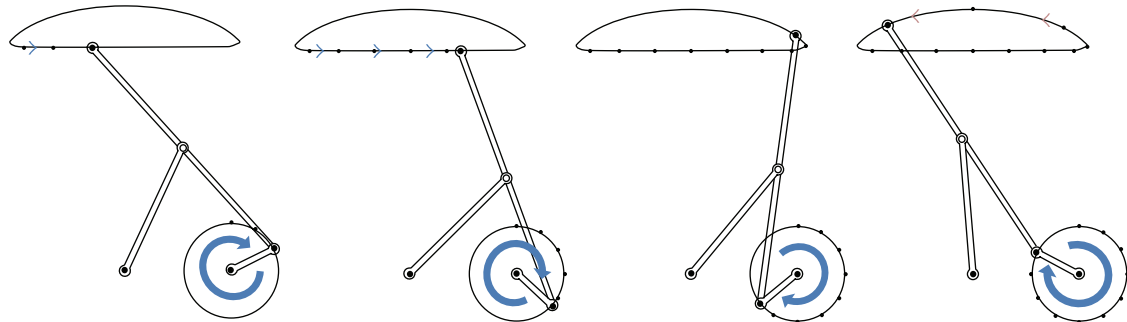


FIGURE 7: Noneccentric crank with single degree of freedom.

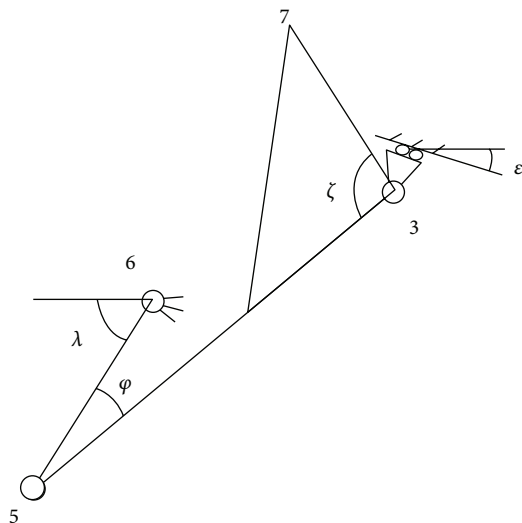


FIGURE 8: An overview of the articulated mechanism.

Figure 10. The design is composed of one motor that transmits power to both left and right limb.

The main benefits of the proposed rehabilitation system are as follows:

- (1) Modular design: individual customization is the adding-value due to trajectory/kinematics parameters setting and actuation system selection. For instance, the baseline is the walking cycle time of a healthy person close to 2 seconds while the duration for a patient can greatly vary depending on several factors (accident severity, rehabilitation stage, age, etc.).
- (2) Reliability and control: the system architecture based on a parallel mechanic can guarantee precision of movement while the patient's body remains stationary. In particular, this configuration permits controlling and monitoring the device easily (e.g., using

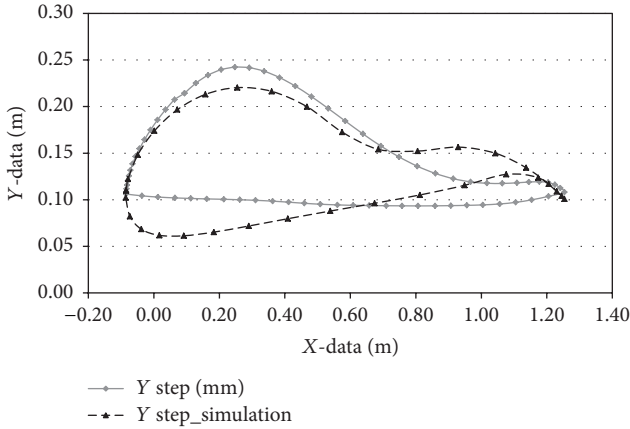


FIGURE 9: Comparison between measured and simulated trajectory in transverse plane during gait cycle.

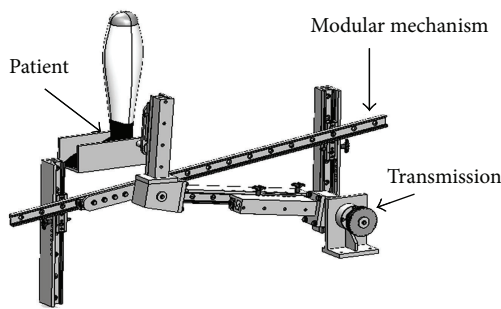


FIGURE 10: Modular mechanism system for ankle complex.

- feedback signal strategy) providing an effective and robust therapy.
- (3) Repeatability of movement: the device guarantees the repeatability of movement in particular for aged people.
  - (4) Adaptive control: usually the rehabilitation robots are position-based control, while this innovative control method is structure-based to provide torque assistance. The presented controller covers online learning platform able to monitor individual user performances during different rehabilitation gates.
  - (5) Errorless Learning approach: this device allows the creation of movement trajectories that encourage “Errorless Learning” approach where the patient needs to take an active part in movement initiation and execution. In fact it is often difficult to teach patient the correct motion of leg, specialty for aged people.
  - (6) Autonomous operation reducing the therapist contribution: patient can perform the rehabilitation exercise independently and easily, reducing the therapist's effort and guaranteeing the effectiveness of rehabilitation and safety.

- (7) Light-weight of structure and compactness design with an impact on commercialization and usability of device in medical applications.

In the light of these preliminary results, the next steps of the research will be based on further improvements of the rehabilitation device in terms of functionality and patients' safety. In particular a failure mode and effect analysis is suggested to identify all potential criticalities of system. This evaluation needs to consider and avoid any issues that may impact patients' safety during rehabilitation therapy (e.g., unexpected error of the system). The system will be equipped with footpads, additional lanes to relieve limbs, and a safety bar placed around the system to assure patient's safety during the rehabilitation exercises. The design review will identify the suitable actuation and control strategy. A preliminary evaluation suggested to use a feedback signal strategy in order to improve the therapy cycle controlling the main system parameters. This strategy permits customizing the therapy and guaranteeing the required movement. In particular, as shown in functional analysis, the walking cycle time (CT) of a healthy adult is close to 2 sec/step, while it may vary for a patient based on therapy. Assuming a very slow therapy (CT = 4 sec) and the worst case in terms of load (patient's weight equal to 150 kg), it is possible to simulate and calculate the maximum torque for system actuation. A preliminary calculation estimated a required torque close to 206 Nm considering whole mechanism and a safety factor equal to 1.2. The results of this further investigation will provide the system configuration suitable for prototype realization. The final purpose is to test and validate the rehabilitation device involving patients, physiotherapists, and physicians.

## 5. Conclusion

This paper introduces an ankle kinematic model and it uses this knowledge to design a device based on a parallel mechanism. This investigation focuses on the integration of human joint movements into rehabilitation device development in order to increase performance and effectiveness. The validity on physiotherapy of gait has been studied, modelling ankle movements during walking and assessing motion data from healthy individuals and patients. Using a functional analysis a preliminary rehabilitation system is proposed able to provide and guarantee the rehabilitation cycle and torque assistance during the required therapy. The study describes the technical features and requirements of the proposed device to guarantee patient's safety and therapy effectiveness. Using software simulations the ankle motion is successfully demonstrated by the rehabilitation system. Further investigations are required to complete and optimize the device, avoiding any potential issue that may impact patients' safety during rehabilitation exercise. In particular, a specific study will be performed to identify the most suitable footpads to guarantee an effective movement and a safe therapy. The design review will also suggest the correct actuation and control strategy. A preliminary study highlighted that the feedback control is a suitable method to improve the system performances. The final step is to propose a prototype to be

tested involving patients, physiotherapists, and physicians. Experimental validations on patients or healthy individuals play a key role in the effective application of the rehabilitation systems. The possibility to include analysis performed on patients should improve the dynamic control and the clinical effectiveness quantifying the ability and the progress during training process. A set of limits and constraints are still under investigation; in particular future works need also to focus on more complex and realistic environment training.

## Competing Interests

The authors declare that they have no competing interests.

## References

- [1] H. Kawamoto and Y. Sankai, "Comfortable, power assist control method for walking aid by HAL-3," in *Proceedings of the IEEE International Conference on Robotics and Automation*, vol. 4, October 2002.
- [2] M. Nordin and V. H. Frankel, *Basic Biomechanics of the Musculoskeletal System*, Lippincott Williams & Wilkins, Philadelphia, PA, USA, 3rd edition, 2001.
- [3] D. Simsik, M. Drutarovsky, P. Galajda, and A. Galajdova, "Embedded control of mechatronical rehabilitation shoe," *Engineering Media/ST. Zilina*, vol. 15, no. 5, pp. 1–6, 2011.
- [4] M. Girone, G. Burdea, M. Bouzit, V. Popescu, and J. E. Deutscher, "Stewart platform-based system for ankle telerehabilitation," *Autonomous Robots*, vol. 10, no. 2, pp. 203–212, 2001.
- [5] H. Yano, S. Tamefusa, N. Tanaka, H. Saitou, and H. Iwata, "Gait rehabilitation system for stair climbing and descending," in *Proceedings of the IEEE Haptics Symposium (HAPTICS '10)*, pp. 393–400, IEEE, Waltham, Mass, USA, March 2010.
- [6] T. Kikuchi, K. Oda, and J. Furusho, "Leg-robot for demonstration of spastic movements of brain-injured patients with compact magnetorheological fluid clutch," *Advanced Robotics*, vol. 24, no. 5–6, pp. 671–686, 2010.
- [7] J. Yoon and J. Ryu, "A novel reconfigurable ankle/foot rehabilitation robot," in *Proceedings of the IEEE International Conference on Robotics and Automation (ICRA '05)*, pp. 2290–2295, IEEE, Barcelona, Spain, April 2005.
- [8] J. S. Dai, T. Zhao, and C. Nester, "Sprained ankle physiotherapy based mechanism synthesis and stiffness analysis of a robotic rehabilitation device," *Autonomous Robots*, vol. 16, no. 2, pp. 207–218, 2004.
- [9] R. P. Wells, "The projection of the ground reaction force as a predictor of internal joint moments," *Bulletin of Prosthetics Research*, vol. 18, no. 1, pp. 15–19, 1981.
- [10] A. H. Hansen, D. S. Childress, S. C. Miff, S. A. Gard, and K. P. Mesplay, "The human ankle during walking: implications for design of biomimetic ankle prostheses," *Journal of Biomechanics*, vol. 37, no. 10, pp. 1467–1474, 2004.
- [11] S. Hesse, H. Schmidt, C. Werner, and A. Bardeleben, "Upper and lower extremity robotic devices for rehabilitation and for studying motor control," *Current Opinion in Neurology*, vol. 16, no. 6, pp. 705–710, 2003.
- [12] F. Sup, A. Bohara, and M. Goldfarb, "Design and control of a powered knee and ankle prosthesis," in *Proceedings of the IEEE International Conference on Robotics and Automation (ICRA '07)*, pp. 4134–4139, Roma, Italy, April 2007.
- [13] J. Bae, K. Haninger, D. Wai, X. Garcia, and M. Tomizuka, "A network-based monitoring system for rehabilitation," in *Proceedings of the IEEE/ASME International Conference on Advanced Intelligent Mechatronics (AIM '12)*, pp. 232–237, IEEE, Kachsiung, Taiwan, July 2012.
- [14] F. Aggogeri, A. Borboni, and R. Faglia, "Reliability roadmap for mechatronic systems," *Applied Mechanics and Materials*, vol. 373–375, pp. 130–133, 2013.
- [15] M. G. Pandy, "Simple and complex models for studying muscle function in walking," *Philosophical Transactions of the Royal Society B: Biological Sciences*, vol. 358, no. 1437, pp. 1501–1509, 2003.
- [16] D. Bradley, C. Acosta-Marquez, M. Hawley, S. Brownsell, P. Enderby, and S. Mawson, "NeXOS—the design, development and evaluation of a rehabilitation system for the lower limbs," *Mechatronics*, vol. 19, no. 2, pp. 247–257, 2009.
- [17] Y. Hurmuzlu and G. D. Moskowitz, "Bipedal locomotion stabilized by impact and switching," *Dynamics and Stability of Systems. An International Journal*, vol. 2, no. 2, pp. 73–96, 1987.
- [18] J. L. Emken, J. H. Wynne, S. J. Harkema, and D. J. Reinkensmeyer, "A robotic device for manipulating human stepping," *IEEE Transactions on Robotics*, vol. 22, no. 1, pp. 185–189, 2006.
- [19] S. K. Banala, S. H. Kim, S. K. Agrawal, and J. P. Scholz, "Robot assisted gait training with active leg exoskeleton (ALEX)," *IEEE Transactions on Neural Systems and Rehabilitation Engineering*, vol. 17, no. 1, pp. 2–8, 2009.
- [20] A. Agrawal, S. K. Banala, S. K. Agrawal, and S. A. Binder-Macleod, "Design of a two degree-of-freedom ankle-foot orthosis for robotic rehabilitation," in *Proceedings of the 9th International Conference on Rehabilitation Robotics (ICORR '05)*, pp. 41–44, IEEE, July 2005.
- [21] M. Zinn, O. Khatib, and B. Roth, "A new actuation approach for human friendly robot design," in *Proceedings of the IEEE International Conference on Robotics and Automation*, vol. 1, pp. 249–254, May 2004.
- [22] A. Takanishi, Y. Ogura, and K. Itoh, "Some issues in humanoid robot design," in *Proceedings of the International Symposium of Robotics Research*, 2005.
- [23] H. Saito, T. Watanabe, and A. Arifin, "Ankle and knee joint angle measurements during gait with wearable sensor system for rehabilitation," in *Proceedings of the World Congress on Medical Physics and Biomedical Engineering*, pp. 506–509, Munich, Germany, September 2009.
- [24] J. R. W. Morris, "Accelerometry—a technique for the measurement of human body movements," *Journal of Biomechanics*, vol. 6, pp. 729–736, 1973.
- [25] S. Tadano, R. Takeda, and H. Miyagawa, "Three dimensional gait analysis using wearable acceleration and gyro sensors based on quaternion calculations," *Sensors*, vol. 13, no. 7, pp. 9321–9343, 2013.
- [26] K. Tong and M. H. Granat, "A practical gait analysis system using gyroscopes," *Medical Engineering and Physics*, vol. 21, no. 2, pp. 87–94, 1999.
- [27] A. M. Sabatini, "Quaternion based attitude estimation algorithm applied to signals from body-mounted gyroscopes," *Electronics Letters*, vol. 40, no. 10, pp. 584–586, 2004.
- [28] E. Gentili, F. Aggogeri, and M. Mazzola, "The effectiveness of the quality function deployment in managing manufacturing and transactional processes," in *Proceedings of the ASME International Mechanical Engineering Congress and Exposition (IMECE '07)*, pp. 237–246, Seattle, Wash, USA, November 2007.

- [29] J. Yoon and J. Ryu, "A novel reconfigurable ankle/foot rehabilitation robot," in *Proceedings of the IEEE International Conference on Robotics and Automation*, pp. 2290–2295, IEEE, Barcelona, Spain, April 2005.
- [30] A. Hreljac and R. N. Marshall, "Algorithms to determine event timing during normal walking using kinematic data," *Journal of Biomechanics*, vol. 33, no. 6, pp. 783–786, 2000.
- [31] H. J. Woltring, "A Fortran package for generalized, cross-validated spline smoothing and differentiation," *Advances in Engineering Software*, vol. 8, no. 2, pp. 104–113, 1986.
- [32] F. C. Anderson and M. G. Pandy, "Individual muscle contributions to support in normal walking," *Gait and Posture*, vol. 17, no. 2, pp. 159–169, 2003.
- [33] R. B. Davis, S. Ounpuu, D. Tyburski, and J. R. Gage, "A gait analysis data collection and reduction technique," *Human Movement Science*, vol. 10, no. 5, pp. 575–587, 1991.

## Research Article

# Relationship between Lower Limb Angular Kinematic Variables and the Effectiveness of Sprinting during the Acceleration Phase

**Artur Struzik,<sup>1</sup> Grzegorz Konieczny,<sup>2</sup> Mateusz Stawarz,<sup>3</sup> Kamila Grzesik,<sup>3</sup> Sławomir Winiarski,<sup>4</sup> and Andrzej Rokita<sup>1</sup>**

<sup>1</sup>Department of Team Sport Games, University School of Physical Education, Mickiewicza 58 Street, 51-684 Wrocław, Poland

<sup>2</sup>Faculty of Health Sciences and Physical Education, Witelon State University of Applied Sciences, Sejmowa 5A Street, 59-220 Legnica, Poland

<sup>3</sup>University School of Physical Education, Paderewskiego 35 Avenue, 51-612 Wrocław, Poland

<sup>4</sup>Department of Biomechanics, University School of Physical Education, Mickiewicza 58 Street, 51-684 Wrocław, Poland

Correspondence should be addressed to Artur Struzik; artur.struzik@awf.wroc.pl

Received 15 April 2016; Accepted 23 June 2016

Academic Editor: Alberto Borboni

Copyright © 2016 Artur Struzik et al. This is an open access article distributed under the Creative Commons Attribution License, which permits unrestricted use, distribution, and reproduction in any medium, provided the original work is properly cited.

The ability to reach a high running velocity over a short distance is essential to a high playing performance in team games. The aim of this study was to determine the relationship between running time over a 10-meter section of a 30-meter sprint along a straight line and changes in the angle and angular velocity that were observed in the ankle, knee, and hip joints. The possible presence may help to optimize motion efficiency during acceleration sprint phase. Eighteen girls involved in team sports were examined in the study. The Fusion Smart Speed System was employed for running time measurements. The kinematic data were recorded using the Noraxon MyoMotion system. Statistically significant relationships were found between running time over a 10-meter section and the kinematic variables of hip and ankle joints. An excessively large flexion in hip joints might have an unfavorable effect on running time during the acceleration phase. Furthermore, in order to minimize running time during the acceleration phase, stride should be maintained along a line (a straight line) rather than from side to side. It is also necessary to ensure an adequate range of motion in the hip and ankle joints with respect to the sagittal axis.

## 1. Introduction

A 30-meter run is a popular test used by coaches in team sports in order to evaluate the level of speed abilities in athletes [1, 2]. Over such a distance, consecutive phases of a sprint can be distinguished in athletes from team sports: start, push-off, acceleration, and, contrary to sprinters, maximum velocity phase [1, 3–6]. The acceleration phase for these athletes is much shorter than that for track sprinters, and the maximal running velocity is reached earlier [1, 3, 5, 6]. However, the time of a 30-meter run should be interpreted carefully due to the substantial time differences within the test distance. For example, two athletes can have a similar running time over a 30-meter distance. However, the split times in individual sections of the run may differ significantly. Therefore, the individual sprinting workout of a player from team sports should be based on split time recordings [2, 3].

Running at a substantial velocity is observed among soccer players at 70–90-second intervals [2, 7, 8]. However, team sport players never reach maximal velocity during a sprint under actual game conditions [1, 6, 9]. Of all the sprints that are performed by soccer players, 49% are shorter than 10 m and 96% are shorter than 30 m [2, 7]. Therefore, the ability to reach high running velocity over a short distance (acceleration) is essential to high playing performance [1, 3, 6, 8–16]. Consequently, coaches should plan running workouts for team sport athletes that focus on the acceleration phase rather than maximum velocity [1, 6, 9]. The time it takes an athlete to run a 10-meter section is considered a measure of acceleration ability, and the distance of 10 meters is considered a conventional distance of acceleration (its initial part, with velocity increment being the highest) [6, 8, 10, 11, 13, 14, 17, 18].

Each of the sprinting phases is characterized by different technical and physiological demands to maximize motion efficiency. Therefore, different training programs should be designed to improve the individual phases of a sprint [3, 4, 13, 19]. The specific nature of each sport should also be considered because running technique used by athletes from team sports differs greatly from the technique that is used by track athletes [1, 3, 6, 20]. Team sport athletes run with a relatively lower height of the center of mass, less knee flexion during swing phase, and lower knee lift [1, 20]. This type of running helps team sport athletes to change their direction of movement faster [20].

The major goal of a team sport player when running over a short distance is to cover the distance as soon as possible in order to be ahead of either the offensive or defensive actions of the opponents. Therefore, a maximization of the horizontal component of velocity of the athlete's center of mass is needed. Running velocity is represented by a mathematical product of stride length and stride frequency. In order to maximize running velocity, it is necessary to proportionally increase both variables. Furthermore, each running phase requires different length-to-frequency ratios in order to maximize the effectiveness [9, 11, 12, 14, 19, 21, 22].

Acceleration ability can be improved by emphasizing the kinematic variables (which characterize the running technique) and/or kinetic variables (associated with the effect of force) during training, considering their mutual relations. The running technique should become the basis on which other variables, which are responsible for energy production or muscle strength, can be developed [9, 14, 15]. For example, a player with a greater potential for the development of high running velocity will lose to opponents due to a longer reaction time and poorer starting technique [23]. Teaching proper movement technique is essential in young athletes, with their training being more general and unfocused towards the development of strength abilities. During the acceleration phase, running technique should be most conducive to developing high speed in a short time [15]. Therefore, adequate synchronization of movements of the upper limbs with respect to the lower limbs is needed [22].

However, researchers do not agree on the most effective training method to improve acceleration ability and on which variables should be improved [9, 12, 14, 16, 17]. This is likely caused by an unclear contribution of individual joints to running performance [24]. Mann and Herman [21] reported that a lower value of knee extension at take-off positively affects sprinters' running times. Analogous conclusions were drawn by Murphy et al. [11] regarding the acceleration phase. Furthermore, Krell and Stefanyshyn [24] found that sprinters who had shorter running times were characterized by higher maximal rates of metatarsophalangeal extension. Ansari et al. [25] suggested that kinematic variables, such as knee angle, hip angle, ankle angle, shoulder rotation, and extension, are of key importance to the sprinting technique and have a clear effect on sprint performance. In contrast, Ranjan [26] found nonsignificant relationships between the angles in the knee, hip, and ankle joint and the sprint start performance. Lockie et al. [27] also did not find statistically significant

relationships between the 0–5 and 0–10 m sprint times and the angles in the knee, hip, and ankle joints.

A substantial number of accelerations and cuts over short distances resulting from changes in the direction of movement make the ability to reach a high running velocity over a short distance essential for high playing performance [1, 3, 6, 8–16]. However, the vast majority of studies on relationships between kinematic variables and running time have evaluated populations of runners [4, 17, 21, 22, 24–26]. Furthermore, reports concerning the running technique of young athletes from team sports are also scarce [5]. The aim of this study was to determine the relationship between the running time over a 10-meter section of a 30-meter sprint along a straight line and changes in the angle and angular velocity in the ankle, knee, and hip joints. Therefore, the authors attempted to answer the question of whether a technique of lower limb movement during the sprint acceleration phase significantly correlates with the running time over this section.

## 2. Materials and Methods

Examinations involving members of the Lower Silesian Voivodeship Team were carried out in a group of 265 participants selected from young people who trained in team sports (soccer, basketball, volleyball, and handball). Eighteen girls with the highest potential speed abilities were selected from this group. This selection was based on the maximum height of the countermovement jump [28]. The study group was characterized by the following mean values ( $\pm SD$ ): body height,  $165.5 \pm 10.5$  cm; body mass,  $52.4 \pm 10.3$  kg; and age,  $13.7 \pm 1.4$  years. Training experience was  $4.2 \pm 1.7$  years. Parents were informed about the purpose of the study and provided written permission for the tests. The experiments were carried out in the Ball Games Research Laboratory (with PN-EN ISO 9001:2009 certification). The research project was approved by the Senate's Research Bioethics Commission, and the procedure complied with the Declaration of Helsinki regarding human experimentation.

A fifteen-minute warm-up was administered before the measurements. The athletes performed a trial test before the measurement. Each participant performed two 30-meter runs over a straight line. The analysis was based on the trial with the shorter time of the first 10-meter section obtained by each participant. The distance to be run was purposively elongated in order to avoid the slow-down effect in the final part of the run [10].

The Fusion Smart Speed System (Fusion Sport, Coopers Plains, QLD, Australia) was used to measure the sprint time over individual sections. This system is comprised of gates, with each gate equipped in an infrared transmitter and a light reflector. A distance of 2 meters was adjusted between the infrared transmitter and the light reflector. Individual gates were spaced 5 meters (beginning from the start line) apart to record the time of crossing the infrared radiation beam. The gate at the distance of 30 meters denoted the finish line. The split times at distances of 5, 10, 15, 20, and 25 m were also recorded.

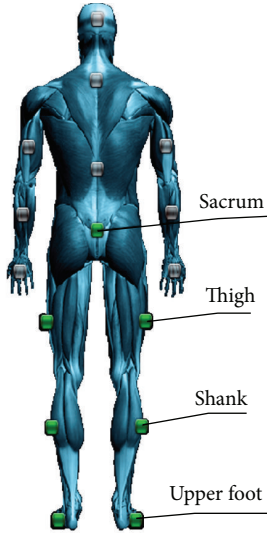


FIGURE 1: The places of deployment of inertial sensors (based on 16-joint-segment rigid-body model from MR3 software).

A Noraxon MyoMotion (Scottsdale, AZ, USA) motion analysis system was used to analyze the kinematic variables. A small inertial measurement unit (IMU) placed on a body segment tracks its 3D angular orientation. By placing individual IMU sensors on two neighbouring body segments, one can evaluate the range of motion in the joint placed between these segments. This principle might be extended from an individual movement of a joint over simultaneous measurement of the motion of the whole body in individual major joints. The MyoMotion sensors transmit the motion of the human body directly to the MyoMotion receiver to quantify the angular changes of the selected body segments. The information from a 3D accelerometer, gyroscope, and magnetometer is used to measure 3D rotation angles of each sensor in absolute space. The system is entirely wireless and does not need calibration of the measurement space, which allows for measurements outside the laboratory. System is entirely independent of external cameras. MyoMotion Research inertial sensors were placed according to the rigid-body model, with 16 joint segments used in the MR3 software on shoes (top of the upper foot, slightly below the ankle), shanks (frontal on the tibia bone), thighs (frontal attachment to the lower quadrant of the quadriceps, slightly above the knee cap, area of lowest muscle belly displacement in motion), and bony area of the sacrum (Figure 1). The sensors were attached with special fixation straps (for pelvis) and elastic straps. Calibration was carried out using the upright position in order to determine the value of the  $0^\circ$  angle in the studied joints. The sampling frequency for the inertial sensors was set at 200 Hz. Instantaneous changes in the joint angles in the area of the lower limb were recorded: hip joint (with respect to the long, transverse, and sagittal axes), knee joint (with respect to the transverse axis), and ankle joint (with respect to the long, transverse, and sagittal axes) during a 30-meter run along a straight line. Positive values of the angle depending on the joint and axis correspond to flexion,

abduction, external rotation, dorsiflexion, and inversion. The angular velocities in the area of these joints were determined based on the derivative of the distance (angle) over time [29].

The participants started from a standing position at the light signal. The left lower limb of a study participant was placed ahead of the start line so that the first step was performed with the right limb. Three entire running gait cycles were used for both the left and right lower limbs (steps 3 to 8 occurring during the acceleration phase), determined based on the instantaneous angle in the knee joint (the border between the cycles was the minimum value of the angle). Manual recognition was used to isolate the running gait cycles. The running steps were counted at a distance of 10 m, adopted as a conventional acceleration phase [6, 13, 18]. The first two running steps were neglected in the analysis because they started at the near-zero velocity, thus being substantially different from the other six.

Three entire gait cycles (as a whole) were normalized with respect to time and averaged for each lower limb separately. Then, the mean angle and angular velocity profiles were calculated with standard deviations. Before generating the graphical presentation shown in Figures 2 and 3, the profiles were smoothed. The procedure of standardization (normalization of variables) allows for intercomparison, even if the subjects have differed in terms of somatic parameters. Therefore, the curve shapes were normalized with respect to time (relative time expressed as a percentage).

In order to analyze the relationships between the sprint time over the section of 10 m and the individual kinematic variables, Spearman's rank correlation coefficient was used due to the lack of normal distribution of the studied variables. The level of significance was set at  $\alpha = 0.05$ . Furthermore, multiple regression was used to find the variable that was the most correlated with running time.

### 3. Results

Figure 2 presents the instantaneous changes in the angle in the area of lower limb joints: hip joint (with respect to the long, transverse, and sagittal axes), knee joint (with respect to the transverse axis), and ankle joint (with respect to the long, transverse, and sagittal axes) during the acceleration phase of a 30-meter run along a straight line. In Figure 2, steps 3, 5, and 7 (from the start line) for the right lower limb and steps 4, 6, and 8 (from the start line) for the left lower limb were presented. Analogously, changes in the variable of angular velocity are presented in Figure 3.

Statistically significant correlations between running time over a 10-meter section and individual kinematic variables of the hip joint were found for the maximum flexion angle, flexion-extension range of angular velocity, maximum adduction angle, maximum adduction angular velocity, maximum abduction angular velocity, abduction-adduction range of motion, and abduction-adduction range of angular velocity. Furthermore, statistically significant correlations between running time over a 10-meter section and individual kinematic variables of the ankle joint occurred for maximum eversion angular velocity, inversion-eversion range of angular velocity, maximum dorsiflexion angle, maximum plantar

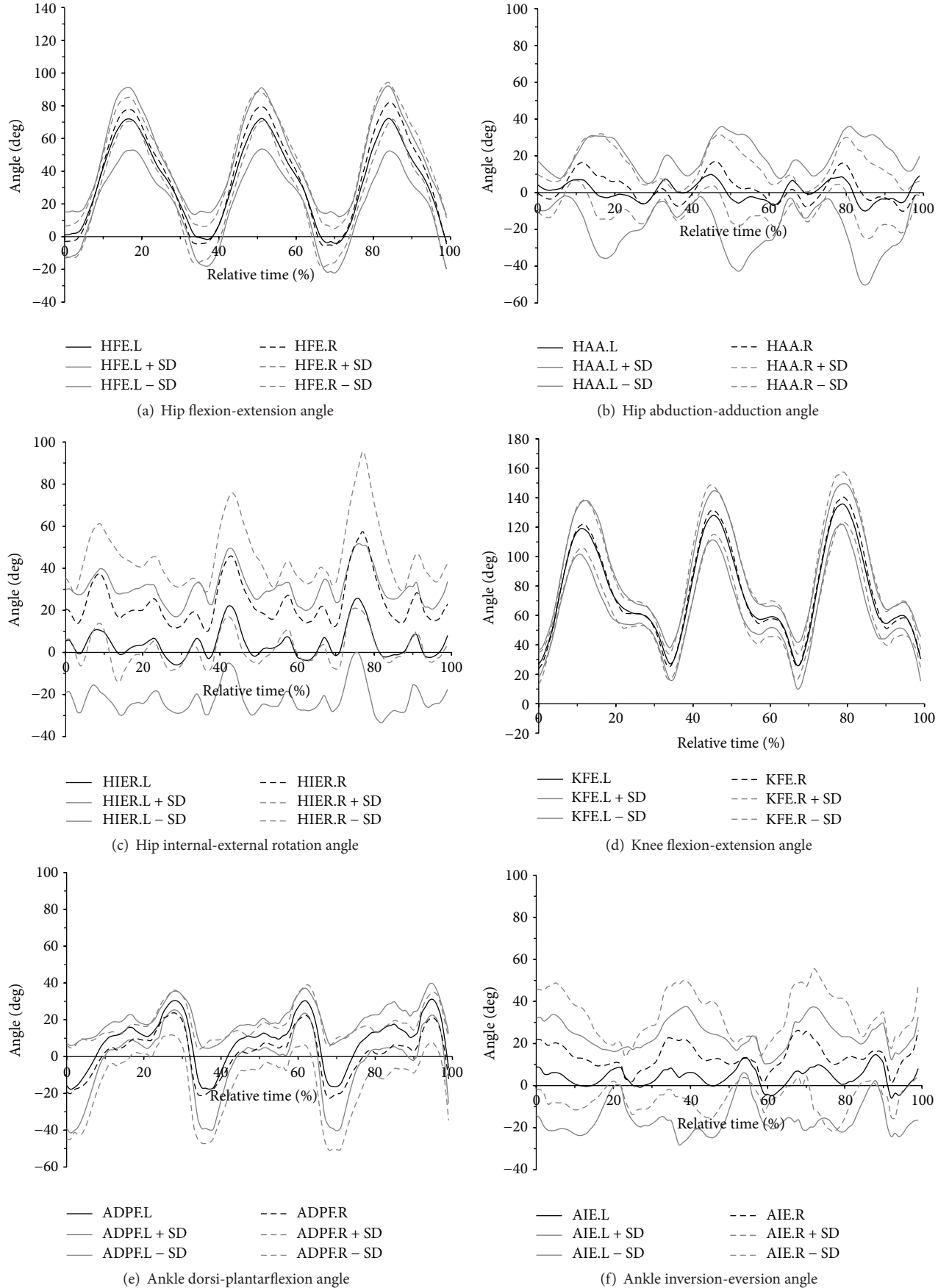


FIGURE 2: Continued.

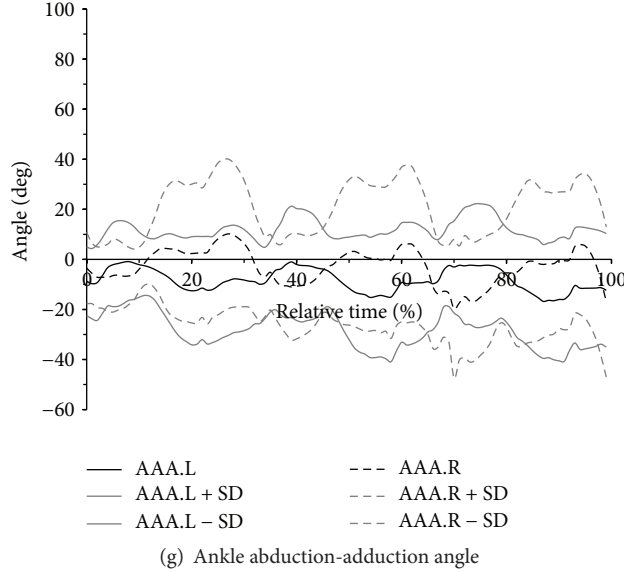


FIGURE 2: Instantaneous changes in the angle in the area of lower limb joints with respect to specific axes during a 30-meter sprint acceleration phase along a straight line for the left limb (continuous line) and right limb (dashed line).

flexion angle, maximum abduction angle, maximum abduction angular velocity, maximum adduction angle, maximum adduction angular velocity, abduction-adduction range of motion, and abduction-adduction range of angular velocity. For other recorded variables of the hip joint and ankle joint, the relationships with running time over a 10-meter section were not statistically significant. These correlations differed in their magnitude and significance depending on the running gait. Values of correlation coefficients for the hip joint are presented in Table 1, whereas these values for the ankle joint are shown in Table 2. No statistically significant correlations were found between running time over a 10-meter section and individual kinematic variables of the knee joint. Multiple regression analysis revealed that the most significant correlation with running time was observed for the maximum hip flexion angle during the eighth running step.

#### 4. Discussion

Statistically significant relationships between running time over a 10-meter section and kinematic variables of the lower limbs occurred most often for one of the body sides, mainly left (Tables 1 and 2). This observation might suggest that the movement pattern during the initial acceleration phase is somehow determined by the asymmetric start (the first step performed by the right lower limb). Therefore, despite alternate work of the limbs, the movement kinematics in the acceleration phase were not as symmetrical as in the maximal velocity phase [29]. Coaches should therefore focus on improving the acceleration phase and on starting from both the left and right legs (at zero initial velocity and at flying start). This improvement is associated with dynamically changing situations on the field or court, which cause team sport athletes to perform many explosive movements during

TABLE 1: Values of correlation coefficients ( $r$ ) between running time over a 10-meter section and individual kinematic variables of the hip joint.

Variable	Running step	$r$
Maximum flexion angle	4	0.47*
	8	0.56*
Flexion-extension range of angular velocity	4	-0.48*
	8	-0.60*
Maximum adduction angle	6	-0.65*
	8	-0.67*
Maximum adduction angular velocity	6	-0.47*
	8	-0.64*
Maximum abduction angular velocity	8	-0.52*
	4	-0.53*
Abduction-adduction range of motion	6	-0.53*
	8	-0.66*
Abduction-adduction range of angular velocity	6	-0.47*
	8	-0.68*

\* Statistically significant at  $p < 0.05$ .

the game, such as rapid starts, accelerations and cuts, changes in the direction of movement, or jumps. For instance, soccer players perform 150–250 brief intense actions lasting 1.9–2.7 s during a match [7]. The effectiveness of the above movements depends mainly on lower limb power [1, 2, 13, 19].

Lockie et al. [14, 15] argue that the beneficial effect on running time over a 10-meter section is from greater stride length, longer flight time, and shorter contact time.

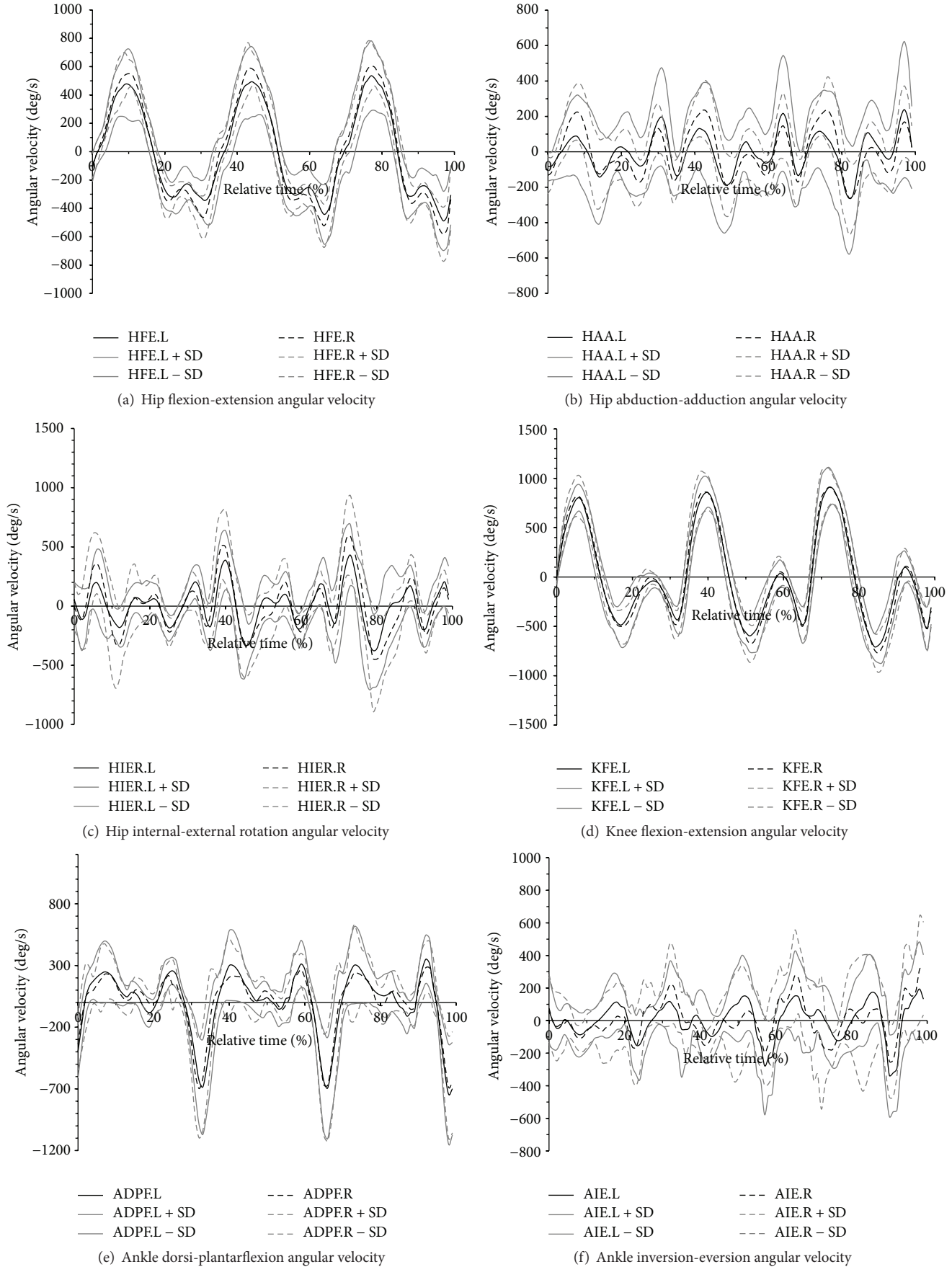


FIGURE 3: Continued.

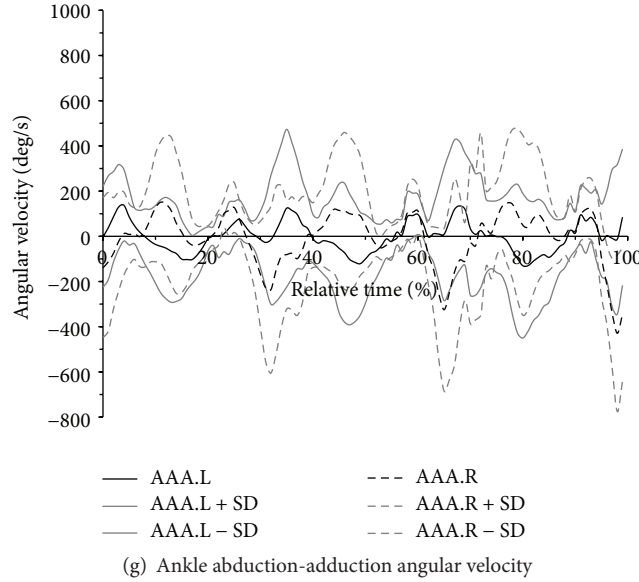


FIGURE 3: Instantaneous changes in the angular velocity in the area of lower limb joints with respect to specific axes during a 30-meter sprint acceleration phase along a straight line for the left limb (continuous line) and right limb (dashed line). Continuous or dashed thin grey lines were denoted  $\pm SD$  for the left and right limb, respectively.

TABLE 2: Values of correlation coefficients ( $r$ ) between running time over a 10-meter section and individual kinematic variables of the ankle joint.

Variable	Running step	$r$
Maximum eversion angular velocity	8	-0.50*
Inversion-eversion range of angular velocity	8	-0.47*
Maximum dorsiflexion angle	3	0.64*
Maximum plantar flexion angle	5	-0.49*
Maximum abduction angle	5	0.48*
Maximum abduction angular velocity	4	-0.60*
	6	-0.47*
Maximum adduction angle	6	-0.59*
	8	-0.65*
Maximum adduction angular velocity	4	-0.67*
	4	-0.74*
Abduction-adduction range of motion	6	-0.56*
	8	-0.55*
Abduction-adduction range of angular velocity	4	-0.75*
	6	-0.56*

\* Statistically significant at  $p < 0.05$ .

However, the statistically significant positive correlations between running time over a 10-meter section and maximal hip flexion angle (steps 4 and 8) suggest that excessively large flexion in hip joints is unfavorable for running time during the acceleration phase. Furthermore, the maximum

hip flexion angle during the eighth running step showed the highest relationship with running time among all of the studied variables. These relationships may suggest that the stride length during the acceleration phase should not be too long. This result is likely to be supported by the lack of statistically significant relationships between the running time over a 10-meter section and kinematic variables for the knee joint with respect to the transverse axis. Statistically significant relationships between the running time over a 10-meter section and the dorsiflexion angle (positive, step 3) and plantar flexion angle (negative, step 5) appear to support this thesis. Therefore, it seems that the running stride should be performed dynamically (shorter contact time) rather than strongly forward (adequate proportion of stride length to stride frequency). This result appears to be supported by a statistically significant negative relationship between running time over a 10-meter section and the hip flexion-extension range of angular velocity (step 4). Indeed, some authors have documented a beneficial effect of stride frequency on the effectiveness of the acceleration phase [9, 11]. Therefore, in order to improve the acceleration phase, coaches should consider exercises that increase power in the lower limbs. The running stride during a sprint can be regarded as a ballistic movement due to the duration of the phase of foot contact with the ground being shorter than 0.2 s [9, 13–16, 19]. The athletes studied by Lockie et al. [14, 15] were much older ( $22.6 \pm 3.2$  years) than the athletes included in our study, which may justify the differences. However, the step frequency is more difficult to improve than the step length during the training process. Additionally, faster athletes employ a higher step frequency with a similar step length to those of their slower counterparts [17]. It has been suggested that the angle between the thigh and body trunk during the acceleration phase should be approximately  $90^\circ$

[16]. However, the athletes who participated in our study obtained the following mean values of maximal hip flexion:  $78.3 \pm 7.1^\circ$  (third step),  $74.1 \pm 16.5^\circ$  (fourth step),  $81.7 \pm 8.2^\circ$  (fifth step),  $75.1 \pm 16.8^\circ$  (sixth step),  $83.8 \pm 10.4^\circ$  (seventh step), and  $75.8 \pm 17.3^\circ$  (eighth step). Therefore, the above values were slightly smaller than those suggested by Spinks et al. [16].

Statistically significant negative relationships between running time over a 10-meter section and the maximal adduction angle for the hip joint (steps 4, 6, and 8) and ankle joint (steps 6 and 8) may demonstrate that the running gait should be performed in a line consistent with the direction of running (straight line) rather than from side to side. This result appears to be supported by a statistically significant positive relationship between running time over a 10-meter section and the maximum abduction angle in the ankle joint (step 5). An efficient sprint involves placing the foot closer to the location of the vertical projection (on the ground) of the center of gravity of the runner's body. In order to counteract the horizontal deceleration, the foot, after contacting the ground, should move towards the rear with respect to the general center of gravity with the horizontal velocity, which is at least equal compared to the velocity of the general center of gravity of the running person [21]. Statistically significant negative relationships between the running time over a 10-meter section and the maximal values and range of angular velocity with respect to the sagittal axis of the hip joint and ankle joint and with respect to the long axis of the ankle joint (Tables 1 and 2) seem to support the need for performing the running gait as dynamically as possible.

Ansari et al. [25] suggest that kinematic variables, such as the hip angle, knee angle, and ankle angle, are essential to the sprinting technique. In contrast, Ranjan [26] and Lockie et al. [27] did not find statistically significant relationships between the angles in the knee, hip, and ankle joints and the sprint performance. In the present study, only the kinematic variables of the hip joint and ankle joint showed a significant relationships with the running time over a 10-meter section of a 30-meter sprint. Theoretically, a greater range of motion and knee flexion angle should also positively affect sprint performance. During the recovery portion of the stride, the heel should remain as close to the hips (buttocks) as possible, which helps to shorten the inertia radius and achieve a higher angular velocity in the knee joint [21, 25, 30]. However, Mann and Herman [21] and Murphy et al. [11] have demonstrated that a lower value of knee extension at take-off positively affects the running time for sprinters, which might result from differences in the motion pattern that should occur in the acceleration phase and maximal velocity phase. However, no statistically significant relationships were found in our study between running time and the values of angles, angular velocities, and range of motion in the knee joint. A lack of these relationships may suggest that this part of the motion pattern was performed properly by the participants rather than the variables do not affect running time.

Statistically significant negative relationships were found between running time over a 10-meter section and the ranges of motion of the hip joint (steps 4, 6, and 8) and the ankle joint (steps 4, 6, and 8) in the sagittal plane. Therefore, in order to maximize the velocity (minimize time) of running

during the acceleration phase, an adequate level of mobility with respect to the sagittal plane in the hip joint and the ankle joint is needed. A relatively high range of motion in the joints of the lower limb is necessary to obtain an adequate running stride [27].

## 5. Conclusions

This study contains technical running guidelines for young athletes that can be used during training. However, it should be noted that the relationships between running time over a 10-meter section of a 30-meter sprint and kinematic variables of lower limbs might differ depending on the age of the athletes, the sport, and the running technique level. Movement technique also depends on the running phase. The relationships between running time over a 10-meter section of a 30-meter sprint and the kinematic variables of the lower limbs refer only to the technical aspect of the running gait, which does not consider (directly) the kinetic variables. Therefore, further studies should be extended by kinetic variables of the lower limbs and the search for relationships between kinetic and kinematic variables. The actual practical implications can be reduced to the three conclusions presented below:

- (1) An excessively large flexion in hip joints might have an unfavorable effect on running time during the acceleration phase of a 30-meter sprint.
- (2) In order to minimize running time during the acceleration phase, running should be maintained more in a line (a straight line) rather than from side to side.
- (3) A beneficial relationship with running time during the acceleration phase was found for the range of motion in hip and ankle joints with respect to the sagittal axis.

## Competing Interests

The authors declare that they have no competing interests.

## Acknowledgments

This study was made possible by funds from the Polish Ministry of Science and Higher Education within the program "Development of Academic Sport 2013" (Grant no. RSA2 019 52).

## References

- [1] J. B. Cronin and K. T. Hansen, "Strength and power predictors of sports speed," *Journal of Strength and Conditioning Research*, vol. 19, no. 2, pp. 349–357, 2005.
- [2] U. Wisloff, C. Castagna, J. Helgerud, R. Jones, and J. Hoff, "Strong correlation of maximal squat strength with sprint performance and vertical jump height in elite soccer players," *British Journal of Sports Medicine*, vol. 38, no. 3, pp. 285–288, 2004.
- [3] M. J. Barr, J. M. Sheppard, T. J. Gabbett, and R. U. Newton, "Long-term training-induced changes in sprinting speed and

- sprint momentum in elite rugby union players," *Journal of Strength and Conditioning Research*, vol. 28, no. 10, pp. 2724–2731, 2014.
- [4] L. Charalambous, G. Irwin, I. N. Bezodis, and D. Kerwin, "Lower limb joint kinetics and ankle joint stiffness in the sprint start push-off," *Journal of Sports Sciences*, vol. 30, no. 1, pp. 1–9, 2012.
  - [5] M. C. Rumpf, J. B. Cronin, J. L. Oliver, and M. Hughes, "Assessing youth sprint ability-methodological issues, reliability and performance data," *Pediatric Exercise Science*, vol. 23, no. 4, pp. 442–467, 2011.
  - [6] W. Young, B. McLean, and J. Ardagna, "Relationship between strength qualities and sprinting performance," *The Journal of Sports Medicine and Physical Fitness*, vol. 35, no. 1, pp. 13–19, 1995.
  - [7] T. Cotte and J.-C. Chatard, "Isokinetic strength and sprint times in English Premier League football players," *Biology of Sport*, vol. 28, no. 2, pp. 89–94, 2011.
  - [8] M. A. Newman, K. M. Tarpenning, and F. E. Marino, "Relationships between isokinetic knee strength, single-sprint performance, and repeated-sprint ability in football players," *Journal of Strength and Conditioning Research*, vol. 18, no. 4, pp. 867–872, 2004.
  - [9] R. G. Lockie, A. J. Murphy, T. J. Knight, and X. A. K. Janse de Jonge, "Factors that differentiate acceleration ability in field sport athletes," *Journal of Strength and Conditioning Research*, vol. 25, no. 10, pp. 2704–2714, 2011.
  - [10] G. Moir, C. Button, M. Glaister, and M. H. Stone, "Influence of familiarization on the reliability of vertical jump and acceleration sprinting performance in physically active men," *Journal of Strength and Conditioning Research*, vol. 18, no. 2, pp. 276–280, 2004.
  - [11] A. J. Murphy, R. G. Lockie, and A. J. Coutts, "Kinematic determinants of early acceleration in field sport athletes," *Journal of Sports Science and Medicine*, vol. 2, no. 4, pp. 144–150, 2003.
  - [12] G. D. Myer, K. R. Ford, J. L. Brent, J. G. Divine, and T. E. Hewett, "Predictors of sprint start speed: the effects of resistive ground-based vs. inclined treadmill training," *Journal of Strength and Conditioning Research*, vol. 21, no. 3, pp. 831–836, 2007.
  - [13] R. G. Lockie, A. J. Murphy, A. B. Schultz, T. J. Knight, and X. A. K. Janse de Jonge, "The effects of different speed training protocols on sprint acceleration kinematics and muscle strength and power in field sport athletes," *Journal of Strength and Conditioning Research*, vol. 26, no. 6, pp. 1539–1550, 2012.
  - [14] R. G. Lockie, A. J. Murphy, M. D. Jeffriess, and S. J. Callaghan, "Step kinematic predictors of short sprint performance in field sport athletes," *Serbian Journal of Sports Sciences*, vol. 7, no. 2, pp. 71–77, 2013.
  - [15] R. G. Lockie, A. J. Murphy, A. B. Schultz, M. D. Jeffriess, and S. J. Callaghan, "Influence of sprint acceleration stance kinetics on velocity and step kinematics in field sport athletes," *Journal of Strength and Conditioning Research*, vol. 27, no. 9, pp. 2494–2503, 2013.
  - [16] C. D. Spinks, A. J. Murphy, W. L. Spinks, and R. G. Lockie, "The effects of resisted sprint training on acceleration performance and kinematics in soccer, rugby union, and Australian football players," *Journal of Strength and Conditioning Research*, vol. 21, no. 1, pp. 77–85, 2007.
  - [17] P. S. Maulder, E. J. Bradshaw, and J. W. L. Keogh, "Kinematic alterations due to different loading schemes in early acceleration sprint performance from starting blocks," *Journal of Strength and Conditioning Research*, vol. 22, no. 6, pp. 1992–2002, 2008.
  - [18] S. Nimpfius, M. R. McGuigan, and R. U. Newton, "Relationship between strength, power, speed, and change of direction performance of female softball players," *Journal of Strength and Conditioning Research*, vol. 24, no. 4, pp. 885–895, 2010.
  - [19] S. Debaere, C. Delecluse, D. Aerdenhouts, F. Hagman, and I. Jonkers, "From block clearance to sprint running: characteristics underlying an effective transition," *Journal of Sports Sciences*, vol. 31, no. 2, pp. 137–149, 2013.
  - [20] W. B. Young, R. James, and I. Montgomery, "Is muscle power related to running speed with changes of direction?" *Journal of Sports Medicine and Physical Fitness*, vol. 42, no. 3, pp. 282–288, 2002.
  - [21] R. Mann and J. Herman, "Kinematic analysis of Olympic sprint performance: men's 200 meters," *Journal of Applied Biomechanics*, vol. 1, no. 3, pp. 151–162, 1985.
  - [22] J. Slawinski, A. Bonnefoy, G. Ontanon et al., "Segment-interaction in sprint start: analysis of 3D angular velocity and kinetic energy in elite sprinters," *Journal of Biomechanics*, vol. 43, no. 8, pp. 1494–1502, 2010.
  - [23] A. Struzik, A. Rokita, B. Pietraszewski, and M. Popowczak, "Accuracy of replicating static torque and its effect on shooting accuracy in young basketball players," *Human Movement*, vol. 15, no. 4, pp. 216–220, 2014.
  - [24] J. B. Krell and D. J. Stefanyshyn, "The relationship between extension of the metatarsophalangeal joint and sprint time for 100 m olympic athletes," *Journal of Sports Sciences*, vol. 24, no. 2, pp. 175–180, 2006.
  - [25] N. W. Ansari, Y. Paul, and K. Sharma, "Kinematic analysis of competitive sprinting," *African Journal for Physical, Health Education, Recreation and Dance*, vol. 18, no. 4, pp. 662–671, 2012.
  - [26] C. Ranjan, "The relationship of selected kinematical variables to the performance of runners in sprint start," *International Journal of Sports Sciences and Fitness*, vol. 1, no. 1, pp. 60–67, 2011.
  - [27] R. G. Lockie, S. J. Callaghan, and M. D. Jeffriess, "Acceleration kinematics in cricketers: implications for performance in the field," *Journal of Sports Science and Medicine*, vol. 13, no. 1, pp. 128–136, 2014.
  - [28] W. Young, S. Cormack, and M. Crichton, "Which jump variables should be used to assess explosive leg muscle function?" *International Journal of Sports Physiology and Performance*, vol. 6, no. 1, pp. 51–57, 2011.
  - [29] A. Struzik, G. Konieczny, K. Grzesik, M. Stawarz, S. Winiarski, and A. Rokita, "Relationship between lower limbs kinematic variables and effectiveness of sprint during maximum velocity phase," *Acta of Bioengineering and Biomechanics*, vol. 17, no. 4, pp. 131–138, 2015.
  - [30] A. A. Biewener, C. T. Farley, T. J. Roberts, and M. Temaner, "Muscle mechanical advantage of human walking and running: implications for energy cost," *Journal of Applied Physiology*, vol. 97, no. 6, pp. 2266–2274, 2004.

## Research Article

# Microstructure and Mechanical Properties of Microwave Sintered $\text{ZrO}_2$ Bioceramics with $\text{TiO}_2$ Addition

Hsien-Nan Kuo,<sup>1</sup> Jyh-Horng Chou,<sup>1,2,3</sup> and Tung-Kuan Liu<sup>1</sup>

<sup>1</sup>*Institute of Engineering Science and Technology, National Kaohsiung First University of Science and Technology, 1 University Road, Kaohsiung 824, Taiwan*

<sup>2</sup>*Department of Electrical Engineering, National Kaohsiung University of Applied Sciences, 415 Chien-Kung Road, Kaohsiung 807, Taiwan*

<sup>3</sup>*Department of Healthcare Administration and Medical Informatics, Kaohsiung Medical University, 100 Shih-Chuan 1st Road, Kaohsiung 807, Taiwan*

Correspondence should be addressed to Hsien-Nan Kuo; andykuo8165@gmail.com

Received 27 April 2016; Accepted 23 June 2016

Academic Editor: Alberto Borboni

Copyright © 2016 Hsien-Nan Kuo et al. This is an open access article distributed under the Creative Commons Attribution License, which permits unrestricted use, distribution, and reproduction in any medium, provided the original work is properly cited.

The microwave sintered zirconia ceramics with 0, 1, 3, and 5 wt%  $\text{TiO}_2$  addition at a low sintering temperature of 1300°C and a short holding time of 1 hour were investigated. Effect of contents of  $\text{TiO}_2$  addition on microstructure and mechanical properties of microwave sintered zirconia bioceramics was reported. In the sintered samples, the main phase is monoclinic zirconia ( $\text{m-ZrO}_2$ ) phase and minor phase is tetragonal zirconia ( $\text{t-ZrO}_2$ ) phase. The grain sizes increased with increasing the  $\text{TiO}_2$  contents under the sintering temperature of 1300°C. Although the  $\text{TiO}_2$  phase was not detected in the XRD pattern, Ti and O elements were detected in the EDS analysis. The presence of  $\text{TiO}_2$  effectively improved grain growth of the  $\text{ZrO}_2$  ceramics. The Vickers hardness was in the range of 125 to 300 Hv and increased with the increase of  $\text{TiO}_2$  contents. Sintering temperature dependence on the Vickers hardness was also investigated from 1150°C to 1300°C, showing the increase of Vickers hardness with the increase of the sintering temperature as well as  $\text{TiO}_2$  addition.

## 1. Introduction

Zirconia ( $\text{ZrO}_2$ ) has become one of the most important ceramic materials since 1970s because of the discovery of transformation toughening mechanisms. There are three different polymorphs which existed in pure zirconia, such as monoclinic (m), tetragonal (t), and cubic (c) phases [1, 2]. It is well known that the monoclinic phase existed and is stable at room temperature up to 1170°C; the tetragonal phase is formed and is stable at temperatures above 1170°C up to 2370°C; and the cubic phase is stable above 2370°C [3]. These existent phases depend on the temperature and compositional ranges under equilibrium conditions. Moreover,  $\text{ZrO}_2$  ceramic shows many special properties, such as high elastic modulus, high fracture toughness, high wear resistance, suitable ionic conductivity, chemical inertness, and high melting temperature [2, 4]. Because of such excellent physical and chemical properties,  $\text{ZrO}_2$  ceramic is attractive

to be a biomaterial and is a popular alternative to alumina as dental bioceramic [5–7].

To increase its industrial applicability, it is desired to retain the tetragonal phase at room temperature to provide favorable mechanical properties. Namely, methods for keeping the  $\text{ZrO}_2$  based solid solution as the tetragonal (t) phase and preventing deleterious t → m phase transformation during cooling after sintering shall be developed [2, 6]. In past, many research efforts reported that a proper percentage of stabilizers such as  $\text{Y}_2\text{O}_3$ ,  $\text{CeO}_2$ , and  $\text{MgO}$  could be used to hold the tetragonal phase from 1170°C to the room temperature, inhibiting the happening of crack propagation and providing relatively high fracture toughness [2, 6–9]. In addition, the combination of uniform grain size and densification of the  $\text{ZrO}_2$  based ceramics can in turn improve the mechanical properties [9]. Therefore, the processing of starting powders, composition, and sintering condition such as sintering time and temperature

are important parameters to prepare the high quality bioceramics.

It is known that, in conventional solid state sintering, the heat is transmitted radiantly to the surface of the material and reaches the internal core of the material by thermal conduction [10]. The sintered piece has approximately 22~25% shrinkage after final sintering. Typically, conventional solid state sintering may not provide uniform heating distribution and requires extended sintering process from 8 to 10 hours for the sintering of  $\text{ZrO}_2$  dental sample, causing much energy consumption [7].

Microwave sintering technology has been used for sintering ceramic materials. In the microwave sintering environment, the suitable material absorbs energy through dielectric heating, and the temperature is more uniformly distributed in the ceramic material [11–14]. Since microwave sintering technology has many attractive features, including uniform heating distribution, rapid volumetric heating, and low cost, it leads to the higher production rates and lower energy consumption. Compared to the conventional sintering technology, it makes the process commercially attractive. Estimates of energy saving are 25% to 95% [14]. However, high purity  $\text{ZrO}_2$  is a low absorber of microwave energy. Therefore, addition of  $\text{TiO}_2$  into high purity  $\text{ZrO}_2$  was provided to improve the microwave coupling at a given temperature [10, 15]. It is expected that microwave sintering would have a lower temperature (below 1400°C) and a shorter process (2 hours) than conventional sintering [16]. The sintering temperature, the heating rate, and the sintering time can affect the grain size, density, and mechanical properties of the sintered  $\text{ZrO}_2$  ceramic.

In this paper, the aim of this study is to investigate the effect of  $\text{TiO}_2$  content on the microstructure and mechanical properties of the microwave sintered  $\text{ZrO}_2$  with  $\text{TiO}_2$  addition at a low sintering temperature and a short holding time. In addition, the relation between the microstructure and mechanical properties is also discussed. Moreover, the dependence of the sintering temperature on the Vickers hardness was also investigated from 1150°C to 1300°C to verify the importance of  $\text{TiO}_2$  addition.

## 2. Materials and Methods

In this study, starting powders used  $\text{ZrO}_2$  with purity of 99.9% and  $\text{TiO}_2$  with purity of 99.85%. Four composite samples were prepared by adding  $\text{TiO}_2$  content from 0, 1, 3, and 5 wt% into  $\text{ZrO}_2$ , respectively. The powders were mixed by wet ball-milling for 12 h in ethanol, using high purity zirconia balls as medium to achieve a homogeneous mixture. After milling, the mixed powders were dried at 90°C for 10 h. The dried powders were mechanically grounded and added with 10 wt% PVA solution. Five green samples, for each composition, with a diameter of 10 mm and a thickness of 1 mm were formed by uniaxially pressing. The samples were microwave sintered at the sintering temperatures of 1150, 1200, 1250, and 1300°C for a holding time of 1 hour in microwave oven. The heating rate was varied as 100°C/min up to 300°C for 1 h to burn out the binder and 100°C/min up to the final temperature under air atmosphere. The sintered samples were naturally

cooled to the room temperature. In the study, the microwave furnace (Therm Wave Mod. III), with a continuously variable power of 2.45 GHz microwaves up to 1.3 kW, was used. To provide indirect heating of the powders, silicon carbide (SiC), having a very strong heating response to 2.45 GHz microwaves, was used as a susceptor. The samples were placed in the center of the susceptor and the sintering temperature was measured by insertion of a thermal couple around the susceptor.

After sintering, the diameter and thickness of each sintered sample were measured with a digital caliper to calculate the shrinkage percent. The crystalline phases of the composite specimens were conducted by using X-ray diffraction (XRD, Bruker D8 Advance) analysis with  $\text{CuK}\alpha$  radiation of  $\lambda = 1.5406 \text{ \AA}$  using a Ni filter and with a secondary graphite monochromator. A scanning range of  $2\theta = 20^\circ \sim 60^\circ$  with a step of 0.03° and 0.4 s as a count time per step was used. The morphology of the sintered samples was examined by scanning electron microscope (SEM, HORIBA EX-200) with the function of energy dispersive spectroscopy (EDS). The average grain size of the microwave sintered samples was obtained by analyzing SEM images using the linear intercept method on the fracture surfaces. The hardness of the sintered samples was conducted at room temperature by a micro-Vickers hardness tester (HM-113, Japan) with an indent load of 5 g held for 6 s on the surface of the microwave sintered samples. The measurement was repeated five times for each sample. With removal of the largest and smallest values during the measurement, the average value was determined to be the measured result.

## 3. Results and Discussion

**3.1. XRD Analysis.** Figure 1 shows the XRD patterns of the microwave sintered  $\text{ZrO}_2$  samples with addition of 0, 1, 3, and 5 wt%  $\text{TiO}_2$  contents at 1300°C for 1 h. The main diffraction patterns of the tetragonal phase are around  $2\theta = 30^\circ$ ,  $51^\circ$ , and  $60^\circ$ . In these patterns, it was found that the diffraction patterns with reflections in  $2\theta = 28^\circ$  and  $31^\circ$  were related to the main phase of monoclinic zirconia and low diffraction intensity with reflection in  $2\theta = 50.36^\circ$  was related to second phase of tetragonal zirconia in the sintered samples for different  $\text{TiO}_2$  content [2, 6]. As reported in many researches, low-temperature cubic and tetragonal phases are meta-stable and would be converted into the monoclinic phase during cooling. Typically, the addition of stabilizers, such as  $\text{Y}_2\text{O}_3$ ,  $\text{CeO}_2$ ,  $\text{CaO}$ , and  $\text{MgO}$ , to pure  $\text{ZrO}_2$  can provide multiphases which coexisted in a material, known as Partially Stabilized Zirconia (PSZ) [1, 2]. In this study, the addition of  $\text{TiO}_2$  seemed not to prevent  $t \rightarrow m$  phase transformation during cooling. The result might be caused from the sintering temperature of 1300°C and the holding time of 1 hour which were much lower than conventional sintering temperature and time for the stabilizer [8]. However, the intensities of main monoclinic ( $m$ ) phases with reflections in  $2\theta = 28^\circ$  and  $31^\circ$  both slightly decreased with increasing  $\text{TiO}_2$  content, indicating  $\text{TiO}_2$  additions into pure  $\text{ZrO}_2$  still have an effect on the phase transformation.

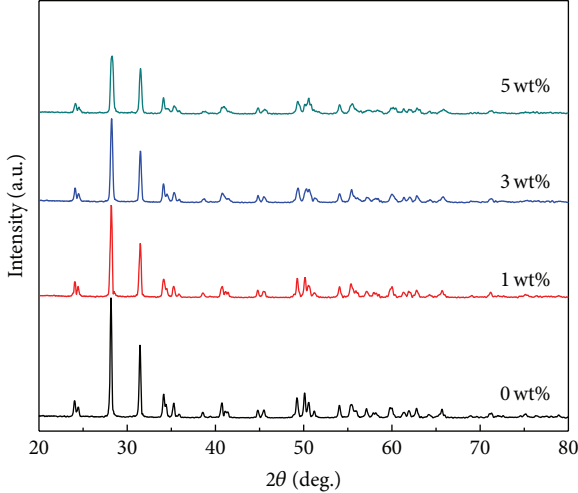


FIGURE 1: XRD patterns of the microwave sintered  $\text{ZrO}_2$  samples with addition of 0, 1, 3, and 5 wt%  $\text{TiO}_2$  contents.

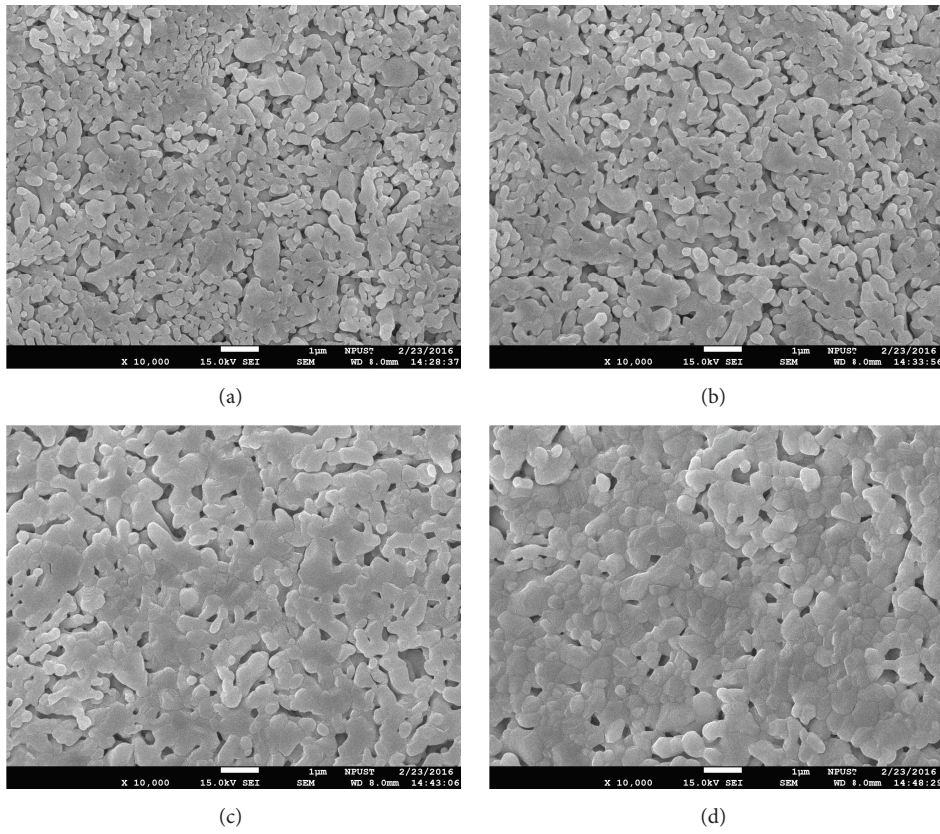


FIGURE 2: SEM of the microwave sintered  $\text{ZrO}_2$  ceramics with addition of (a) 0, (b) 1, (c) 3, and (d) 5 wt%  $\text{TiO}_2$  contents.

**3.2. Microstructure.** Under the microwave sintering temperature of  $1300^\circ\text{C}$  and the holding time of 1 hour, the linear shrinkage of the microwave sintered  $\text{ZrO}_2$  samples with different additions was approximately 16%. With the density measurement, the relative densities of microwave sintered  $\text{ZrO}_2$  ceramics with  $\text{TiO}_2$  addition achieved around 88% to 90%. Figure 2 shows SEM results of the microwave sintered  $\text{ZrO}_2$  ceramics with addition of (a) 0, (b) 1, (c) 3, and (d) 5 wt%

$\text{TiO}_2$  contents at  $1300^\circ\text{C}$  in 1 h. It is clearly observed that the grain sizes increased with increasing  $\text{TiO}_2$  contents. The grain sizes were 420 nm, 650 nm, 890 nm, and 1060 nm with the addition of  $\text{TiO}_2$  content with 0, 1, 3, and 5 wt%, respectively. The result indicated that the addition of  $\text{TiO}_2$  in  $\text{ZrO}_2$  ceramic could improve the grain growth and enhance the microwave sintering. Since the  $\text{TiO}_2$  phase was not detected in the XRD pattern, the  $\text{TiO}_2$  phase might be too small to be detected and

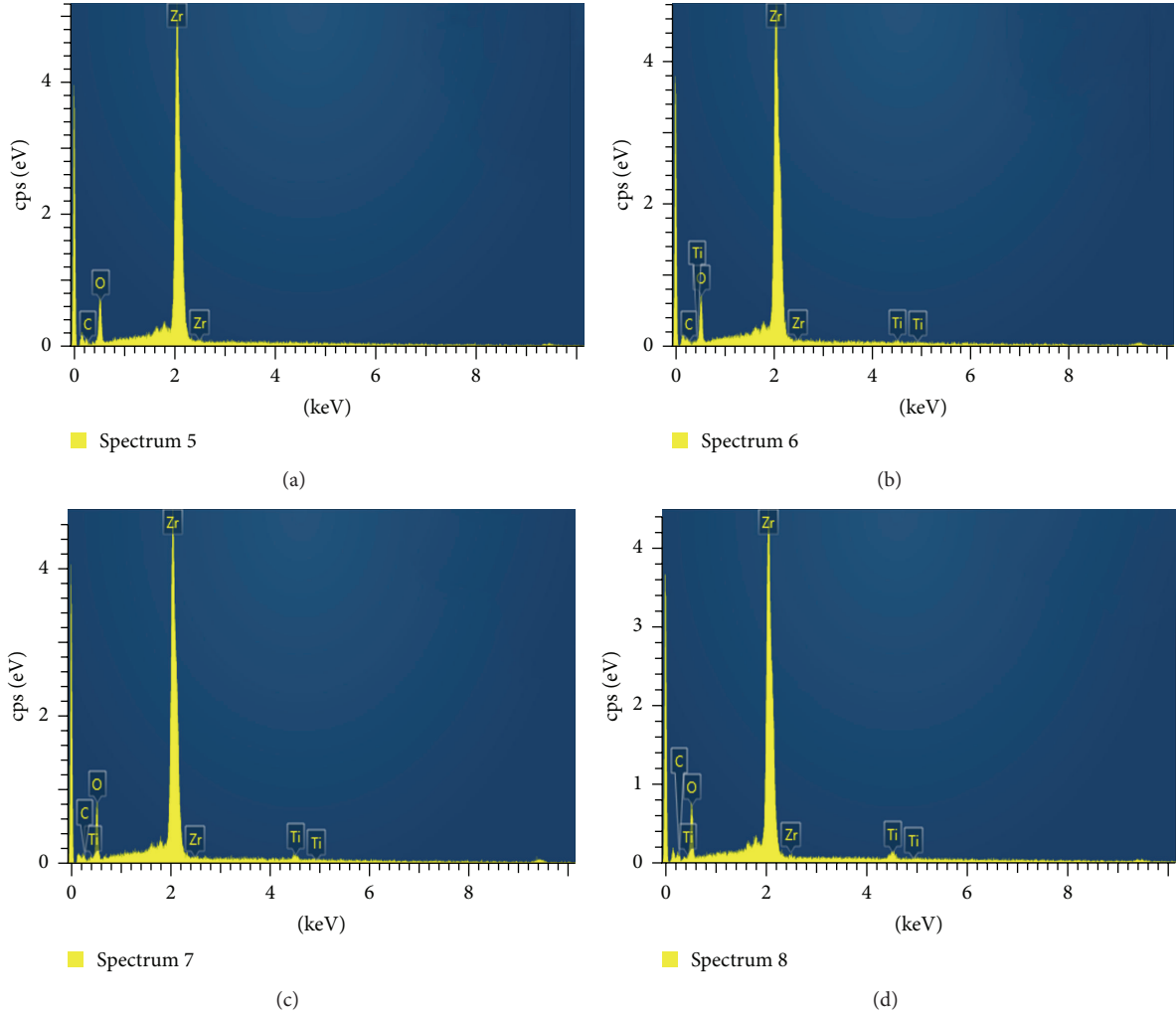


FIGURE 3: EDS analysis of the microwave sintered  $\text{ZrO}_2$  ceramics with addition of (a) 0, (b) 1, (c) 3, and (d) 5 wt%  $\text{TiO}_2$  contents.

$\text{TiO}_2$  addition was embedded around the  $\text{ZrO}_2$  grain and/or within the  $\text{ZrO}_2$  grain. Although the sintered samples did not achieve the full densification, it shall be noted that even at such a low temperature and a short holding time the  $\text{ZrO}_2$  grains were eventually coalesced with each other. At the triple junctions of the  $\text{ZrO}_2$  grains, some micro pores were present. It is known that the appearance of pores would increase the diffusion distance between  $\text{ZrO}_2$  grains, thus reducing the driving force for pore shrinkage of the sintered ceramics [6].

Figure 3 shows EDS analysis of the microwave sintered  $\text{ZrO}_2$  ceramics with addition of (a) 0, (b) 1, (c) 3, and (d) 5 wt%  $\text{TiO}_2$  contents. The EDS results verified that the content of  $\text{TiO}_2$  increased actually with increasing  $\text{TiO}_2$  addition. Although the  $\text{TiO}_2$  phase was not detected in the XRD pattern, Ti and O elements were detected in the EDS analysis. The presence of  $\text{TiO}_2$  on the grain and/or grain boundaries effectively improved the grain growth of the  $\text{ZrO}_2$  grains.

**3.3. Mechanical Properties.** Figure 4 shows the Vickers hardness of the  $\text{ZrO}_2$  ceramics with addition of 0, 1, 3, and 5 wt%  $\text{TiO}_2$  contents. Despite the errors associated with the measurement, it is found that the Vickers hardness of

the  $\text{ZrO}_2$  ceramic with addition of 0, 1, 3, and 5 wt%  $\text{TiO}_2$  contents was 125, 150, 250, and 300 Hv, respectively. The hardness values are low if the sintered samples are designed for dental use, since the sintered samples did not achieve the full densification under such a low temperature and a short holding time. Optical microscope of the  $\text{ZrO}_2$  ceramics with addition of (a) 0, (b) 1, (c) 3, and (d) 5 wt%  $\text{TiO}_2$  contents was shown in Figure 5. It is clearly observed that, under the same indent load, the lengths of the cross-indentation were decreased with increasing  $\text{TiO}_2$  contents. Thus, the larger length of the Vickers hardness indicated the shorter length of the cross-indentation. Typically, many factors would affect the Vickers hardness of ceramic materials, including the intrinsic deformability of the ceramic and the extrinsic microstructural features such as existent phases, grain size, crystal orientation, porosity, and boundary constitution [6, 8]. Under the microwave sintering temperature of 1300°C and the holding time of 1 hour, the main phase of monoclinic zirconia and second phase of tetragonal zirconia coexisted in the sintered samples with different  $\text{TiO}_2$  content, and the amount of the main phase was much larger than that of the second phase, as discussed in Figure 1. However, the grain

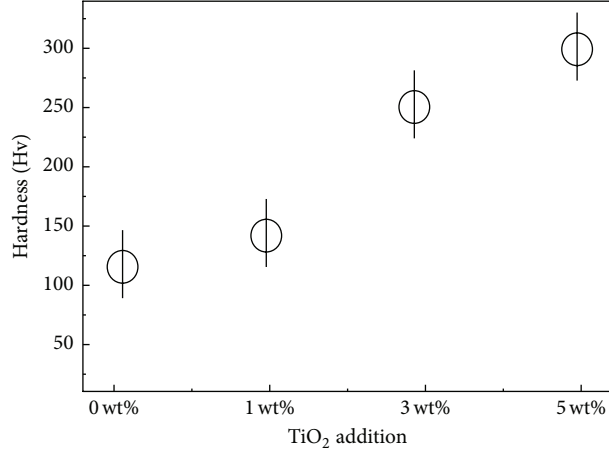


FIGURE 4: Vickers hardness of the ZrO<sub>2</sub> ceramics with addition of 0, 1, 3, and 5 wt% TiO<sub>2</sub> contents.

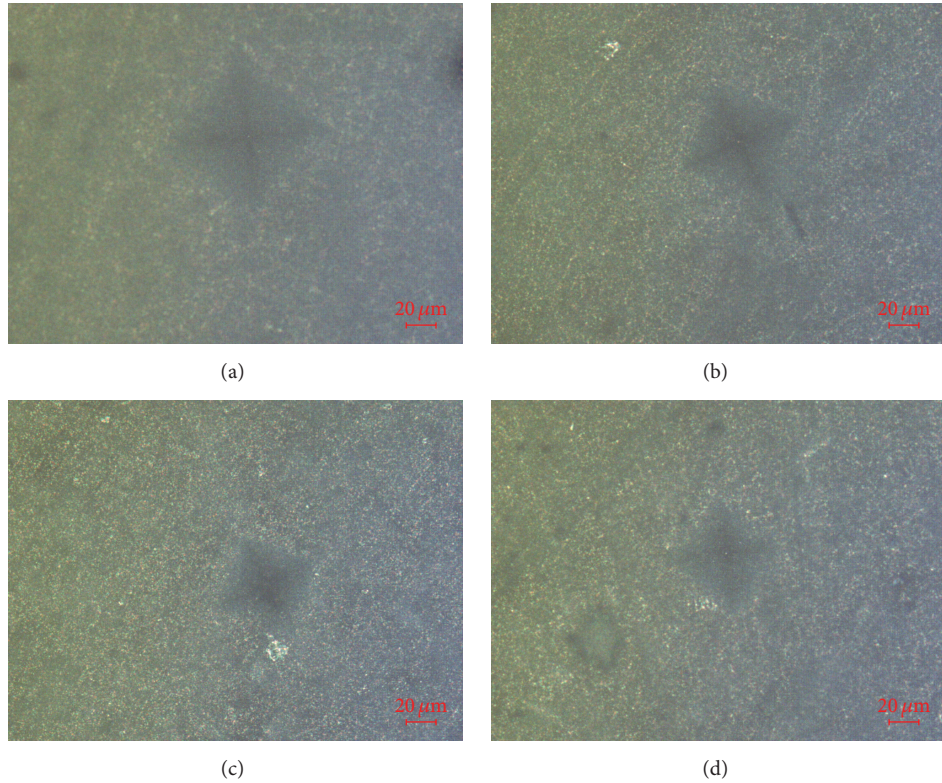


FIGURE 5: Optical microscope of the ZrO<sub>2</sub> ceramics with addition of (a) 0, (b) 1, (c) 3, and (d) 5 wt% TiO<sub>2</sub> contents (the scale bar is 20  $\mu\text{m}$ ).

sizes increased and the microwave sintering enhanced with increasing TiO<sub>2</sub> contents. Thus, it is suggested that in this study the hardness of ZrO<sub>2</sub> was mainly influenced by the enhanced microwave sintering with TiO<sub>2</sub> addition.

Figure 6 shows further the Vickers hardness of the ZrO<sub>2</sub> ceramics with addition of 0, 1, 3, and 5 wt% TiO<sub>2</sub> contents under different sintering temperatures. It is actually found that, with increasing the sintering temperature from 1150°C to 1300°C, the Vickers hardness of the ZrO<sub>2</sub> ceramics increased in spite of TiO<sub>2</sub> contents. The increase was not obvious from 1150°C to 1200°C and then enhanced after 1200°C.

Moreover, for the same sintering temperature, the Vickers hardness of ZrO<sub>2</sub> was enlarged by doping with TiO<sub>2</sub> in spite of the content. Namely, TiO<sub>2</sub> addition into the ZrO<sub>2</sub> ceramics actually improved the Vickers hardness of the ZrO<sub>2</sub> ceramics under the microwave sintering. Figure 7 shows the optical microscope of the ZrO<sub>2</sub> ceramics with addition of 5 wt% TiO<sub>2</sub> contents sintered at (a) 1150°C, (b) 1200°C, (c) 1250°C, and (d) 1300°C. It is verified that, with higher sintering temperature, the length of the cross-indentation decreased due to the increase of the Vickers hardness. From the above results, it is summarized that TiO<sub>2</sub> content plays

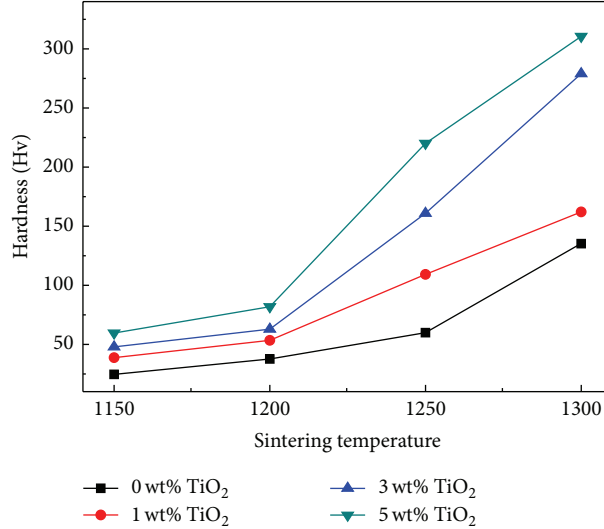


FIGURE 6: Vickers hardness of the  $\text{ZrO}_2$  ceramics with addition of 0, 1, 3, and 5 wt%  $\text{TiO}_2$  contents under different sintering temperatures.

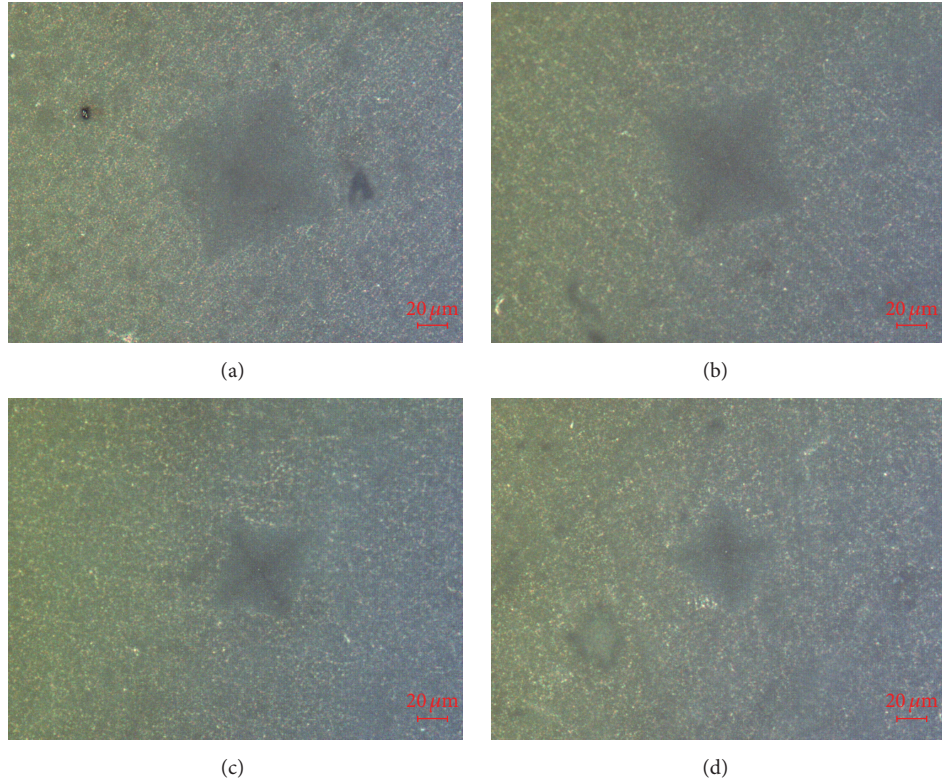


FIGURE 7: Optical microscope of the  $\text{ZrO}_2$  ceramics with addition of 5 wt%  $\text{TiO}_2$  contents sintered at (a) 1150°C, (b) 1200°C, (c) 1250°C, and (d) 1300°C (the scale bar is 20  $\mu\text{m}$ ).

an important role in the crystallite phases, microstructures, and mechanical properties of microwave sintered  $\text{ZrO}_2$  ceramics with  $\text{TiO}_2$  addition. In the future, the sintering temperature shall be high and/or the sintering holding time shall be also longer to achieve the full densification and enough Vickers hardness of the  $\text{ZrO}_2$  ceramics for the dental use.

#### 4. Conclusions

This paper investigated the effect of contents of  $\text{TiO}_2$  addition on microstructure and mechanical properties of microwave sintered zirconia bioceramics for the dental use. The zirconia ceramics with 1, 3, and 5 wt%  $\text{TiO}_2$  addition were sintered using the microwave energy at the sintering temperature of

1300°C. For different TiO<sub>2</sub> content, the main phase was the monoclinic zirconia (m-ZrO<sub>2</sub>) phase and second phase was tetragonal zirconia (t-ZrO<sub>2</sub>) phase. For all sintered samples, the grain growth was nearly completed. The grain sizes increased with increasing TiO<sub>2</sub> contents, indicating that TiO<sub>2</sub> addition effectively improved the grain growth of the ZrO<sub>2</sub> grains. The Vickers hardness increased with TiO<sub>2</sub> contents in the range from 125 to 300 Hv. Moreover, the Vickers hardness of ZrO<sub>2</sub> was enlarged by doping with TiO<sub>2</sub> in spite of the content under the same sintering temperature from 1150°C to 1300°C. Based on the study results, the microwave sintering is verified to be used to sinter ZrO<sub>2</sub> bioceramics with a low sintering temperature, and TiO<sub>2</sub> addition plays an important role in the crystallite phases, microstructures, and mechanical properties of microwave sintered ZrO<sub>2</sub> ceramics.

## Competing Interests

The authors declare that there are no competing interests regarding the publication of this paper.

## Authors' Contributions

Hsien-Nan Kuo and Jyh-Horng Chou contributed to design of experiments and composed the paper. Hsien-Nan Kuo performed experiments and data analysis.

## Acknowledgments

The authors would like to thank the Advanced Electronic Materials Laboratory and Precision Instrument Center of National Pingtung University of Science and Technology for supporting the experimental equipment. This work was supported by the Ministry of Science and Technology, Taiwan, under Grant no. NSC 102-2221-E-151-021-MY3.

## References

- [1] S. Pilathadka, D. Vahalová, and T. Vosáhlo, "The Zirconia: a new dental ceramic material. An overview," *Prague medical report*, vol. 108, no. 1, pp. 5–12, 2007.
- [2] I. Denry and J. R. Kelly, "State of the art of zirconia for dental applications," *Dental Materials*, vol. 24, no. 3, pp. 299–307, 2008.
- [3] R. H. J. Hannink, P. M. Kelly, and B. C. Muddle, "Transformation toughening in zirconia-containing ceramics," *Journal of the American Ceramic Society*, vol. 83, no. 3, pp. 461–487, 2000.
- [4] S. R. Choi and N. P. Bansal, "Mechanical behavior of zirconia/alumina composites," *Ceramics International*, vol. 31, no. 1, pp. 39–46, 2005.
- [5] K. G. Kanade, J. O. Baeg, S. K. Apte, T. L. Prakash, and B. B. Kale, "Synthesis and characterization of nanocrystallized zirconia by hydrothermal method," *Materials Research Bulletin*, vol. 43, no. 3, pp. 723–729, 2008.
- [6] M. J. Abden, M. K. Islam, and J. D. Afrose, "Microstructure and mechanical properties of 3YSZ ceramics reinforced with Al<sub>2</sub>O<sub>3</sub> particles," *International Journal of Materials Engineering*, vol. 4, no. 4, pp. 2166–5389, 2014.
- [7] S. Ban, H. Sato, Y. Suehiro, H. Nakanishi, and M. Nawa, "Biaxial flexure strength and low temperature degradation of Ce-TZP/Al<sub>2</sub>O<sub>3</sub> nanocomposite and Y-TZP as dental restoratives," *Journal of Biomedical Materials Research Part B: Applied Biomaterials*, vol. 87, no. 2, pp. 492–498, 2008.
- [8] J. Chevalier, L. Gremillard, A. V. Virkar, and D. R. Clarke, "The tetragonal-monoclinic transformation in zirconia: lessons learned and future trends," *Journal of the American Ceramic Society*, vol. 92, no. 9, pp. 1901–1920, 2009.
- [9] J. LLorca, J. Y. Pastor, P. Poza et al., "Influence of the Y<sub>2</sub>O<sub>3</sub> content and temperature on the mechanical properties of melt-grown Al<sub>2</sub>O<sub>3</sub>-ZrO<sub>2</sub> eutectics," *Journal of the American Ceramic Society*, vol. 87, no. 4, pp. 633–639, 2004.
- [10] D. D. Upadhyaya, A. Ghosh, G. K. Dey, R. Prasad, and A. K. Suri, "Microwave sintering of zirconia ceramics," *Journal of Materials Science*, vol. 36, no. 19, pp. 4707–4710, 2001.
- [11] H.-Y. Chen, M.-H. Weng, S.-J. Chang, and R.-Y. Yang, "Preparation of sr<sub>x</sub>SiO<sub>4</sub>:Eu<sup>3+</sup> phosphors by microwave-assisted sintering and their luminescent properties," *Ceramics International*, vol. 38, no. 1, pp. 125–130, 2012.
- [12] R.-Y. Yang, M. H. Weng, H.-Y. Chen, C.-M. Hsiung, and S.-H. Chen, "The influence of Eu<sup>3+</sup> doping on photoluminescent properties of red emitting phosphor YInGe<sub>2</sub>O<sub>7</sub>:Eu<sup>3+</sup> by microwave assisted and conventional sintering method," *Journal of Luminescence*, vol. 132, no. 2, pp. 478–483, 2012.
- [13] C. Laberty-Robert, F. Ansart, C. Deloget, M. Gaudon, and A. Rousset, "Dense yttria stabilized zirconia: sintering and microstructure," *Ceramics International*, vol. 29, no. 2, pp. 151–158, 2003.
- [14] A. A. Almazdi, H. K. Khajah, H. E. Monaco, and A. Kim, "Applying microwave technology to sintering dental zirconia," *Journal of Prosthetic Dentistry*, no. 12, pp. 60181–60184, 2012.
- [15] Y. Takigawa, Y. Naka, and K. Higashi, "Effect of titania doping on phase stability of zirconia bioceramics in hot water," *Materials Transactions*, vol. 48, no. 3, pp. 332–336, 2007.
- [16] A. Marinis, S. A. Aquilino, P. S. Lund et al., "Fracture toughness of yttria-stabilized zirconia sintered in conventional and microwave ovens," *Journal of Prosthetic Dentistry*, vol. 109, no. 3, pp. 165–171, 2013.

## Research Article

# Singular Value Decomposition Based Features for Automatic Tumor Detection in Wireless Capsule Endoscopy Images

Vahid Faghah Dinevari, Ghader Karimian Khosroshahi, and Mina Zolky Lighvan

*Electrical and Computer Engineering Department, University of Tabriz, Tabriz 51666 16471, Iran*

Correspondence should be addressed to Vahid Faghah Dinevari; v.faghah@tabrizu.ac.ir

Received 11 January 2016; Accepted 11 April 2016

Academic Editor: Alberto Borboni

Copyright © 2016 Vahid Faghah Dinevari et al. This is an open access article distributed under the Creative Commons Attribution License, which permits unrestricted use, distribution, and reproduction in any medium, provided the original work is properly cited.

Wireless capsule endoscopy (WCE) is a new noninvasive instrument which allows direct observation of the gastrointestinal tract to diagnose its relative diseases. Because of the large number of images obtained from the capsule endoscopy per patient, doctors need too much time to investigate all of them. So, it would be worthwhile to design a system for detecting diseases automatically. In this paper, a new method is presented for automatic detection of tumors in the WCE images. This method will utilize the advantages of the discrete wavelet transform (DWT) and singular value decomposition (SVD) algorithms to extract features from different color channels of the WCE images. Therefore, the extracted features are invariant to rotation and can describe multiresolution characteristics of the WCE images. In order to classify the WCE images, the support vector machine (SVM) method is applied to a data set which includes 400 normal and 400 tumor WCE images. The experimental results show proper performance of the proposed algorithm for detection and isolation of the tumor images which, in the best way, shows 94%, 93%, and 93.5% of sensitivity, specificity, and accuracy in the RGB color space, respectively.

## 1. Introduction

Gastrointestinal (GI) tract diseases are so common all over the world. Therefore, the possibility of direct observation of the GI tract is beneficial for treatment of these patients. None of the traditional methods like endoscopy and colonoscopy can reach the small intestine which is the main body of the GI tract. This limitation occurs due to the complex structure of the small intestine. Wireless capsule endoscopy is a new instrument which helps doctors achieve this purpose and alleviates the pain caused by the traditional endoscopy for the patients. As a result, it is widely used in hospitals. WCE video data identification is done by physicians, which takes a long time due to the large number of images. The average number of WCE images in each experiment is about 50,000 which takes around two hours to be reviewed and analyzed [1, 2]. Furthermore, some abnormalities appear just in one or two frames of the video which might be missed by physicians. On the other hand, variation of abnormalities in size, color, and distribution makes their detection too difficult by naked eyes. All these problems motivate researchers to

develop other reliable systems to reduce the great burden of physicians. However, it should be considered that this goal is very challenging because the appearance of varied diseases is so different and the same diseases have lots of variations in color, shape, and size [3, 4].

Tumor is one of the GI tract diseases which greatly threaten human health [5]. In case of early detection, this abnormality can be prevented and cured easily; therefore, many studies have been done to propose a computer aided detection (CAD) system to identify tumors in the WCE images. Karkanis et al. utilized color wavelet covariance features and a linear discriminant analysis classifier to detect tumors in the colonoscopy videos. This feature is based on the covariance of the second-order textural measures of the different color bands [6]. Moreover, Li used the wavelet transform and uniform local binary pattern (ULBP) as the texture features for detection of tumors in the WCE images [7, 8]. Martins et al. utilized the advantage of high directional sensitivity of the discrete curvelet transform and the Gaussian mixture model as a classifier to detect tumors in the WCE images [9].

In this work, a new algorithm is proposed which exploits color based texture features and SVM to detect tumor in the WCE images. The proposed method integrates advantages of DWT and SVD to characterize the normal and tumor WCE images. DWT is used for multiresolution image analysis as a preprocessing step. In the following step, the SVD based features which are invariant against rotation are extracted. Finally, SVM which has a better ability to classify high dimensional feature vectors is used to classify the WCE images. The experimental results from the presented data set show that this new scheme achieves an encouraging performance in tumor detection.

This paper is organized as follows. The new wavelet based SVD color texture feature extraction for the WCE images is presented in Section 2. In Section 3, SVM, which was used to classify our data set, is briefly introduced. Section 4 presents the experimental results in detail, including the detection evaluation. Finally, the conclusion will be given in Section 5.

## 2. Texture Features

Due to development in the image analysis methods, the normal and abnormal regions in the WCE images can be distinguished properly. In the present work, we attempt to design a CAD system to recognize tumor in the WCE images. Tumor and normal WCE images have different color and texture features as shown in Figures 1 and 2. These different appearances motivate us to select color texture feature as an image analyzer. This texture is reddish compared to the normal ones [10] due to the increment of blood capillary density in the tumor. Also, the inflation and inflammation surface of tumors can isolate them from the normal textures [11]. The most important problems in this identification are the time varying illumination environment and the great variety in tumor appearances which can be observed in Figure 1 [3]. Therefore, the CAD system should be powerful enough to overcome these problems.

To have a local analysis, the input WCE images are divided into nine patches according to Figure 3. Since the size of the input image is  $256 \times 256$  pixels, the number of  $128 \times 128$  overlapping patches is set to three in both directions. For better image analysis, DWT is applied to each patch to have multiresolution and zooming ability. In addition, the SVD based features which are invariant to rotation are extracted from the created subpatch. Finally, SVM is used to classify the WCE images because of its better ability to classify high dimensional feature vectors. The methodology of the proposed CAD system is shown in Figure 4.

**2.1. Discrete Wavelet Transform.** Wavelet transform is a powerful tool for multiresolution image analysis [12]. Also, zooming ability and local characterization of the wavelet transform provide a much efficient analysis of the WCE images which contain different scale information. DWT can decompose an image into different subbands with both time information and frequency information that are implemented with a separable filter-bank [13]. To create decomposed subimages that are shown in Figure 5, an image is convoluted with a low pass filter (L) and a high pass filter (H). The LL subimage,



FIGURE 1: Several WCE images with tumor.

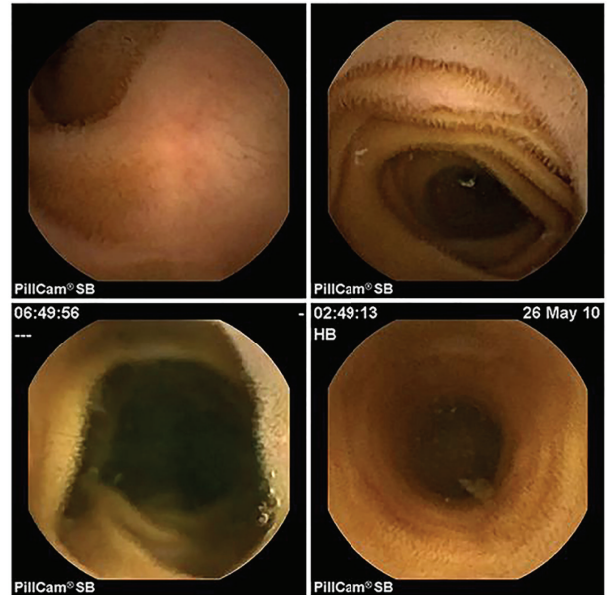


FIGURE 2: Several normal WCE images.

which is called approximation component, is obtained from low pass filtering in both directions. This subimage is very similar to the original image and is used to generate second-level decomposition. The other three subimages are called detailed components. HL is derived from low pass filtering along the vertical direction and high pass filtering along the horizontal direction. The remaining LH and HH subimages can be explained similarly [8, 14]. In this study, we only apply the two-level DWT to each color channel of the WCE images.

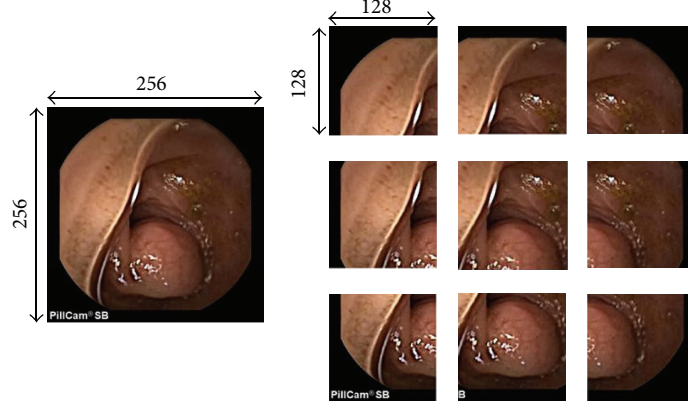


FIGURE 3: Patches chosen from one WCE image.

**2.2. Singular Value Decomposition.** Singular value decomposition is a tool for exploratory data analysis which dissociates the  $m \times n$  data matrix  $X$  as follows [15]:

$$X = USV^T, \quad (1)$$

where  $U$  is an  $m \times m$  orthonormal matrix whose columns are called the left singular vectors or the gene coefficient vectors of  $X$ . Also,  $V$  is an  $n \times n$  orthonormal matrix whose columns are called the right singular vectors or the expression level vectors of  $X$ . Matrix  $S$  is an  $m \times n$  diagonal matrix which is represented as

$$S = \begin{bmatrix} s_1 & \cdots & 0 \\ \vdots & \ddots & \vdots \\ 0 & \cdots & s_{256} \end{bmatrix}. \quad (2)$$

The diagonal elements of matrix  $S$  are called the singular values of  $X$  which are used to create the feature vectors [16]. If the input image size is  $256 \times 256$ , the singular value size will be  $1 \times 256$ .

In the created subimages, instead of the normal part, there are more texture details in tumors; therefore, the corresponding singular values are bigger than the other parts. This texture difference is used to identify tumors in the WCE images. As mentioned before, textural features are better analyzed in detailed subimages [17], so we use  $HL_i$ ,  $LH_i$ , and  $HH_i$  ( $i = 1, 2$ ) as the bases for the textural feature analysis. Since the WCE images are color ones, each color channel is processed independently. To decrease the feature vector dimension, we compare the accuracy of three color channels in each level of DWT and select the biggest one to extract the SVD based features. Accordingly, the feature vector dimension for each WCE image using the proposed method is  $9 \times [(64 \times 3) + (32 \times 3)] = 2592$ , as illustrated in Figure 6.

In this work, RGB (red, green, and blue) and HSV (hue, saturation, and value) color spaces are used to find the best color space for our feature extraction method. The RGB model is the most convenient color space in image and video processing applications because of the high correlation

among the RGB channels [18]. On the other hand, the HSV color model separates color information into chromaticity and intensity, and it is invariant to illumination direction and illumination intensity [19]. Also, the HSV color space is very close to the perceived colors by the human being [6]. These properties have made the HSV model less sensitive to illumination variation which is a common problem of the WCE images as the battery weakens over time.

### 3. Support Vector Machine

Support vector machine as an optimal marginal classifier is developed by Vapnik [20]. SVM has been successfully employed in lots of applications providing satisfying results compared to the other methods [7]. The SVM algorithm processes data by minimum classification structural error and good ability to tackle high dimensional problems. As previously mentioned, the SVM classifier, with strong generalization capability, is able to overcome the problem of having great variations in tumor appearances in the WCE images [21].

SVM uses a training set to build a binary classifier which separates the positive and negative samples. The training set is composed of input vectors of  $x_i \in R^N$  and the corresponding target values of  $y_i \in \{-1, 1\}$  for  $(i = 1 \dots m)$ . The aim is to find a function which correctly classifies the test data as a positive or negative sample.

The SVM algorithm finds a hyperplane with maximized separation margin which is defined by the following equation:

$$w^T f(x) + b = 0, \quad (3)$$

where  $f(x)$  is a nonlinear mapping from the input space to the bigger dimension feature space which has less overlap between the two classes and  $b$  is a scalar which can be estimated from the Karush-Kuhn-Tucker complementary condition. The maximized margin hyperplane is calculated by the following equation [20]:

$$w = \sum_{i=1}^m (l_i y_i f(x_i)), \quad (4)$$

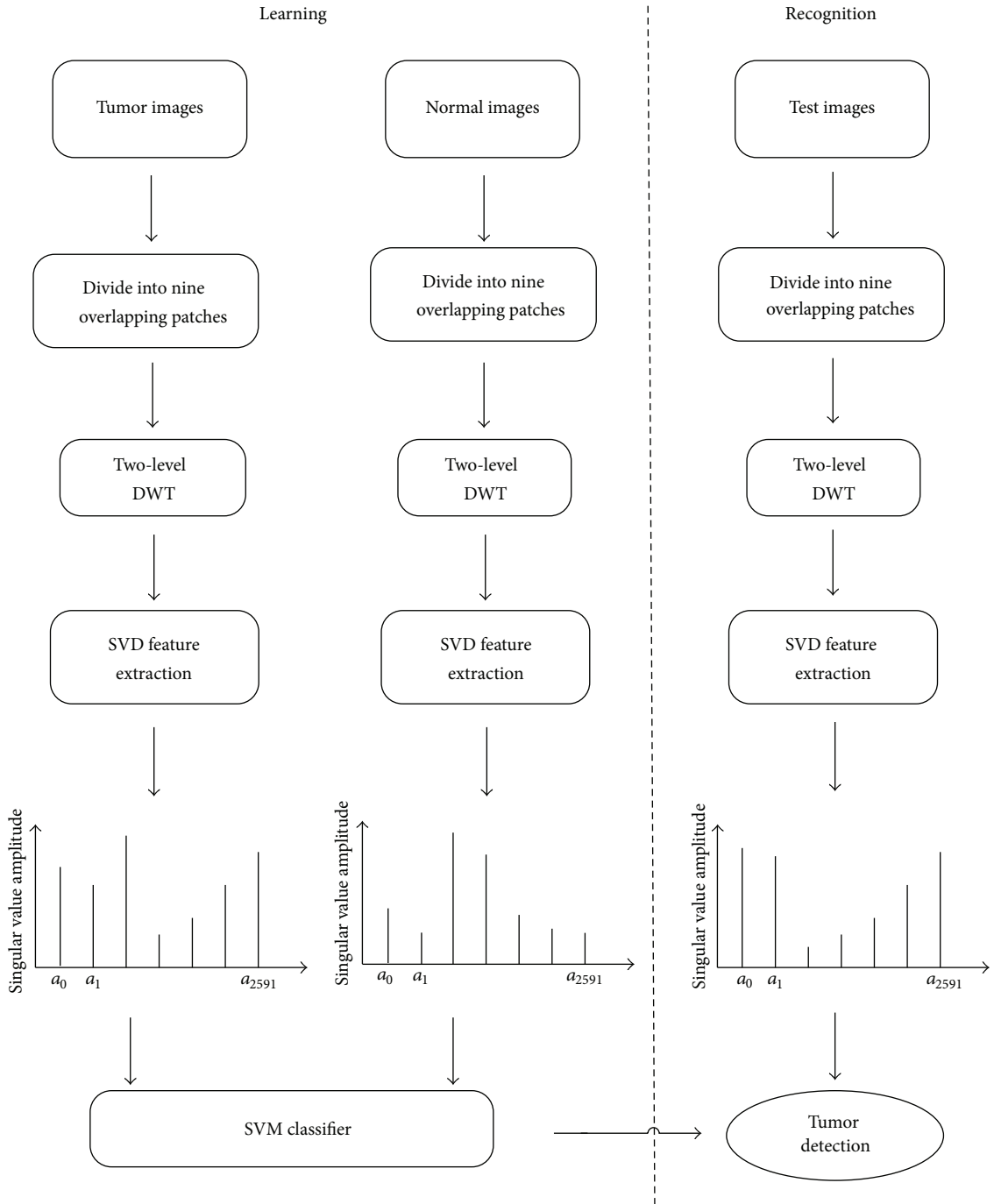


FIGURE 4: The methodology of the proposed CAD system.

where  $l_i$  is the Lagrange multiplier that can be calculated by maximization of

$$L_D = \sum_{i=1}^m l_i - \frac{1}{2} \sum_{i=1}^m \left( \sum_{j=1}^m l_i l_j y_i y_j K(x_i, x_j) \right), \quad (5)$$

$$K(x_i, x_j) = f^T(x_i) f(x_j),$$

where  $K$  is a kernel function which is implemented by the linear, polynomial, sigmoid, and radial basis functions (RBF) [22]. The test input vector  $x$  is applied to the SVM function and it returns +1 for positive samples and -1 for negative ones with regard to the equation below:

$$y = \text{sign} \left\{ \sum_{i=1}^m l_i K(x_i, x) + b \right\}. \quad (6)$$

## 4. Results

For performance evaluation of the proposed algorithm, we use an experimental data set which contains 400 tumor images from 6 pathological cases with different tumor appearances and 400 normal images from 6 normal pathological cases. These images are obtained from PillCam Company (<http://www.givenimaging.com/>). The resolution of these images is  $256 \times 256$  pixels. In addition, to obtain reliable results, some WCE images with a few bubbles and feces, similar to the ones in Figure 7, have been added to our data set.

To extract the performance of the proposed method, each image is manually labeled as a positive sample (tumor image) or a negative one (normal image) to create the ground truth. In this case, 300 normal samples and 300 tumor samples are used as the training set, while the remaining 100 normal samples and 100 tumor ones are used as the test set. This procedure is repeated four times in order to prevent overfitting of the classification results by exchanging the training and testing images. At last, the average recognition rates are used to demonstrate the performance of the proposed method. Success of the WCE image identification is measured due to its sensitivity, specificity, and accuracy which can be explained as follows [6–8]:

Sensitivity

$$= \frac{\text{Number of Correct Positive Predictions}}{\text{Number of Positives}},$$

Specificity

$$= \frac{\text{Number of Correct Negative Predictions}}{\text{Number of Negatives}},$$

$$\text{Accuracy} = \frac{\text{Number of Correct Predictions}}{\text{Number of Positives and negatives}}.$$

Haar wavelet is utilized in this work for implementing DWT because of its superior discriminating power which is illustrated in [23]. Also, to achieve the optimal classification performance, RBF kernel function is used for implementation of SVM.

The performance of the proposed two-level wavelet based SVD features for automatic tumor detection in the RGB color channels is shown in Tables 1, 2, and 3, independently. According to the results, the utmost accuracy is obtained in the first and second levels of DWT from the R and G color channels, respectively, which are used to extract features in the proposed method. The efficiency of the red channel is due to the fact that tumor has more blood vessels compared to the normal textures. Also, the best recognition rate of the proposed method in the first and second levels of DWT in the HSV color channels is obtained from the value channel. These are shown in Tables 4, 5, and 6. Finally, to calculate the performance of the proposed method, the selective color channel is utilized for the first and second levels of DWT to extract the corresponding singular values to create the feature vector. The performance of the proposed algorithm in the RGB and HSV color spaces is shown in Table 7.

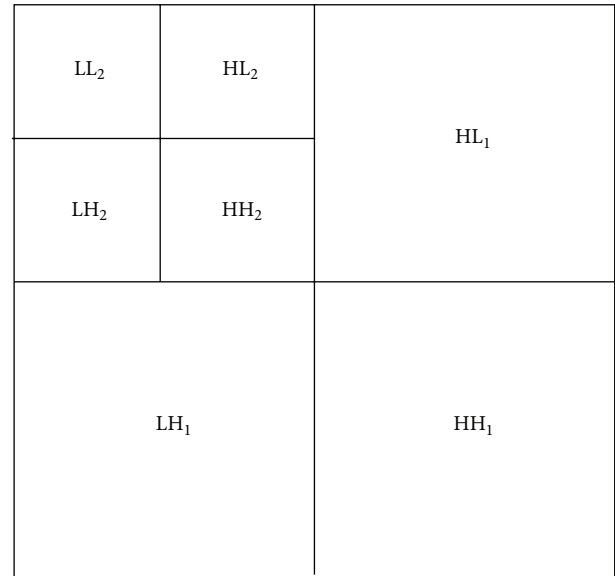


FIGURE 5: Two-level image decomposed using DWT for one color channel.

TABLE 1: Results obtained using the proposed feature in R channel.

	Sensitivity	Specificity	Accuracy
Level 1	93.5%	90.5%	92%
Level 2	90%	83%	86.5%
Level 1 + 2	93.75%	91.25%	92.5%

TABLE 2: Results obtained using the proposed feature in G channel.

	Sensitivity	Specificity	Accuracy
Level 1	90.5%	93%	91.75%
Level 2	86%	88%	87%
Level 1 + 2	91%	93.5%	92.25%

TABLE 3: Results obtained using the proposed feature in B channel.

	Sensitivity	Specificity	Accuracy
Level 1	91%	88.5%	89.75%
Level 2	88%	85%	86.5%
Level 1 + 2	93%	90%	91.5%

To evaluate the performance of the proposed method, it is compared with the wavelet based ULBP which is the latest similar feature proposed by Li and Meng [7] to be used for tumor detection. SVM is used as a classifier for this feature. Tables 8 and 9 show the recognition rates obtained from implanting the wavelet based ULBP in the RGB and HSV color spaces with the current data set.

Finally, the extracted results from the proposed algorithm and two-level wavelet based ULBP in the RGB and HSV color models are compared in Figure 8. The results indicate that the presented SVD based algorithm has a better performance in automatic tumor detection in the WCE images in terms

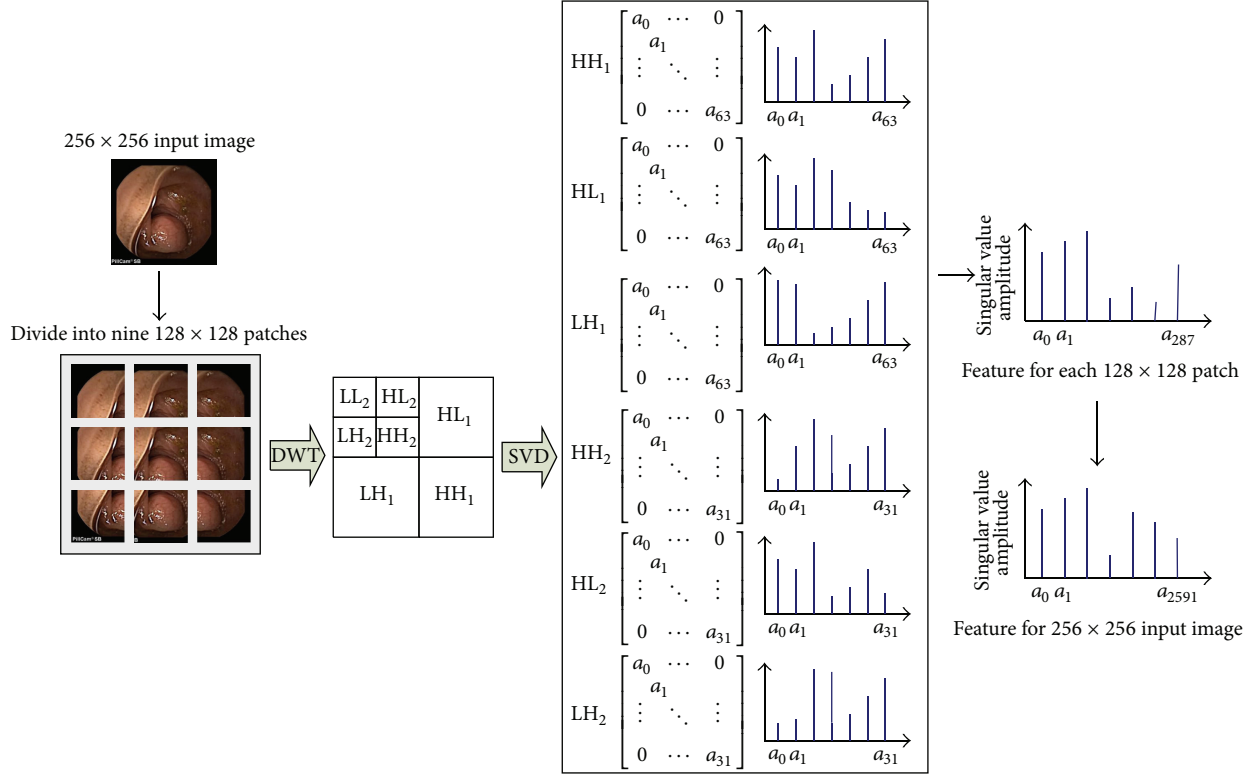


FIGURE 6: The process for extracting SVD based color texture feature using two-level DWT.

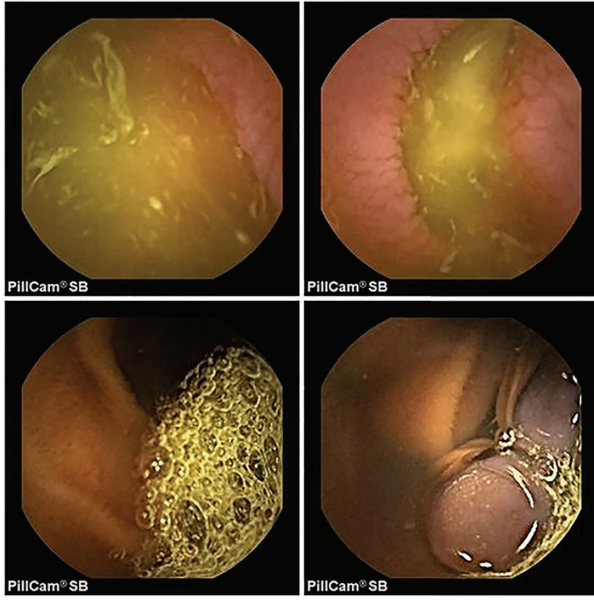


FIGURE 7: Several normal WCE images.

of sensitivity, specificity, and accuracy compared to the two-level wavelet based ULBP algorithm in both color spaces. The highest accuracy obtained from the proposed algorithm is 93.5% in the RGB color model while the best recognition rate extracted from employing the two-level DWT + ULBP

TABLE 4: Results obtained using the proposed feature in H channel.

	Sensitivity	Specificity	Accuracy
Level 1	86.5%	80%	87.75%
Level 2	82.5%	81.5%	81.5%
Level 1 + 2	87.5%	86.5%	89.5%

TABLE 5: Results obtained using the proposed feature in S channel.

	Sensitivity	Specificity	Accuracy
Level 1	94%	79%	86.5%
Level 2	80%	83%	81.5%
Level 1 + 2	93%	84%	88.5%

TABLE 6: Results obtained using the proposed feature in V channel.

	Sensitivity	Specificity	Accuracy
Level 1	91%	90%	90.5%
Level 2	89.5%	85%	87.5%
Level 1 + 2	92.5%	90.5%	91.5%

is 88.5% in the same color model. High accuracy obtained by the proposed CAD system demonstrates that the system can overcome the problem of the great variety of tumor appearances in the time varying illumination environments. Better recognition rate of the proposed method for tumor detection in the WCE images is due to the fact that SVD is a better tool to analyze data from different appearance textures.

TABLE 7: Results obtained using the proposed algorithm in RGB and HSV color spaces.

Color space	Color channel used for the first level of the DWT	Color channel used for the second level of the DWT	Sensitivity	Specificity	Accuracy
RGB	R channel	G channel	94%	93%	93.5%
HSV	V channel	V channel	92.5%	90.5%	91.5%

TABLE 8: Results obtained using DWT + ULBP [7] in RGB color space.

	Sensitivity	Specificity	Accuracy
Level 1	86%	85%	85.5%
Level 2	81%	83.5%	82.75%
Level 1 + 2	87%	90%	88.5%

TABLE 9: Results obtained using DWT + ULBP [7] in HSV color space.

	Sensitivity	Specificity	Accuracy
Level 1	84%	86%	85%
Level 2	79%	78%	78.5%
Level 1 + 2	85%	90%	87.5%

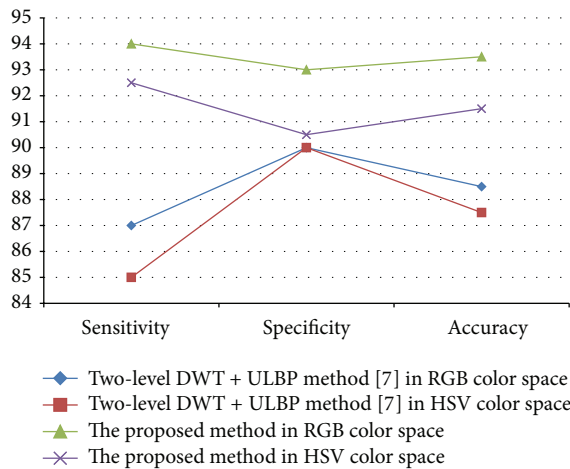


FIGURE 8: Extracted results from the proposed algorithm and two-level DWT + ULBP method in RGB and HSV color spaces.

On the other hand, local analysis of the WCE images can help in improving the performance of the proposed method.

## 5. Conclusions

A new CAD system has been proposed in this paper for automatic tumor detection in the WCE images. This method locally investigated the input WCE images to extract features. The advantage of the proposed system is based on a new feature extraction method with multiresolution and rotation invariant analysis ability which exploits wavelet based singular value decomposition. In addition, support vector machine with high dimensional classification ability is used

to distinguish between the normal and tumor samples in the WCE images. The experimental results from the presented data set which contains 800 WCE images show that this scheme is more powerful in tumor detection. The best recognition rates of 94%, 93%, and 93.5% are achieved in terms of sensitivity, specificity, and accuracy using the two-level selective wavelet based SVD feature extractor in the RGB color space.

## Competing Interests

The authors declare that they have no competing interests.

## References

- [1] D. G. Adler and C. J. Gostout, "Wireless capsule endoscopy," *Hospital Physician*, vol. 39, pp. 14–22, 2003.
- [2] R. Sidhu, D. S. Sanders, K. Kapur, L. Marshall, D. P. Hurlstone, and M. E. McAlindon, "Capsule endoscopy: is there a role for nurses as physician extenders?" *Gastroenterology Nursing*, vol. 30, no. 1, pp. 45–50, 2007.
- [3] J. T. Carlo, D. DeMarco, B. A. Smith et al., "The utility of capsule endoscopy and its role for diagnosing pathology in the gastrointestinal tract," *American Journal of Surgery*, vol. 190, no. 6, pp. 886–890, 2005.
- [4] M. T. Coimbra and J. P. S. Cunha, "MPEG-7 visual descriptors-contributions for automated feature extraction in capsule endoscopy," *IEEE Transactions on Circuits and Systems for Video Technology*, vol. 16, no. 5, pp. 628–636, 2006.
- [5] S. L. Parker, T. Tong, S. Bolden, and P. A. Wingo, "Cancer statistics, 1997" *CA: A Cancer Journal for Clinicians*, vol. 47, no. 1, pp. 5–27, 1997.
- [6] S. A. Karkanis, D. K. Iakovidis, D. E. Maroulis, D. A. Karras, and M. Tzivras, "Computer-aided tumor detection in endoscopic video using color wavelet features," *IEEE Transactions on Information Technology in Biomedicine*, vol. 7, no. 3, pp. 141–152, 2003.
- [7] B. Li and M. Q.-H. Meng, "Tumor recognition in wireless capsule endoscopy images using textural features and SVM-based feature selection," *IEEE Transactions on Information Technology in Biomedicine*, vol. 16, no. 3, pp. 323–329, 2012.
- [8] B. Li, M. Q.-H. Meng, and J. Y. W. Lau, "Computer-aided small bowel tumor detection for capsule endoscopy," *Artificial Intelligence in Medicine*, vol. 52, no. 1, pp. 11–16, 2011.
- [9] M. M. Martins, D. J. Barbosa, J. Ramos, and C. S. Lima, "Small bowel tumors detection in capsule endoscopy by Gaussian modeling of color curvelet covariance coefficients," in *Proceedings of the 32nd Annual International Conference of the IEEE Engineering in Medicine and Biology Society (EMBC '10)*, pp. 5557–5560, September 2010.
- [10] I. Flamme, T. Fröhlich, and W. Risau, "Molecular mechanisms of vasculogenesis and embryonic angiogenesis," *Journal of Cellular Physiology*, vol. 173, no. 2, pp. 206–210, 1997.

- [11] R. A. Mathias, S. K. Gopal, and R. J. Simpson, "Contribution of cells undergoing epithelial-mesenchymal transition to the tumour microenvironment," *Journal of Proteomics*, vol. 78, pp. 545–557, 2013.
- [12] T. C. Wang and N. B. Karayiannis, "Detection of microcalcifications in digital mammograms using wavelets," *IEEE Transactions on Medical Imaging*, vol. 17, no. 4, pp. 498–509, 1998.
- [13] S. G. Mallat, "Theory for multiresolution signal decomposition: the wavelet representation," *IEEE Transactions on Pattern Analysis and Machine Intelligence*, vol. 11, no. 7, pp. 674–693, 1989.
- [14] W.-L. Lee, Y.-C. Chen, and K.-S. Hsieh, "Ultrasonic liver tissues classification by fractal feature vector based on M-band wavelet transform," *IEEE Transactions on Medical Imaging*, vol. 22, no. 3, pp. 382–392, 2003.
- [15] G. H. Golub and C. F. Van Loan, *Matrix Computations*, JHU Press, 2012.
- [16] B. Nagarajan and V. Devendran, "Singular value decomposition based features for vehicle classification under cluttered background and mild occlusion," *Procedia Engineering*, vol. 30, pp. 529–534, 2012.
- [17] K. W. Abyoto, S. J. Wirdjosoedirdjo, and T. Watanabe, "Unsupervised texture segmentation using multi-resolution analysis for feature extraction," *Journal of Tokyo University of Information Sciences*, vol. 2, pp. 49–61, 1998.
- [18] C. H. Li and P. C. Yuen, "Regularized color clustering in medical image database," *IEEE Transactions on Medical Imaging*, vol. 19, no. 11, pp. 1150–1155, 2000.
- [19] T. Gevers, J. Van de Weijer, and H. Stokman, *Color Image Processing: Methods and Applications: Color Feature Detection*, CRC Press, New York, NY, USA, 2006.
- [20] V. N. Vapnik, *The Nature of Statistical Learning Theory*, Springer Science & Business Media, New York, NY, USA, 1995.
- [21] L. Wang, *Support Vector Machines: Theory and Applications*, Springer, Berlin, Germany, 2005.
- [22] C. J. C. Burges, "A tutorial on support vector machines for pattern recognition," *Data Mining and Knowledge Discovery*, vol. 2, no. 2, pp. 121–167, 1998.
- [23] L. Semler, L. Dettori, and J. Furst, "Wavelet-based texture classification of tissues in computed tomography," in *Proceedings 18th IEEE Symposium on Computer-Based Medical Systems*, pp. 265–270, Dublin, Ireland, 2005.